INFORMATION TO USERS

This manuscript has been reproduced from the microfilm master. UMI films the text directly from the original or copy submitted. Thus, some thesis and dissertation copies are in typewriter face, while others may be from any type of computer printer.

The quality of this reproduction is dependent upon the quality of the copy submitted. Broken or indistinct print, colored or poor quality illustrations and photographs, print bleedthrough, substandard margins, and improper alignment can adversely affect reproduction.

In the unlikely event that the author did not send UMI a complete manuscript and there are missing pages, these will be noted. Also, if unauthorized copyright material had to be removed, a note will indicate the deletion.

Oversize materials (e.g., maps, drawings, charts) are reproduced by sectioning the original, beginning at the upper left-hand corner and continuing from left to right in equal sections with small overlaps.

ProQuest Information and Learning
300 North Zeeb Road, Ann Arbor, MI 48106-1346 USA
800-521-0600

DYNAMICS OF LOOSELY SUPPORTED HEAT EXCHANGER TUBES

By

MARWAN HASSAN

A Thesis
submitted to the School of Graduate Studies
in Partial Fulfilment of the Requirements
for the Degree of
Doctor of Philosophy

McMaster University

DYNAMICS OF LOOSELY SUPPORTED HEAT EXCHANGER TUBES

Doctor of Philosophy (2000) McMaster University

(Mechanical Engineering) Hamilton, Ontario

Title: Dynamics of Loosely Supported Heat Exchanger Tubes

Author: Marwan Hassan
Master of Science, Tuskegee University, U.S.A.
Bachelor of Science, Helwan University, Egypt

Supervisors: Dr. M. A. Dokainish
Dr. D. S. Weaver

Number of Pages: xv, 195

ABSTRACT

Tube failure due to excessive flow-induced vibrations is a major concern with regards to the operation of heat exchangers in nuclear power and chemical process plants. Typical consequences include unplanned and expensive plant shutdowns to plug the failed tubes. Fretting wear resulting from tube/support impact is considered as a major contributor to tube failure. Impact forces, which occur when tube vibration amplitudes exceed the local support clearance, play a vital role in determining tube wear. Turbulence is one of the possible excitation mechanisms which can drive tube vibrations and is of particular concern in heat exchangers. Unlike other excitation mechanisms, turbulence has a persistent effect and thus determines the long term reliability of the heat exchangers.

To address these issues, a point contact algorithm describing the tube/support interaction was implemented in an in-house finite element program and validated by several published examples. Pseudo-forces were utilized in conjunction with modal superposition in solving the nonlinear equations of tube motion. The equilibrium equations were solved iteratively to calculate the contact forces required to oppose any tube/support overlaps. The impact model was further modified to consider more realistic tube/support contact configurations. The new model considers a finite support width. The contact forces arising from the tube/support overlap are due to two different contact situations that may be encountered (point and segment contact). A distributed stiffness along the tube/support interface was utilized to model the segment contact. The resulting contact pressure was calculated using the displacement profile along the contact segment. The general point contact model considers any tube/support overlap that may occur between the principal contact node and the neighbouring node.

Time-domain simulations of the nonlinear response of the tube are presented to determine the effect of various tube/support parameters on the system's vibratory characteristics. Special attention was paid to the effect of clearance enlargement due to fretting wear on the response of tubes in lattice-bar supports. The tube response, the impact force, and the contact ratio (ratio of the contact time to the total time) were analysed and presented in a dimensionless form. The dimensionless parameters utilized proved to be effective at collapsing all the data pertaining to different flow velocities over a single curve. This aids in identifying the role of support variables in influencing tube dynamics. Moreover, these parameters may also be used to scale the results in order to account for differences in geometrical and material properties. In addition, simulations were conducted to investigate the effect of the support type, the flow orientation, and the lattice-bar offset on the tube dynamics. The study indicates that some flow orientations, support types, and support offsets provide a favourable support geometry for higher normal work rates. This, in turn, increases susceptibility to fretting wear damage. These results provide new insights and a better understanding of the underlying phenomena of nonlinear tube behaviour in loose lattice-bar supports.

ACKNOWLEDGEMENTS

I would like to express my sincerest appreciation to my supervisors, Dr. M. Dokainish and Dr. D. Weaver, for providing kind guidance, consistent encouragement and patience throughout the course of my graduate studies and this research. This support has made my graduate studies enjoyable and productive.

I would also like to thank the members of my supervisory committee, Dr. M. Yetisir (AECL) and Dr. D. Metzger (McMaster University) for their many useful comments and suggestions.

Thanks are also due to my colleagues Rafael Bravo and Tony Robinson for their valuable discussions over sessions of coffee and music: without them it would have been harder.

Thanks are also due to the FIV group members for their attention and patience during my FIV presentations.

I wish to express my appreciation to my lifetime friend, Hossam Kishawy for the help and the support I received during tough times.

I would like to express my gratitude to my dear wife, Christine, who provided me with support and love in addition to her efforts in proofreading this thesis.

Last, but not least, I would like to express my deep gratitude towards my parents, my sister, and my brothers for their encouragement, support, and love.

TABLE OF CONTENTS

Contents Page

LIST OF FIGURES

LIST OF TABLES

NOMENCLATURE

A	principle contact node
Cr	clearance
$[C_s]$	damping matrix (structural component)
$[C_{NL}]$	damping matrix (contact contribution)
$\bar{d}^i$	displacement vector of the i^{th} node
D	tube diameter
$\hat{e}_1$, $\hat{e}_2$, and $\hat{e}_3$	unit vectors along the coordinates axes x, y, and z respectively
E	neighbouring contact node
E_{NL}	Euclidean error norms
f_n	natural frequency
F_{dmp}	damping force
F_f	friction force
F_{imp}	impact force
F_N	normal force
F_{spr}	spring force
$\{F_e\}$	external excitation vector
$\{F_{NL}\}$	nonlinear force vector
J^2	joint acceptance
K_{spr}	contact stiffness
$[K_s]$	stiffness matrix (structural component)
$[K_{NL}]$	stiffness matrix (contact contribution)
L	tube length
m	mass per unit length
$[M_s]$	mass matrix (structural component)
r	position vector pointing towards a contact node
r_x, r_y, and r_z	components of the position vector
S_{FF}	PSD of the excitation forces
St	Strouhal number
t	time
{u}	displacement vector
$\hat{u}_{sn}$	support normal unit vectors
$\hat{u}_{sa}$	support axial unit vectors
$\hat{u}_{st}$	support tangential unit vectors
$\hat{u}_{smn}$	support modified normal unit vectors
$\hat{u}_{tn}$	tube normal unit vectors
$\hat{u}_{ta}$	tube axial unit vectors
$\hat{u}_{tt}$	tube tangential unit vectors
U	flow velocity
$\bar{v}^i$	velocity vector of the i^{th} node

V_o	cut-off velocity
V_t	tangential sliding velocity
W_N	normal work rate
W_{tur}	input power by turbulence forces
y_{rms}	RMS displacement
β	material damaping coefficient
δ_n	normal overlap displacement
Δr	beam element length
μ_s	static coefficient of friction
μ_d	dynamic coefficient of friction
ρ	mass density
ζ	modal damping
ω	circular frequency

OVERSCORES

.	first derivative with respect to time
..	second derivative with respect to time

SUPERSCRIPTS

i	i^{th} element
j	j^{th} iteration
T	transpose of a matrix or a vector

SUBSCRIPTS

si	support inactive response

OTHERS

$[\,.\,]$	for matrices
$\|\,.\,\|$	Euclidean norm

CHAPTER 1

INTRODUCTION

1. 1 PREAMBLE

Historically, heat exchangers have been among the most troublesome components of both nuclear power and chemical process plants. Most problems arise due to tube failure, which is attributed to corrosion and mechanical problems. Corrosion problems include denting, pitting, corrosion fatigue, and corrosion cracking on the outer surface of the tube. On the other hand, mechanical problems consist mainly of fretting wear of the tubes. While tube failure is often attributed to tube corrosion at the support location, tube fretting wear due to flow-induced vibrations has been recognized as a significant contributor to tube failure.

The general mechanisms causing the destructive nature of flow-induced vibrations include fluidelastic instability, vortex shedding, and turbulence buffeting. The first of these

mechanisms, fluidelastic instability, can cause tube failure within a short period of time. In order to avoid such a destructive mechanism, design restrictions are imposed, which include either reducing the flow velocity or increasing the tube's natural frequencies. Therefore, supports are installed at a number of locations along the tube to provide a stiffer structure with which to restrain vibrations.

Tube/support assemblies are usually loose fitting due to manufacturing considerations which require these clearances to facilitate tube bundle assembly. The number and locations of these supports are normally chosen to promote stability. However, other excitation sources, such as turbulence, are omnipresent and cannot be avoided. Turbulence provides enough energy for the tubes to vibrate significantly inside the support space. When tube response due to flow-induced forces exceeds the clearance of the tube support, the tubes impact on their supports. In addition to impact, friction forces may also develop at the tube/support interface. Conditions are then favourable for tube fretting wear, which leads to thinning of the tube walls and eventual through-wall wear and tube failure.

Typically, tube failure results in unplanned outages, which lead to expensive repairs and loss of production. This type of failure, unfortunately, occurs frequently. In a recent survey focussing on the years 1992 and 1993, sixty reactors experienced cases of tube leakage related to fretting wear (Guérout and Fisher, 1999). In more severe cases, steam generators have needed to be replaced after a mere eight to twelve years of operation; a time far shorter than the expected operating life of forty years.

Although turbulence-induced vibrations do not lead to rapid catastrophic failures, the amplitude of vibration may be large enough to cause tube failure at the support location due

to the accumulation in fretting wear. Currently, there is an increased interest in predicting long-term tube life. The ability to estimate turbulence-induced response is therefore an important step towards evaluating the damage due to fretting wear, and thus extending the life of heat exchangers. However, turbulence-induced wear is considerably more difficult to predict than the abrupt threshold for fluidelastic instability (Connors 1981).

When predicting nonlinear turbulence-induced vibrations, it is important to consider the nature of the support. This is imperative because the geometry of the support affects the tube dynamics due to variations in the contact configurations. Weaver and Schneider (1983) discussed various support geometries currently used by manufacturers. Among these types of supports, lattice-bars are considered to be very effective. However, the contact configuration of this type of support is complicated due to the number of possible tube/support contact points.

1. 2 OBJECTIVES OF THIS THESIS

The main objectives of the research reported in this thesis are:

1- To develop a reliable analytical tool capable of modelling tube/support interaction in lattice-bar supports.

2- To investigate the effect of turbulence excitation on heat exchanger tube dynamics in lattice-bar supports.

3- To derive proper scaling parameters that reduce the nonlinear random tube response to a dimensionless form convenient for physical insights and for design

purposes.

4- To develop a model that accounts for the width of the support when predicting the tube/support interaction response.

While substantial research has been conducted on the nonlinear response of tubes in loose supports, no results have been published on the influence of lattice-bar supports in spite of their current use. Furthermore, no results have been published on the scaling of the nonlinear tube dynamics using dimensionless parameters, nor on the effect of tube/support bar width.

1. 3 LAYOUT OF THIS THESIS

This thesis consists of six chapters, the first of which includes three sections. The first section illustrates the definition and importance of the dynamics of heat exchanger tubes with loose supports. The second section highlights the main objectives of the thesis. The chapter then ends with an overview of this thesis.

Chapter two provides some background on the structure of heat exchangers, excitation mechanisms, and types of supports. In addition, an up-to-date review of the work done on the current subject is presented. This chapter concludes with a discussion of the knowledge gaps in this field, some of which will be addressed in this thesis.

In chapter three, the formulation of a tube/support interaction model is presented. A discussion then follows on the basic algorithm which is implemented in an in-house general purpose finite element program. The implemented model is then validated by comparing it with three documented examples. Finally, the modelling and implementation of turbulence excitation is presented.

Chapter four includes numerical simulations of tubes held in loose lattice-bar supports. These models represent single span and multi-span tubes subjected to turbulence excitation with various rates of fluid flow. An analysis of the tube/support interaction parameters, such as contact ratio, RMS impact force and work rate, is then performed. A set of dimensionless parameters are introduced to present the tube/support interaction parameters, as well as the tube response. Both square flat-bar supports and rhomboid flat-bar supports are considered in this investigation to explore the effect of support geometry on tube dynamics. In addition, the effect of flow angle on the system dynamics is also considered. Chapter four concludes with an investigation of the effect of the lattice- bar offset.

In chapter five, the tube/support modelling is further extended to account for a very practical issue – the simulation of the support width. A basic mathematical model is derived for flat bars. Calculations of the impact and the friction forces are carried out by considering two modes of contact. These modes are a general point contact mode and a segment contact mode. Simulations are then conducted to study the effect of width on the tube dynamics.

Finally, in chapter six, the main conclusions of the thesis are summarized. Further recommendations for future research work are also proposed.

CHAPTER 2

LITERATURE REVIEW

2. 1 INTRODUCTION

Heat exchangers are widely used in nuclear power and chemical process plants. The main function of a heat exchanger is to transfer the thermal energy from a primary fluid to a secondary fluid. In nuclear power plants, the primary fluid is heated in the reactor core. It then passes through the steam generator (a massive heat exchanger) where the secondary fluid (water) is converted into steam as shown in Figure 2.1. The steam, being at a high pressure and temperature, is directed to turbines which drive electrical power generators. After being used in the turbines, the steam is condensed and fed back to the steam generator as feedwater. Although the primary fluid is usually radioactive, the steam coming out of the

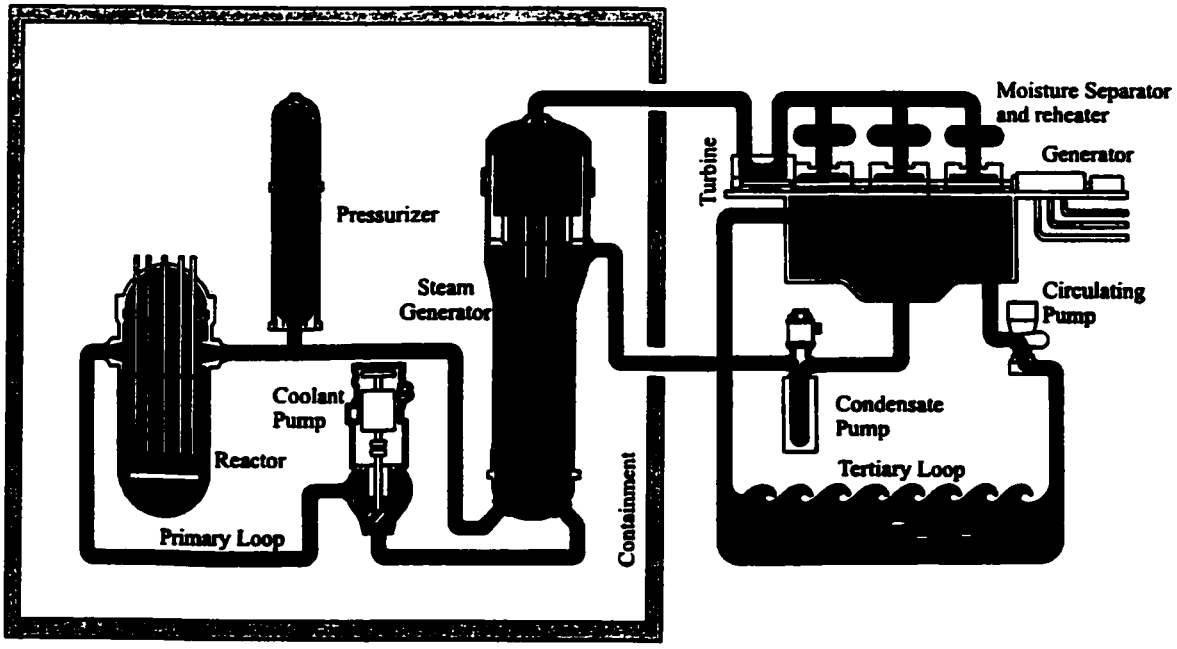

Figure 2.1 Schematic of a pressurized water reactor (Westinghouse Electric Corporation).

containment must not contain any radioactive material. Therefore, it is imperative that the primary and the secondary fluids be completely separated which is accomplished through the use of tubes. The primary fluid passes through the tubes while the secondary fluid flows over them. Hence the integrity of these tubes is of primary concern in the design, construction, operation and maintenance of steam generators.

There are three main types of steam generators: vertical U tube, horizontal, and once-through. Vertical U tube steam generators use inverted U-shaped tubes, while once-through and horizontal designs utilize straight tubes. Figure 2.2 shows a vertical U-tube steam generator. A tube sheet in the lower part of the steam generator separates the primary fluid from the secondary fluid. More than 3000 tubes are mounted on the tubesheet, each having an outer diameter of 5/8 to 3/4 of an inch. Supports are placed along the span of tubes to stabilize them and minimize their movements. In a vertical steam generator, the feed water ring supply header is usually on the outer edge of the steam generator. The water is directed downward, flowing through the downcomer (outer annulus of the steam generator) and through ports across the tubes at the tubesheet. It is then directed upward to flow along the steam generator tubes where its temperature increases until it boils and transforms to steam. The steam/water mixture then passes through a moisture separator mounted in the upper part of the steam generator, leaving the system through a nozzle at the top of the steam generator. The separated water falls back into the annular downcomer of the steam generator.

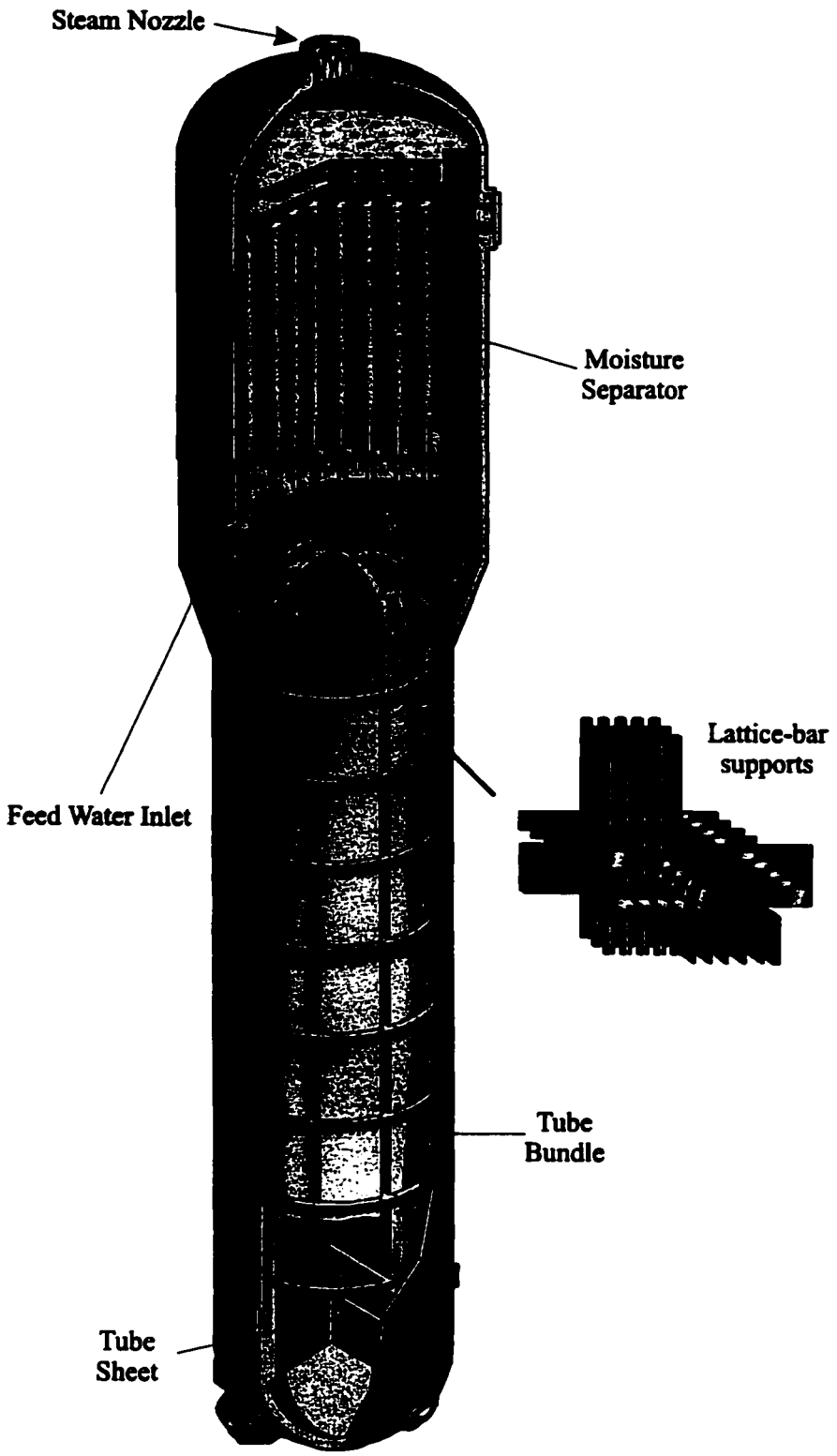

Figure 2.2 General layout of a U-bend steam generator. (Babcock and Wilcox)

2. 2 EXCITATION MECHANISMS

There are three main mechanisms which account for flow-induced vibrations in heat exchangers. These mechanisms depend on the flow conditions and the structure of the tubes. They are broadly classified as a) turbulent buffeting, b) Strouhal periodicity, and c) fluidelastic instability (Weaver and Fitzpatrick 1988).

Strouhal periodicity occurs when a natural frequency of a tube coincides with the frequency of the vorticity shed from the tube. This may result in large amplitude vibrations, especially if the fluid is liquid. Such excitation may appear in the response curve as a discrete amplitude peak which stands out among the turbulence response. Strouhal periodicity is characterized by the Strouhal number:

$$S_t = \frac{fD}{U} \tag{2.1}$$

where f, D, and U are the frequency of the vorticity, the tube diameter, and the mean flow velocity respectively. The Strouhal number for a given fluid/tube configuration is determined experimentally. This information is required at the design stage to avoid resonance between the tube's natural frequency and the frequency of the vortex shedding. Research to date suggests that significant tube vibrations due to Strouhal periodicity may occur in the first few rows of a tube bundle subjected to liquid flow (Weaver and Fitzpatrick 1988) or be encountered with a certain resonance in gas flows. On the other hand, there appears to be no such problem in two-phase flows.

Fluidelastic instability is the excitation mechanism with the greatest potential for short term damage to heat exchangers. The complete process leading to this instability is not

yet fully understood. Generally, in a tube bundle, the fluid forces acting on a tube are affected by both the motion of the tube and its neighbours. This creates an interaction between the fluid forces and the tube motion. Fluidelastic instability forces come into effect when the fluid forces are proportional to the tube displacement and/or are in phase with the tube velocities. Instability occurs when the amount of energy expended by the tube motion through damping is less than the energy input to the tube. The mechanism is characterized by a critical flow velocity below which vibrational amplitudes are small, and above which the amplitudes increase rapidly.

Excessive vibration due to both Strouhal periodicity and fluidelastic instability can be prevented through proper design. However, turbulence excitation is omnipresent and cannot be avoided. In fact, turbulence is promoted in the design to provide improved heat transfer by choosing certain coolant paths and flow rates. Moreover, turbulence in the flow can affect the existence and the strength of other excitation mechanisms such as the Strouhal periodicity. Turbulence-induced random vibration of a tube bundle, sometimes referred to as subcritical vibration, is usually of a much smaller amplitude than that experienced in fluidelastic instability. However, through fretting wear, turbulence-induced random vibrations can determine the long-term reliability of the steam generator tube bundle.

Pettigrew and Gorman (1978) and Blevins *et al.* (1981) developed similar turbulence response design equations. Both considered the general tube boundary conditions and the spatial correlation of the excitation forces. To use these equations, force coefficients are needed to calculate the tube response. These force coefficients can be obtained from the turbulence bounding spectra which have emerged as a standard tool in predicting the

turbulence forces exerted on heat exchanger tubes. Recent investigations have resulted in a number of bounding spectra (Taylor *et al.*, 1988; Axisa *et al.*, 1990; Blevins, 1993; and Oengören and Ziada, 1995). The aforementioned turbulence response design spectra are powerful tools in predicting tube response provided that the fluid-structure is weakly coupled, and the structure responds linearly to the imposed forces.

2. 3 TYPES OF SUPPORTS

Steam generator tubes, being long and slender cylindrical structures, must be supported along their length to maintain their separation, and to minimize destructive flow-induced vibrations due to fluid excitation. Several types of supports have been utilized to support the U-bend and the straight regions of the tubes (Figure 2.3). Early steam generator designs used tube support plates with drilled holes (Figure 2.3a) and plates with broached holes (Figure 2.3c). Drilled hole supports are structurally strong and provide excellent tube support. However, because of their geometry, the annular support area around each tube is not well vented for the release of steam and impurities. As well, drilled hole supports may severely block the flow, especially as corrosion deposits develop.

Wiggle bars (Figure 2.3b) create a structure which is more open to the flow. The radial flexibility of the tube bundle is enhanced by this arrangement.

Flat-bar supports (Figure 2.3d) have proven to be effective in the U-bend region of the tubes. In some designs, the bars drop in and out of the U-bend assembly in a boomerang shape in which both ends of the bars are outside the bundle. Flat bars also provide great flexibility to accommodate differential tube motions in operation due to thermal expansion.

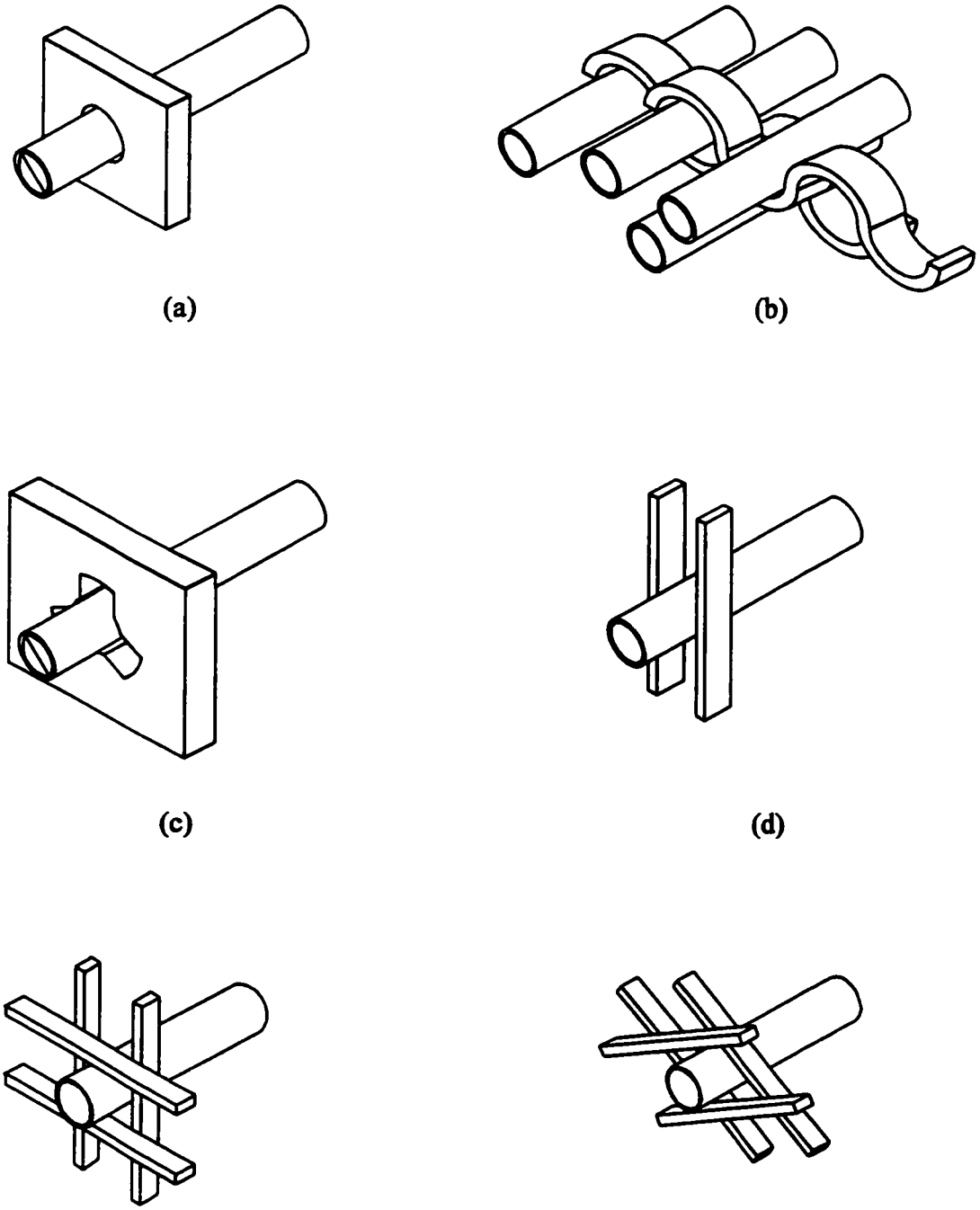

Figure 2.3 Various support configurations. a) drilled holes; b) wiggle bars; c) broached holes; d) flat bars; e) lattice bars (square array); f) lattice bars (triangular array).

As drilled hole support plates were found to promote the accumulation of corrodents and to have the potential of being excessively rigid against thermal expansion, lattice-support structures were seen as an attractive alternative. A lattice type of support may be constructed of flat bars to provide a diamond-shaped support space for each tube (lattice network) as shown in Figure 2.3e. This arrangement provides a very open structure to the flow with line contact support. It therefore reduces the potential for the build-up of deposits.

Lattice bars (in-line arrays) are shown in Figure 2.3f. Large bars are placed on the plane of the U-bends with additional bars being placed perpendicular to them. This arrangement ties the entire U-bend assembly rigidly together. Thus, relative tube motion is prevented at the support, and differential axial tube motion must be absorbed by tube flexing. Although wide bars provide line support contact, they may result in poorly vented spaces. In-line arrays are very open to the flow and have line contact with the tubes. Trapped cavities or stagnant spaces are avoided to minimize problems with dryout or deposition.

2. 4 TUBE DYNAMICS IN THE PRESENCE OF LOOSE SUPPORTS

Supports are installed to both stiffen and brace the tube structure. However, the tolerance dictated by the manufacturing process and the thermal expansion of the tubes requires that these supports be rather loose. Tubes can therefore vibrate freely in the support space and/or impact against their supports. At the design stage, it is customary to consider the heat exchanger tubes to be simply supported at the tube supports. This assumption simplifies the problem, permitting the application of the linear beam theory to compute the system's natural frequencies and its response to various excitation sources. Under this

assumption, the tube will respond as a continuous beam. The supports are assumed to act as knife edge supports, forcing a vibration node at the support location. This type of mode is called "Support-Active". This is a reasonable assumption, particularly in the case of tubes with long spans and a narrow support width with small clearances. However, if the tube has a relatively short span and a large clearance, it may vibrate freely inside the support space for small-amplitude oscillations. A situation in which the support is not effective is called "Support-Inactive".

For intermediate clearances, the tube response strongly depends on the excitation amplitude. For low excitations, the tube will vibrate within the gap, resulting in a support-inactive mode. For large excitations, the tube will be in contact with all of the supports most of the time, resulting in a support-active mode. In some cases, the tube response will be composed of both support-active and support-inactive modes. The effectiveness of the support has a major influence on the system's dynamic characteristics.

The determination of the system's natural frequencies is extremely important to accurately assess the system's integrity, especially against fluidelastic instability. Moreover, the dynamics of the tubes can be analysed using the normal mode theory in which the vibration of a tube is expressed as the superposition of the normal modes. Each normal mode corresponds to a natural frequency of the tube and has a unique vibratory shape. The presence of the gaps at the support introduces nonlinearity to the system. In general, a nonlinear system does not have a definite set of mode shapes and natural frequencies. The natural frequency of the tube can therefore be either the support-inactive or the support-active mode, depending on the excitation and the clearance. The natural frequency of a

support-inactive mode is significantly lower than that of a support-active mode. For instance, the n^{th} natural frequency (f_n) of a single span pinned-pinned tube of length (L), and mass per unit length (m), is given by:

$$f_n = \frac{n^2 \pi}{2L^2}\sqrt{\frac{EI}{m}} \tag{2.2}$$

where I and E are the tube moment of inertia and the elasticity modulus respectively. Figure 2.4 shows the natural frequencies and the mode shapes of this tube considering the following properties:

$I = 2.485 \times 10^{-9}\ m^4$

$E = 1.97 \times 10^{11}$ Pa

$m = 1.404$ kg/m

$L = 1.0$ m

Using Equation 2.2, the first and second natural frequencies are 29.3 Hz and 117.3 Hz respectively. Utilizing the above properties, the two lowest mode shapes and the natural frequencies for a two-span beam with pinned supports are shown in figure 2.5.

Figure 2.6 shows the mode shapes of a two-span tube with a clearance at the centre support. In this case, depending on the amplitude of excitation, particular modes of vibration will occur. For instance, low excitations will result in a small amplitude of vibration. The tube will oscillate inside the support gap without contact as shown in figure 2.6a. In this case, the support is support-inactive and the system will behave linearly as if no support existed in the middle of the beam. This system is equivalent to that of figure 2.4. If the

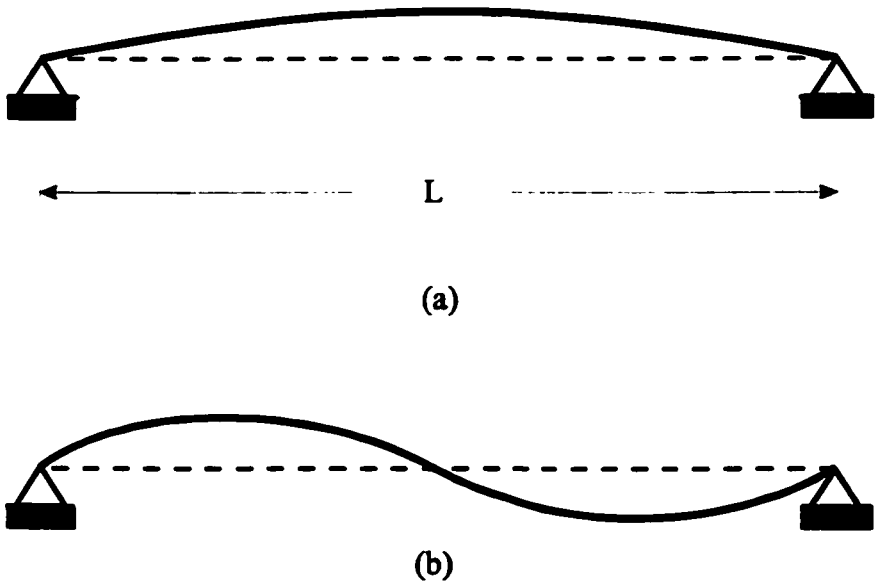

Figure 2.4 Mode shapes and natural frequencies for a single-span tube. a) mode 1 (29.3 Hz); b) mode 2 (117 Hz).

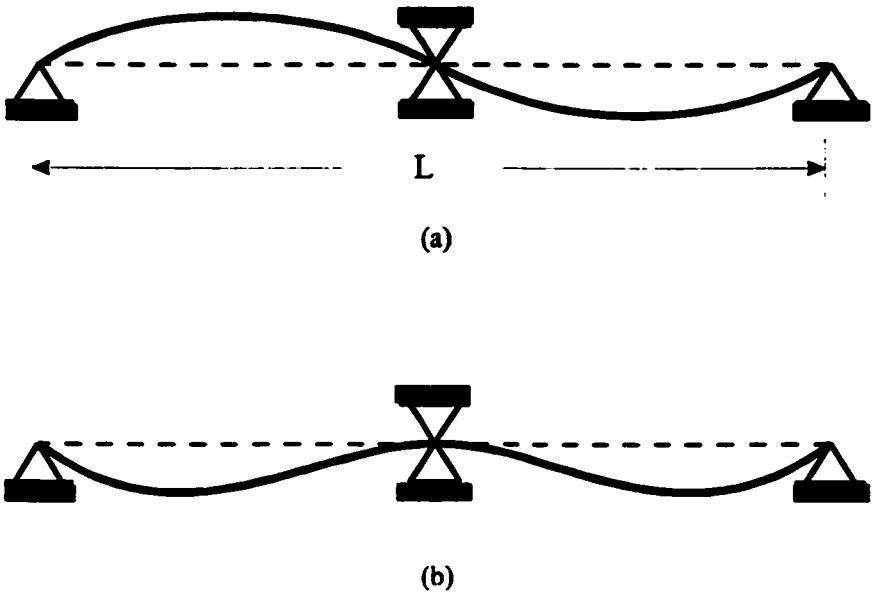

Figure 2.5 Mode shapes and natural frequencies for a two-span tube. a) mode 1 (117 Hz); b) mode 2 (183 Hz)

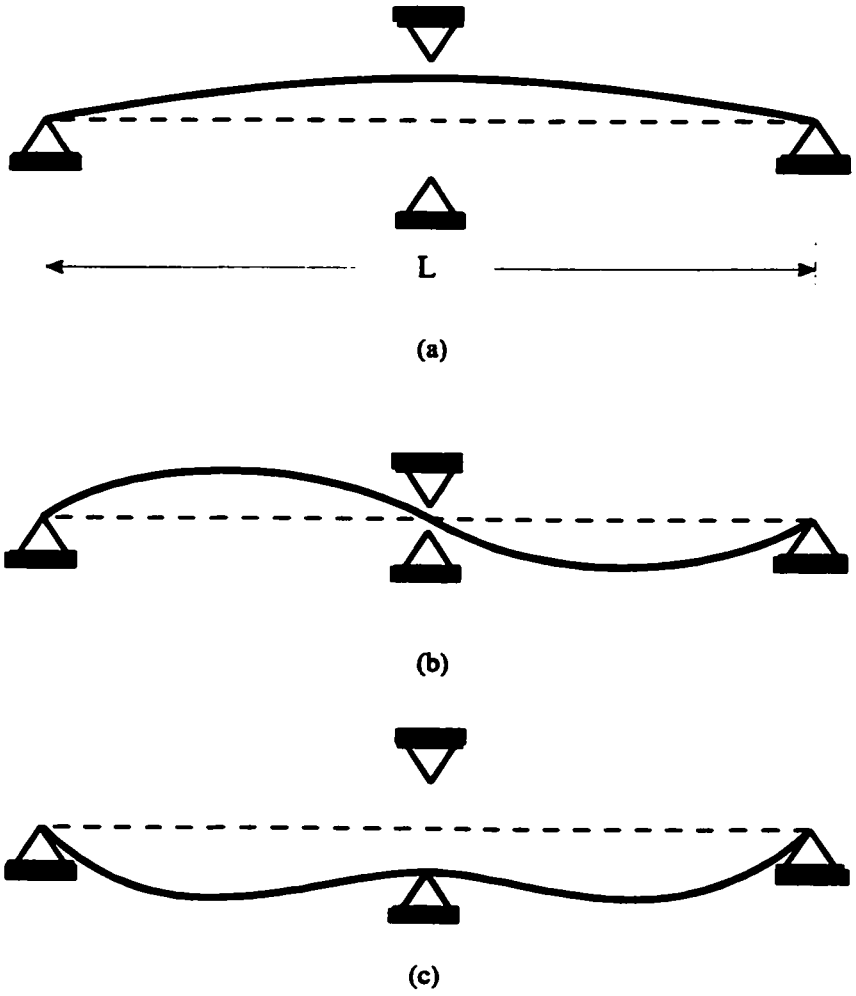

Figure 2.6 Mode shapes and natural frequencies for a two-span tube with clearance at the middle support.
a) 29.3 Hz; b) 117 Hz; c) 183 Hz.

excitation amplitude is large enough that the tube remains substantially in contact with the support, the support may be considered as support active. This is shown in figure 2.6b and 2.6c. In this case, the system is equivalent to that of figure 2.5.

In the case of multi-span tubes, the combined effectiveness of each support must be considered. This was demonstrated by Chen *et al.* (1985) when conducting tests on multi-span tubes with clearances at the supports. The tubes were excited by broadband random excitation. They found that at low excitation amplitudes, the responses were dominated by a group of low frequencies. These frequencies corresponded to the case in which some supports are not in contact with the tube, *i.e.* some supports are inactive. In these modes, the tube vibrates within the clearance of some of the supports. At high amplitudes, the response is dominated by a group of high frequency peaks. These frequencies correspond to the case in which all the supports are active. In the intermediate range of excitation amplitudes, both types of frequencies exist. In addition, Chen *et al.* (1985) found that the natural frequencies of support-inactive modes increase with the excitation amplitude, while those of support-active modes decrease with the excitation amplitude. Moreover, the dominant support-inactive mode for a tube subjected to an excitation depends on both the amplitude and frequency of the excitation.

2. 5 PREVIOUS WORK IN TUBE/SUPPORT INTERACTION

The dynamics of loosely-supported tubes has captured the interest of many researchers. As a result, there has been an increasingly large volume of research and investigative work done on this subject during the past two decades. This includes both

experimental and analytical studies of the problem.

Many experimental investigations were conducted to study nonlinear tube response, and to characterize tube wear (Weaver and Schneider, 1983; Chen *et al.*,1985; Haslinger *et al.*, 1987; Antunes *et al.*, 1990; and Taylor *et al.*, 1995). The work of Chen *et al.* (1985) focussed on the effectiveness of the supports at various excitation levels. Experiments on U-bend tube configurations with flat-bar supports in the bend region were performed by Weaver and Schneider (1983). Their results demonstrated the effectiveness of flat-bar supports in restraining the in-plane tube motion. Other experimental studies utilizing straight or U-bend tubes have been performed using mechanical excitation (Axisa *et al.*, 1984; 1991; Blevins, 1975; Goyder, 1982; Haslinger *et al.*, 1984; 1987; Fisher and Ingham, 1989; and Connors and Kramer, 1991). Numerous experimental investigations were aimed at measuring the normal work rate, which may in turn be used to predict fretting wear.

At the other end of the spectrum, analytical and numerical tools are used to treat the nonlinear boundary conditions of this problem. Piecewise linear approaches were the natural choice for analytical solutions. In this method, the equation of motion is constructed and remains unchanged until the boundary conditions change. In the case of a tube with a single support, two equations of motion evolve. One equation represents the condition of the tube with no contact while the other describes the effect of contact.

The effect of contact is introduced in the second equation through two methods. The first method considers a spring term added at the boundary condition. The usual solution for the associated normal modes is followed (Salmon *et al.*, 1985). The second approach considers the effect of the contact to be an external force determining the particular solution

of the resulting equations (Ting *et al.*, 1979). This approach has been used for simple beam geometries with limited degrees of freedom i.e. a pinned-pinned beam with a support in the middle (Ting *et al.*, 1978; and Salmon *et al*, 1985), and a cantilever beam with a support at the tip (Watanabe, 1981). However, for complicated tube geometries and different support conditions, this method becomes unfeasible.

Numerical investigations, on the other hand, are a powerful tool in treating complex problems. The finite element method has been the numerical technique most widely used for solving the general contact problem. The application of the finite element method to tube/support interaction enabled researchers to investigate a wide variety of tube geometries. Bohm and Nahavandi (1972) employed the finite element method to study the dynamics of reactor internals, including the effect of support impacting. Elliot (1973) did similar work in predicting the response of a vibratory tube impacting on a support. He modelled the vibrational response of a cantilevered beam with a displacement limiting stop at the free end, and the two-dimensional response of a simply supported tube with a mid-span stop. Molnar *et al.* (1976) utilised the linear modal analysis technique to study the dynamics of a piping system which includcd a gap-bumper support. Rogers and Pick (1976) extended this approach and reported a good agreement between both the calculated and the experimental values of the RMS (root mean square) impact forces.

Another approach adopted by a number of researchers is to directly integrate the coupled equations of motion. Such an approach was adopted by Shin *et al.* (1977) who used a nonlinear contact force-deflection relationship. Sauvé and Teper (1987) used the same concept to develop an impact simulation model. In their model, direct integration was

performed implicitly with a variable time step. Later, Sauvé (1997) modified the H3DMAP code utilizing the explicit (central difference) direct integration scheme.

Shah *et al.* (1979) presented simulations of a piping system subjected to seismic excitation. In their model, they utilized modal superposition to solve the piping system dynamics. They also compared the solution obtained by the modal superposition with those obtained by direct integration. The comparison showed that using the modal superposition method significantly reduced the simulation time.

Johansson (1997) presented another model for tube/support interaction. This model is essentially a pseudoforce model with a Newmark direct integration technique. Johansson believed that an instantaneous change in clearance due to wear can change the dynamic properties of the system to a large extent. Therefore, his algorithm permits the contact conditions to change continuously with wear.

Modelling of the support has been successfully carried out and used in simulating support-plates (Rogers and Pick, 1976; Shin *et al.*, 1977; and Sauvé and Teper, 1987). An early study of tubes with loose flat-bar supports was carried out by Yetisir and Weaver (1986). Successful numerical simulations were also reported for flat-bar supports by Antunes *et al.* (1988), Fricker (1991), and Eisinger *et al.* (1995). Fisher *et al.* (1991) presented the mathematical model of the broached-hole support.

Yetisir and Weaver (1986) conducted a theoretical study which investigated the effect of flat-bar supports on the dynamic response of a heat exchanger U-tube. The tube was modelled using beam finite elements, and it was excited at its lowest natural frequencies. The results demonstrated that the dynamics of the system change dramatically as the

excitation level increases. At a low excitation, the tube supports are inactive and all free modes are observed. However, at moderate excitation amplitudes, the tube occasionally impacts the support. The relative modal contributions are then strongly dependent on the excitation level. For higher excitation levels, impacting is regular and the energy is transferred from the lower to the higher frequency modes. This transfer results in the motion of the lower modes being quenched as the higher frequency modes increase in amplitude.

Fisher *et al.* (1989) simulated a cantilever tube with a loose circular support subjected to sinusoidal excitations. A parametric study was conducted on the effects of the radial clearance, the friction coefficient, the tube/annulus stiffness, and the modal damping on the tube/support interaction parameters. It was found that the RMS impact force increases as the radial clearance increases. On the other hand, the contact ratio decreases with an increase in the radial clearance. They also reported that the friction coefficient has a great effect on the RMS impact force and the contact ratio.

Antunes *et al.* (1988) developed a stick-slip friction model based on the Coulomb friction model. They also presented a numerical investigation of tube dynamics in the presence of gaps when the tubes were subjected to random turbulence excitation. Their model utilized a simply supported tube with a loose support (square flat-bar support) near the midspan. The same excitation level was assumed for both orthogonal directions. Their simulations considered a single radial clearance value of 0.1 mm. Several preloads were applied (0 to 50 N) on the tube at the support location to simulate tube misalignments. Their results demonstrated that the normal work rate initially increased as a function of the applied preload, and then gradually decreased. Moreover, they concluded that increasing the friction

ratio decreases the work rate.

Tan and Rogers (1996) developed a force-balance model to simulate the stick-slip friction behaviour. The model developed was tested for a single fuel pin element system. Their simulations covered clearances ranging from 0 to 60 μm. The resulting work rate showed that, when using the slip-stick and the coulomb friction models, simulations consistently underestimated the experimental results. However, the coulomb friction model gave more conservative results, especially for when the clearance was larger than 30 μm.

Axisa *et al.* (1988) calculated the "normal work rate" of a cantilever tube with a gapped support at mid-span. The effect of turbulence and fluidelastic excitation were investigated. Their studies concluded that if turbulence alone was the cause of wear, the wear rate would decrease as the tube-to-support clearance increases. Moreover, they reported that increasing the radial clearance decreased the RMS impact forces and increased the tube response.

Fisher *et al.* (1991) conducted a numerical investigation to study the effect of support type on tube dynamic behaviour. Their simulations addressed the effect of drilled-hole and broached-hole supports, and increased tube-to-support clearances due to chemical cleaning. The study concluded that at similar levels of excitation, the work rate for a broached-hole support is less than that of a drilled-hole support.

Yetisir and Fisher (1996) modelled the U-bend region of a commercial steam generator in an effort to predict the normal work rate of the tubes. Their study assessed the effect of chemical cleaning on the normal work rate. Unlike Axisa *et al.* (1988), they assumed that the tubes are fluid-elastically stable, and estimated the normal work rate due

to turbulence alone. They concluded that the normal work rate decreases with an increase in the support clearance. However, if the clearance increases, the natural frequency of tube decreases. This reduces the critical flow velocity at which the tube becomes unstable, thus increasing the wear rate.

Although the aforementioned investigations have produced abundant numerical and experimental data, much of it requires further interpretation. The shortcoming of the present body of analysis lies mainly in the fact that much of the data produced have been unique to specific configurations and excitations. It is therefore difficult to apply these results to situations involving different flow rates or tube configurations.

Lattice-bar support arrangements are often utilized in the straight leg and U-bend regions in new steam generator designs. The open literature, however, contains virtually no references regarding the effect of these supports on the vibratory behaviour of the tubes. Furthermore, the understanding of tube dynamics in the presence of loose lattice-bar supports and their associated fretting wear patterns is still limited. Although current literature has begun to enhance and refine flow excitation modelling and computational methods used for tube response prediction, there are still many concerns to be addressed. Further study is required to understand and characterize the effect of support characteristics on tube behaviour.

All of the aforementioned tube/support contact models assume that the tube contacts the support over a point. However, the support has a finite width and therefore, the tube/support contact may occur over a segment. Therefore, a new tube/support impact model is required to consider more realistic tube/support contact configurations. The pseudoforce

method in conjunction with modal superposion represents an efficient way in solving the nonlinear equations of tube motion. Therefore, this method will be adopted in this thesis.

The impacting tube motion consists of a number of modes since the tube/support impact excites the higher modes. As a result, the tube/support contact is intermittent where the duration of each contact is of the order of 10 ms, depending on the frequencies of the higher excited modes. Therefore, the classical friction model would be appropriate in modelling such friction conditions. Reasonable tube response predictions have been obtained in the past using the Coulomb's Friction Model (CFM). However, when using both the CFM and the stick-slip model (SSM), the wear work rate has been found to be underestimated (Tan and Rogers, 1996). Additionally, the wear work rate obtained by the SSM is lower than that obtained by the CFM. Since the classical friction model gives a more conservative work rate value, it will be used in this analysis.

CHAPTER 3

TUBE/SUPPORT INTERACTION MODELLING

3. 1 INTRODUCTION

This chapter presents the implementation and verification of the tube/support interaction model. The finite element method was used to describe the dynamics of tubes in the presence of gaps at the supports. The numerical solution of the nonlinear equation of motion was obtained by employing an incremental iterative technique. The temporal integration of the resulting equation of motion was carried out using the Newmark integration method. The algorithm was implemented in an in-house general purpose finite element program. The implemented algorithm was benchmarked by three well documented examples.

3. 2 FORMULATION OF TUBE DYNAMICS

The equation of motion of a structure subjected to arbitrary dynamic loading is expressed in matrix form as:

$$\left[M_L\right]\{\ddot{u}\} + \left[C_L\right]\{\dot{u}\} + \left[K_L\right]\{u\} = \left\{F_e\right\} \tag{3.1}$$

where $[M_L]$, $[C_L]$ and $[K_L]$ are the mass, damping, and stiffness matrices respectively while $\{\ddot{u}\}$, $\{\dot{u}\}$, and $\{u\}$ are the structural displacement, velocity, and acceleration vectors respectively. $\{F_e\}$ is the force vector equivalent to the fluid excitation that takes place in the form of turbulence in the present study. Due to the contact between the tube and its supports, additional stiffness and damping contributions are added to the system matrices. The equation of motion for a structure, including nonlinearities caused by intermittent contact, can be expressed as:

$$[M_L]\ \{\ddot{u}\} + [C_L + C_{NL}]\ \{\dot{u}\} + [K_L + K_{NL}]\ \{u\} = \{F_e\} \tag{3.2}$$

where $[C_{NL}]$ and $[K_{NL}]$ are the nonlinear contributions to the damping and stiffness matrices. These matrices are functions of displacement and velocity and are added to the system when contact occurs.

3. 3 SOLUTION PROCEDURES

3. 3. 1 INTRODUCTION

Transient analysis methods can be divided into two categories: the direct integration

method and the modal superposition method. For nonlinear analysis, the direct integration method of the discretized equation of motion is widely used. On the other hand, for a linear or linearized structural analysis, modal superposition can be utilized. Modal superposition is widely employed because it is cost effective. This is due to the fact that only a few mode shapes are needed to express the response of the system. The selection of the number of mode shapes required for the analysis depends on the frequency content of the excitation force and the natural frequencies of the system. The uncoupled modal equations are integrated analytically, allowing for a larger time step. Moreover, frequencies and mode shapes greatly enhance the physical understanding of the dynamic behaviour of structures.

Modal superposition, however, is often abandoned because a few nonlinearities, such as gaps and friction, may be present in the system. This is essentially true in the dynamic analysis of heat exchanger tubes when impact exists between the tubes and their supports. The dynamics in the presence of impact is a highly nonlinear problem. However, it is sufficient to describe tube motion with beam equations while assuming nonlinearities are strictly localized at the supports. Moreover, instability can be modelled using modes with negative damping. The selection of modes for a reduced modal analysis needs some additional considerations due to the nonlinearities. The reduced modal analysis, when applied, results in a significant reduction in the solution time.

3. 3. 2 PSEUDOFORCE METHOD

The beam equation of motion is discretized in space by the finite element method, and in time by Newmark's method. This equation is solved under the assumption that the

contact forces are known. The mass, damping, and stiffness matrices are computed only once. The corresponding mode shapes and natural frequencies associated with the linear unconstrained system are then extracted. The nonlinear contributions are added to the system through a displacement and velocity dependent external force. The contact forces are computed using a point contact algorithm with Coulomb friction. The pseudo-force vector for the dynamic equation is given by:

$$\{F_{NL}\} = -[C_{NL}]\{\dot{u}\} - [K_{NL}]\{u\} \tag{3.3}$$

The equation of motion therefore becomes:

$$[M_L]\{\ddot{u}\} + [C_L]\{\dot{u}\} + [K_L]\{u\} = \{F_e\} + \{F_{NL}\} \tag{3.4}$$

When there is no impact, the integration of Equation (3.4) may be accomplished analytically assuming that the force vector varies linearly over each time step (Fricker, 1992). Given the displacement and the velocity at the beginning of a time step, as well as the force vector at the beginning and the end of that time step, it is possible to calculate the displacement and the velocity at the end of that time step. However, this is not the case when impact occurs. This is because the force at the end of the time step is unknown since it depends on the displacement and the velocity. Therefore, an iterative procedure is used to calculate the time history of the displacement and the impact forces. In this procedure, the support nodes are monitored to detect overlaps (tube displacements exceeding the support clearance). If any are detected, the displacement vector is used to calculate the contact forces that will oppose these overlaps. These forces are then applied as external forces to the system, and a new

force vector is obtained. This process is repeated until the nonlinear forces converge. Euclidean error norms of the nonlinear forces (Phillips and Taylor, 1973) are used as a measure of convergence. The error in the nonlinear forces is calculated as:

$$E_{NL} = \frac{\left[\sum_{j=1}^{N}\left(\left|F_{NL_j}{}^{i} - F_{NL_j}{}^{i-1}\right|\right)^2\right]^{\frac{1}{2}}}{\left[\sum_{j=1}^{N}\left(\left|F_{NL_j}{}^{i-1}\right|\right)^2\right]} \tag{3.5}$$

where $F_{NL_j}{}^{i}$ and $F_{NL_j}{}^{i-1}$ are the values of the nonlinear forces in the current and the previous iterations for the j^{th} component of the contact force vector (normal contact and friction forces).

3. 4 TUBE/SUPPORT INTERACTION FORCES

3. 4. 1 IMPACT FORCE MODEL

Several models are available for treating the transverse impact of beams. Models such as the momentum balance method are incapable of predicting the values of the impact forces and the deformations during impact. On the other hand, the spring-dashpot model represents a robust method of presenting the boundary forces arising from impact. These boundary forces can be easily integrated into the finite element frame. Using this model, an equivalent spring and damper are introduced. They act in the direction of the tube normal displacement when contact takes place (Figure 3.1). Impact occurs when the tube displacement exceeds the support clearance. Hence, the resulting normal contact forces

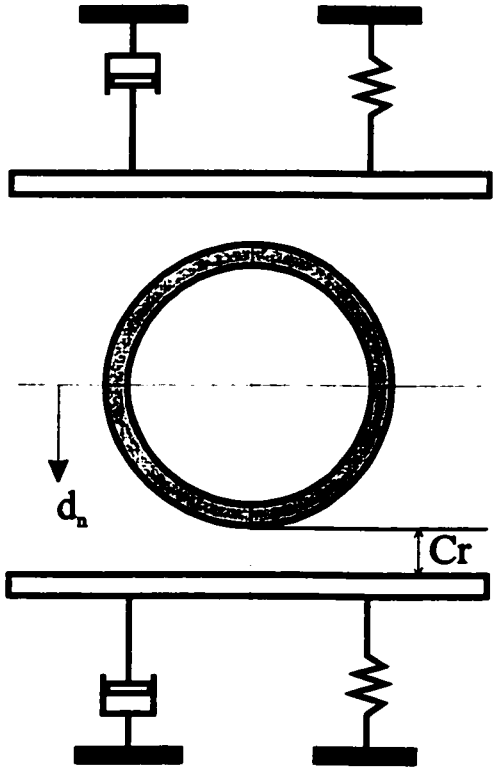

Figure 3.1 Spring-dashpot impact model

(F_{imp}) can be expressed as:

$$F_{imp} = F_{spr} + F_{dmp} \tag{3.6}$$

where F_{spr} and F_{dmp} are the spring and the damping forces respectively. The simplest method of calculating the spring force is to assume a linear stiffness model. The spring force (F_{spr}) is then expressed as:

$$\begin{aligned} F_{spr} &= K_{spr}\delta_n \qquad if \qquad \delta_n > 0 \\ F_{spr} &= 0 \qquad\qquad if \qquad \delta_n \le 0 \end{aligned} \tag{3.7}$$

where δ_n is the support displacement which is expressed as:

$$\delta_n = \left|u_n(t)\right| - Cr \tag{3.8}$$

K_{spr}, $u_n(t)$, and Cr are the equivalent support stiffness, the tube normal displacement and the radial clearance respectively. Spring stiffness (K_{spr}) is physically related to the equivalent stiffness of the contacting bodies. This stiffness is a function of both the tube/support geometry and the material properties. An accurate estimate of the support stiffness can be obtained experimentally. A detailed finite element analysis of the tube and the support bar can also be utilized. Through this analysis, the tube-to-tube support stiffness can be determined as a ratio of the load to the average displacement of the tube cross section in the neighbourhood of the contact area. The problem can be simplified by neglecting the flexibility of the supports in comparison to the flexibility of the tube near the contact area. Satisfactory results have been obtained using the stiffness associated with local ovalization (Axisa *et al.*, 1988). An approximate range of 10^5 to 10^7 N/m has been reported in the literature. A few percent change in the RMS impact force was reported when the stiffness

was increased four times (Rogers *et al.*, 1977). High accuracy in estimating the support stiffness is not often required (Axisa *et al.*, 1988). In order to account for the loss of energy due to impact, the coefficient of restitution was introduced. Hunt and Grossley (1975) used the classical definition of the coefficient of restitution and obtained a nonlinear material damping coefficient. The damping coefficient is then expressed as:

$$C_{imp} = 1.5\beta \; K_{spr}\delta_n \tag{3.9}$$

where β is the material damping coefficient. A value between 0.08 to 0.32 sec/m can be used for steel, bronze, or ivory (Hunt and Crossley, 1975). Finally, the damping forces can be expressed as:

$$F_{dmp} = 1.5\beta \quad K_{spr}\delta_n\dot{\delta}_n \tag{3.10}$$

3. 4. 2 FRICTION

In addition to the aforementioned forces, frictional forces appear when there is tangential motion between the tube and the support. Friction plays an important role in influencing the sliding motion of tubes. The nature of the dynamic friction developed between a tube and its support is a highly nonlinear and complex phenomenon. The mathematical model of friction will be reviewed briefly in this section.

3. 4. 2. 1 CLASSICAL FRICTION MODEL

In the Classical Friction Model, also called Coulomb's Friction Model, the frictional force between two bodies subjected to a normal load is given by:

$$F_f < \mu_s F_N \quad \text{if} \quad V_t = 0 \tag{3.11a}$$

$$F_f = \mu_d F_N \quad \text{if} \quad V_t \neq 0 \tag{3.11b}$$

The frictional force F_f is proportional to the normal force F_N and is either independent of the velocity V_t, or increases slightly as the velocity diminishes. Equation (3.11 b), which represents the condition in which sliding occurs, causes no modelling or numerical problems. On the other hand, numerical problems are encountered when using Equation (3.11a), which represents the sticking or adherence condition. It is strongly nonlinear in the neighbourhood of the zero sliding velocity. In particular, these problems are more pronounced in the transition between sticking and sliding or from sliding to sticking.

It has shown proven experimentally that a small relative motion between contacting bodies is possible even if the tangential force, F_f, is smaller than the static friction capacity. A friction stiffness is therefore utilized to account for the micro-tangential displacement. This modification improves the numerical instability of the solution. Moreover, the Classical Friction Law can be obtained as a special case by setting this friction stiffness to a very large value.

$$F_f = -sign\left(\frac{V_t}{V_o}\right) \mu_s F_N \quad \text{if} \quad V_t \leq V_o \tag{3.12a}$$

$$F_f = -sign\left(V_t\right) \mu_d F_N \quad \text{if} \quad V_t > V_o \tag{3.12b}$$

where V_o is the cut-off velocity. Selecting values for V_o depends on the time step size. Smaller values for V_o require smaller time steps. To economize on computer time, it is

important to make the slope defined by V_o and $\mu_s F_N$ as small as possible without noticeably affecting the simulation results.

3. 5 MATHEMATICAL MODELLING OF FLAT-BAR SUPPORTS

In this section, the modelling of flat-bar supports is presented. Impact and friction forces are derived for a general tube/support configuration. Figure 3.2 shows the unit vectors that define the support orientation as well as the corresponding contact node. $\hat{u}_{sn}$, $\hat{u}_{sa}$, and $\hat{u}_{st}$ are the normal axial and the tangential unit vectors, while $\hat{u}_{tn}$, $\hat{u}_{ta}$, and $\hat{u}_{tt}$ refer to the corresponding tube unit vectors

related to the contact node. Position vectors pointing towards the principal contact node (PCN) and the neighbouring contact node (NCN) are given by:

$$\begin{aligned} \vec{r}^{\,A} &= r_x^A \bullet \hat{e}_1 + r_y^A \bullet \hat{e}_2 + r_z^A \bullet \hat{e}_3 \\ \vec{r}^{\,E} &= r_x^E \bullet \hat{e}_1 + r_y^E \bullet \hat{e}_2 + r_z^E \bullet \hat{e}_3 \end{aligned} \tag{3.13}$$

where A and E denote the principal and the neighbouring contact nodes, respectively. r_x, r_y, and r_z are the components of the respective position vector, while $\hat{e}_1$, $\hat{e}_2$, and $\hat{e}_3$ are unit vectors along the coordinate axes x, y, and z, respectively. A unit vector along the tube axis is calculated using the nodal position vectors as follows:

$$\hat{u}_{ta} = \frac{r_x^A - r_x^E}{\Delta r} \cdot \hat{e}_1 + \frac{r_y^A - r_y^E}{\Delta r} \cdot \hat{e}_2 + \frac{r_z^A - r_z^E}{\Delta r} \cdot \hat{e}_3 \tag{3.14}$$

where Δr is the element length which is given by:

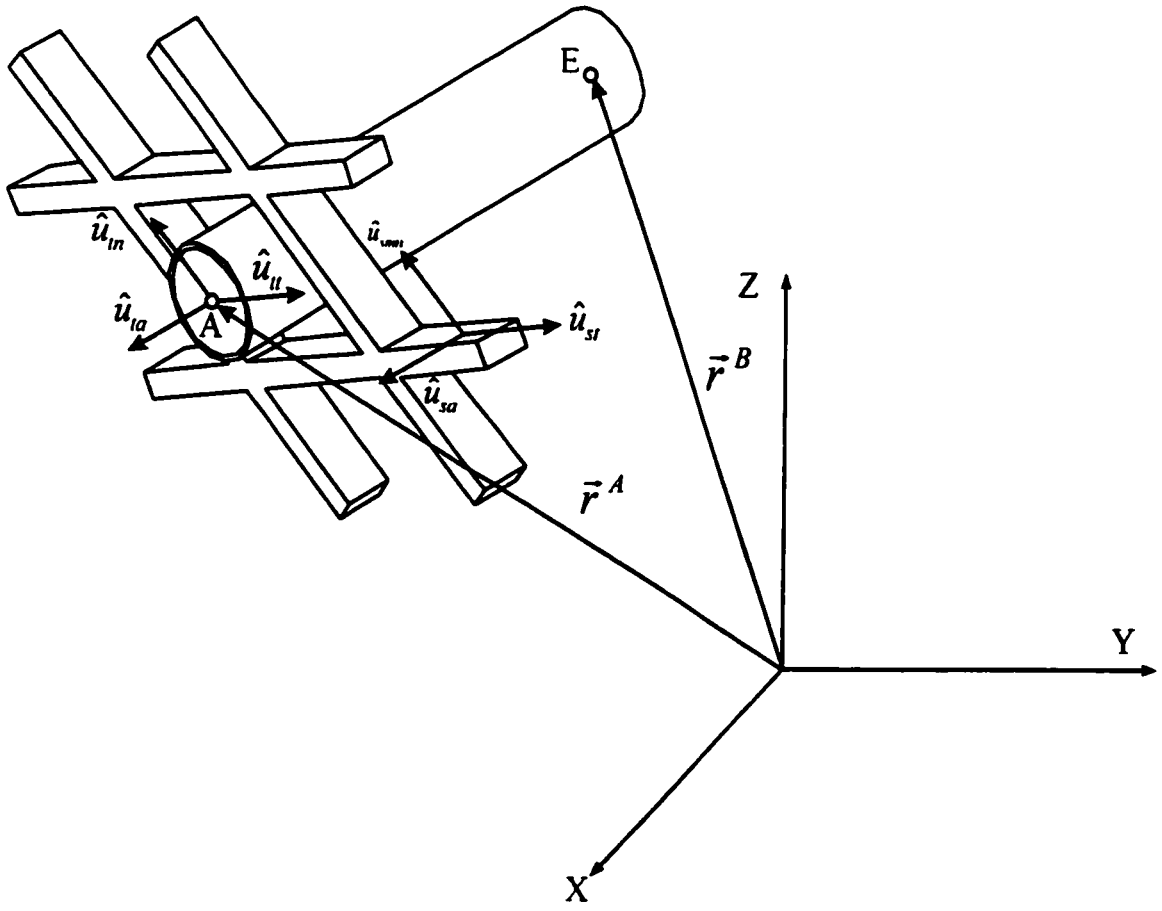

Figure 3.2 Tube and support unit vectors

$$\Delta r = \left[\left(r_x^A - r_x^E \right)^2 + \left(r_y^A - r_y^E \right)^2 + \left(r_z^A - r_z^E \right)^2 \right]^{\frac{1}{2}} \tag{3.15}$$

The tube tangential vector ($\vec{u}_{tt}$) is calculated by the cross product of the tube axial unit vector and the support-normal unit vector:

$$\vec{u}_{tt} = \hat{u}_{ta} \times \hat{u}_{sn} \tag{3.16}$$

The tube tangential vector ($\vec{u}_{tt}$) is then converted to a unit vector ($\hat{u}_{tt}$). The displacement and the velocity of the tube's centre at the principal contact node are given by:

$$\begin{aligned} \vec{d}^{\,A} &= d_x^A \cdot \hat{e}_1 + d_y^A \cdot \hat{e}_2 + d_z^A \cdot \hat{e}_3 \\ \vec{V}^E &= V_x^E \cdot \hat{e}_1 + V_y^E \cdot \hat{e}_2 + V_z^E \cdot \hat{e}_3 \end{aligned} \tag{3.17}$$

where the subscripts *x*, *y*, and *z* denote components in the direction of the global coordinate system.

It is also necessary to calculate the tube's displacement and velocity components (d_n and V_n) in the support-normal direction since this determines whether or not an overlap exists. This is calculated by:

$$\begin{aligned} d_n &= \vec{d} \cdot \hat{u}_{sn} \\ V_n &= \vec{V} \cdot \hat{u}_{sn} \end{aligned} \tag{3.18}$$

Since the tube can impact on any of the flat bars, it is necessary to assign different normal unit vectors for each one. A modified support normal unit vector is created for each flat bar so that this vector always points towards the centre of the tube (Figure 3.3).

$$\hat{u}_{snm} = -sign\left(d_n\right) \hat{u}_{sn} \tag{3.19}$$

In order to compute the contact forces, the normal component of the overlap displacement and the impact velocity must be obtained.

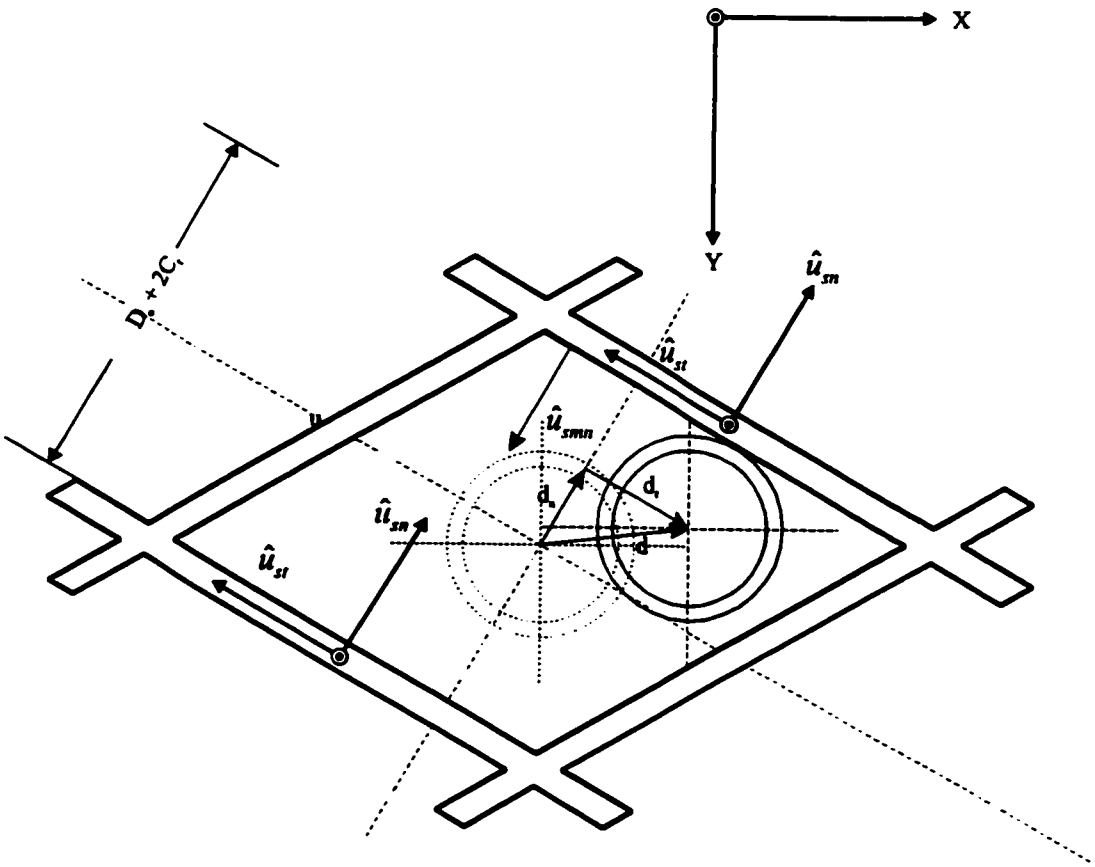

Figure 3.3 Tube in a lattice-bar support model

$$\begin{aligned} \delta_n &= d_n - Cr \\ \dot{\delta}_n &= V_n \end{aligned} \tag{3.20}$$

As was indicated in Section (3.4.1), the spring force $\left(\vec{F}_{spr}\right)$ is equal to the displacement overlap times the equivalent contact stiffness and acts in the outward normal direction of the support surface.

$$\vec{F}_{spr} = \left(K_{spr} \cdot \delta_n\right) \cdot \hat{u}_{snm} \tag{3.21}$$

The damping component of the impact force is in the opposite direction to the normal tube velocity. Now the total impact force is written as:

$$\vec{F}_{imp} = \vec{F}_{spr} + \vec{F}_{dmp} \tag{3.22}$$

If relative motion between the tube and its support is detected, friction forces (F_f) are calculated based on the normal force (F_{imp}), the tangential velocity, and the friction coefficient. Friction forces act along the direction opposite to the resultant tangential velocity. This velocity is the vectorial sum of the tangential and the axial tube velocities. The resultant tangential velocity is given by:

$$\vec{V}_r = \vec{V}_t + \vec{V}_a \tag{3.23}$$

where $\vec{V}_r$, $\vec{V}_t$, and $\vec{V}_a$ are the resultant, the tangential, and the axial tube velocities, respectively. The tangential and the axial velocities are given by the dot product of the principle node velocity vector. The tube tangential and the axial-projected unit vectors are written as follows:

$$\begin{aligned} \vec{V}_t &= \vec{V} \cdot \hat{u}_{tt} \\ \vec{V}_a &= \vec{V} \cdot \hat{u}_{tap} \end{aligned} \tag{3.24}$$

where $\hat{u}_{tap}$ is a unit vector representing the tube's axial projection on the support plane. The friction force acts on the support plane and is calculated by:

$$\bar{F}_f = -\left|F_f\right| \cdot \hat{u}_{rt} \tag{3.25}$$

where $\hat{u}_{rt}$ is a unit vector in the direction of the resultant tangential velocity, while F_f is the magnitude of the friction force which can be calculated using Equations (3.12a and 3.12b). The resultant friction force vector $\bar{F}_f$ acts at the circumference of the tube. When this component is translated to the tube centre, it creates bending and twisting moments. The resultant moment is expressed by:

$$\bar{M}_f = \left(\frac{D_o}{2} \cdot \hat{u}_{snm}\right) \times \bar{F}_f \tag{3.26}$$

where $\bar{M}_f$ is the resultant friction moment which has components along the tube's axial and tangential unit vectors. Finally, these forces and moments are projected on the global coordinates, and added to the global force vector at its respective degrees of freedom.

3. 6 COMPUTER IMPLEMENTATION

The tube/support model presented in Sections (3.4) and (3.5) was incorporated into INDAP (Incremental Nonlinear Dynamic Analysis Program, Dokainish, 1988a). INDAP is an in-house analytical tool capable of solving a wide variety of structural problems including linear and nonlinear static, as well as transient dynamic analysis. For the purpose of flow-induced vibrations analysis, the code was further modified to include an algorithm for

handling turbulence excitation. This algorithm is discussed in Section (3.8). INDAP was written in a modular format to permit both ease of debugging and code efficiency. Due to its open architecture, it is also possible to upgrade the program by adding new modules. In its most recent structure, INDAP is comprised of the following main modules:

1. Preprocessor Module — This module is a user friendly data input computer code which was prepared by using the commands and the parameters of INDAP (Dokainish, 1988b). The specification of these commands and their parameters has no particular order and their names are self-explanatory.

2. Master Organizer — Based on the information supplied by the user and/or the built-in default instructions, this module devises the most effective global strategy for the specified problem.

3. Element Librarian Module — This module performs the kinematic formulation of the finite elements requested by the user. In general, it calculates the linear and nonlinear element stiffness, as well as the mass and the damping matrices.

4. Solver — The main task of this module is to put together the discretized structure and carry out the numerical solution of the assembled structure in conjunction with the specified

boundary conditions. The equilibrium equations are solved by a partitioned frontal solver.

5. Material Module — This is a general mathematical material modelling module. It provides the state of stress for the given kinematic and thermal state, and the current stress-strain relationship for the material at that point.

6. Contact Module — This is a 3-D contact algorithm for a general contact problem. This algorithm detects and removes any compatibility violation between contacting bodies.

The main modules of INDAP are shown in Figure 3.4. A detailed description of the structure and the organization of the program can be found in the user's theoretical and verification manuals (Dokainish, 1988a, 1988c).

The main processor in INDAP is the master routine which controls the flow of data between the different modules. Figure 3.5 shows the flow chart of the master routine in which two main loops can be observed. The most outer loop is set over the time step. The impact routine has a sub-module which searches for overlaps between the tube and the supports. This is achieved by constructing the tube unit vectors and calculating the normal overlap at each support node. The calculated normal displacements are compared to the assigned clearance at each support and hence, the tube/support overlaps are determined. If an overlap is detected, integration is restarted from the previous time step (t) with a smaller

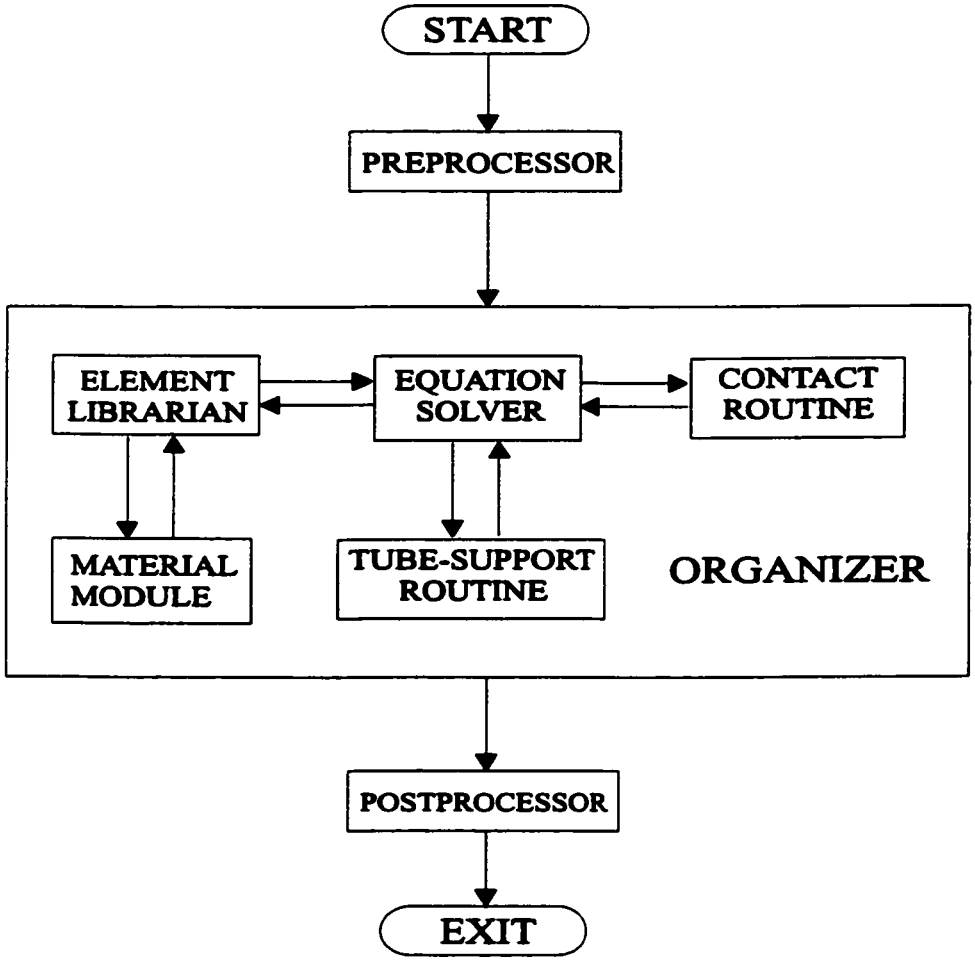

Figure 3.4 General layout of INDAP

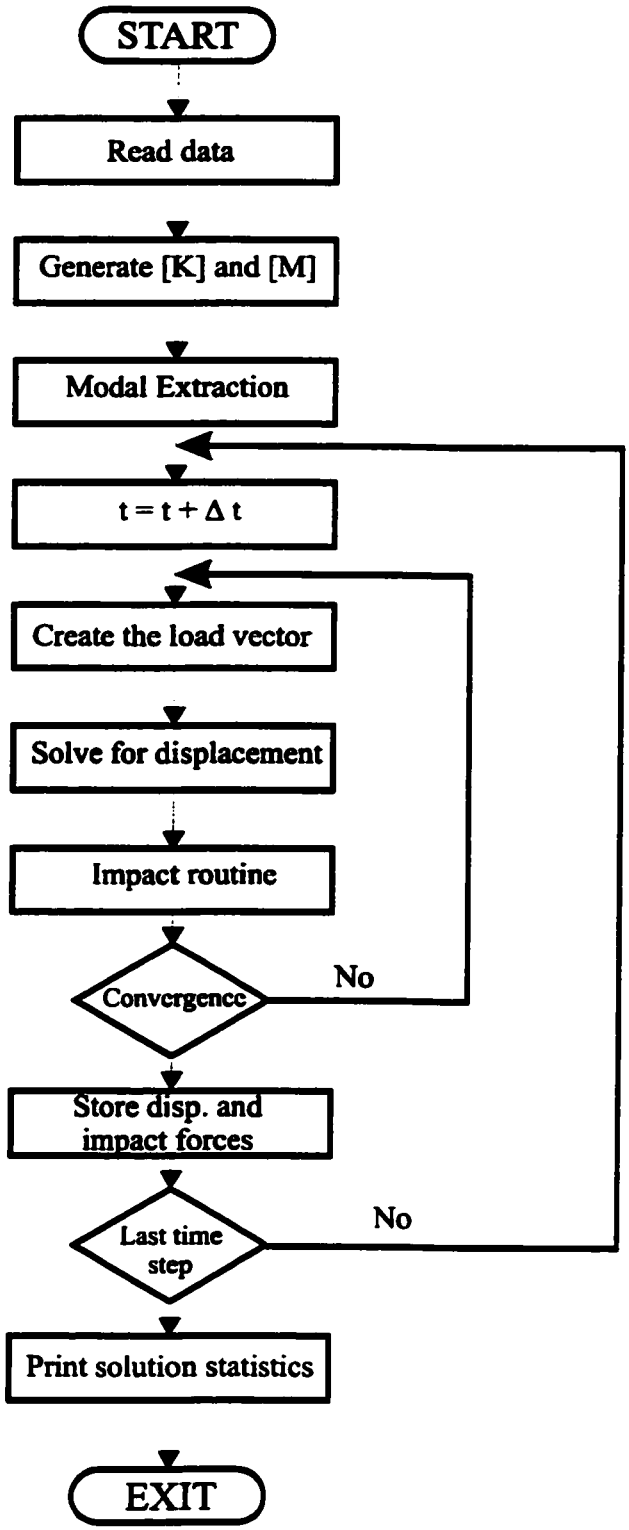

Figure 3.5 Flow chart of INDAP's master module

time step (Δt). Using the new time step, the equations of motion are integrated, and the contact is checked. Once any contact is detected, the tube/support interaction routine is invoked to calculate the impact forces that opposes any overlap. In addition, if sliding motion is detected, the friction forces are calculated according to the friction law. This in turn initiates the inner loop, which is the nonlinear iteration loop. In the nonlinear iteration loop, the contact forces are added to the global load vector. Iteration continues until convergence is achieved. Upon convergence, the time is advanced by a full time step and so on.

3. 7 VERIFICATION CASES

As mentioned earlier, INDAP is written in a modular form which allows addition of new modules. The program is constructed around the effective algorithms and tested for accuracy and speed against the existing algorithms in the literature and the general purpose programs available (Dokainish,1988c). Therefore, in this section, three cases are utilized to only verify the tube/support impact module implemented in INDAP.

3. 7. 1 SDOF SYSTEM

The initial study of the implemented procedure utilized the SDOF model shown in Figure 3.6a. M and K are the system mass and the stiffness respectively. Two symmetric gaps (Cr) with two identical gap stiffnesses (K_g) are present. This problem was solved analytically by considering a series of piece-wise linear systems. It is obvious that the restoring force, $f(x)$, is dependent on the displacement $|x|$. If $|x|$ is less than Cr, the mass is

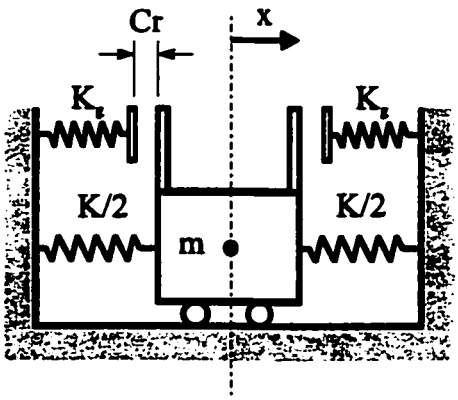

(a)

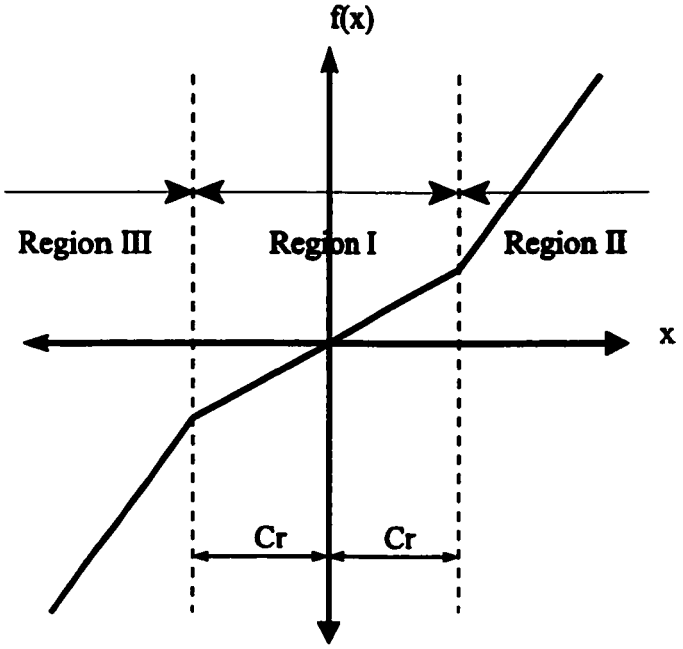

(b)

Figure 3.6 Verification case 1. a) single degree of freedom model b) piece wise linear restoring force

totally controlled by the spring K. When $|x|$ is larger than Cr, the two springs act together as one spring. The force-displacement relation is shown in Figure 3.6b. The restoring force is given as follows:

$$\begin{aligned} &\text{Region I}: && f(x) = Kx && \text{for } -Cr \le x \le Cr \\ &\text{Region II}: && f(x) = Kx + K_g(x - Cr) && \text{for } x > Cr \\ &\text{Region III}: && f(x) = Kx + K_g(x + Cr) && \text{for } x < -Cr \end{aligned} \tag{3.27}$$

Accordingly, the equations of motion are described as follows:

$$\begin{aligned} &\text{Region I}: && M\ddot{x} + Kx = F\sin\omega t \\ &\text{Region II}: && M\ddot{x} + \left(K + K_g\right)x = F\sin\omega t + Cr\,K_g \\ &\text{Region III}: && M\ddot{x} + \left(K + K_g\right)x = F\sin\omega t - Cr\,K_g \end{aligned} \tag{3.28}$$

The system was subjected to an initial velocity V_o, and solved as a free vibration problem. The time needed for the gap to close was obtained. Now, a different system was considered which included an additional stiffness due to contact. The response calculated at the time when the gap was closed was used as the initial condition for the new system. The data pertaining to the SDOF system and the gap parameters are presented below:

K = 400 lb/in $\quad$ K_g = 105 lb/in

M = 100 lb.s^2/in $\quad$ Cr = 1.0 in

V_o = 10 in/s

Using INDAP, the problem was solved utilizing a single beam element whose geometrical and material properties are chosen so that the overall mass and stiffness match those of the SDOF system. A comparison was made between the exact solution and the numerical prediction of INDAP. The comparison indicates an excellent agreement between

the exact solution and the INDAP prediction. Table (3.1) shows the predicted results which include the closure time (the time at which the mass contacts the spring), the maximum response time, the peak displacement, and the maximum impact force.

Table 3.1 Comparison between the exact and the INDAP results for the SDOF case.

	Closure Time (sec)	Max Response Time (sec)	Max Response (in)	Max Impact Force (lb)
Exact	0.10067	0.14987	1.30528	0.30528×10^5
INDAP	0.10070	0.14990	1.30531	0.30531×10^5

3. 7. 2 SINGLE-SPAN TUBE

The objective here was to verify the general behaviour of both the impact and the displacement time traces. The INDAP prediction was compared with a documented case (Yetisir 1987) to examine the validity of the implemented algorithm. Yetisir's model utilizes a cantilever tube with a loose support at the free end. The tube is 1 m long with a 15.88 mm outer diameter, and a 10.03 mm inner diameter. The elastic modulus and the mass density are 230 GPa and 7920 kg respectively. The tube was excited by a sinusoidal force at its tip. Thirty-two modes, each with a 1% critical damping, were used in the analysis. The computation was performed using a constant time step of 0.1 ms. The displacement and the force/time histories of both the documented case (Yetisir 1987) and INDAP are shown in Figure 3.7. The comparison indicates a good agreement in the displacement trace, as well as in the impact force and the duration.

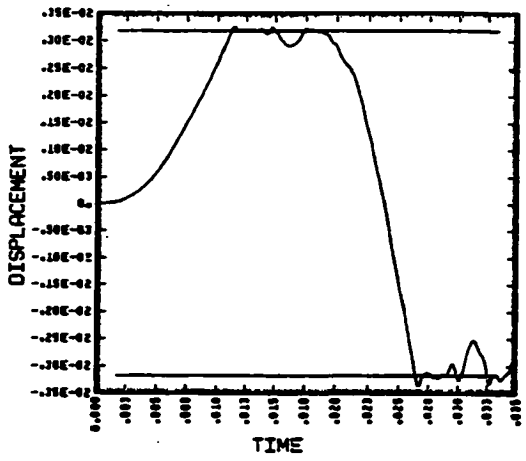

a) Yetisir (1985)

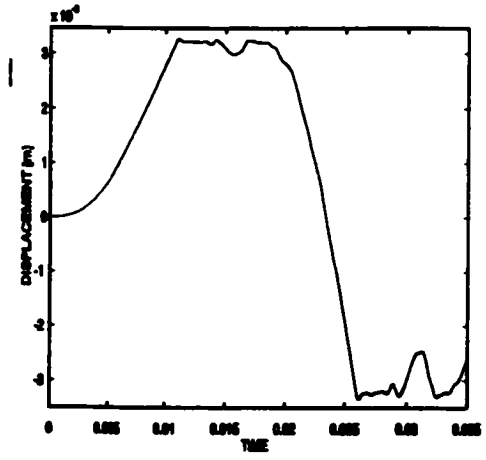

b) Current work

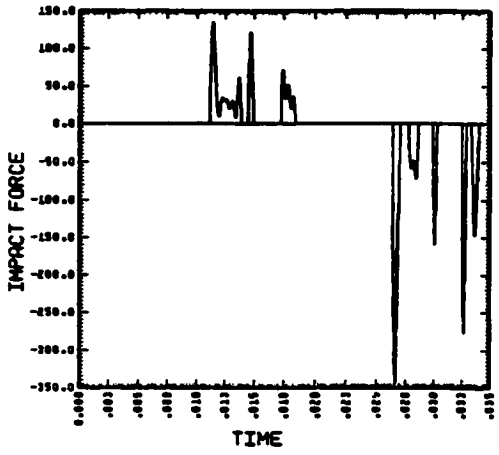

c) Yetisir (1985)

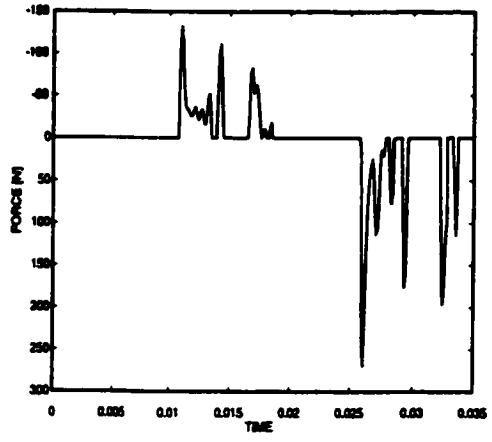

d) Current work

Figure 3.7 Displacement and impact force traces for a single-span tube

3. 7. 3 MULTI-SPAN TUBE

Sauvé and Teper (1987) developed a direct implicit (Newmark) integration code, H3DMAP (Hydro 3 Dimensional Matrix Analysis Program) to simulate the nonlinear dynamic-impact response of multi-supported tubes. They presented simulation results for a four-span model of a typical process equipment arrangement subjected to high flow forces (Figure 3.8). The flow excitation was modelled as a distributed force with alternating directions over each span. Thirty-two modes were used in the analysis. The time history of the response was obtained for a number of clearances for ten driving cycles (0 to 0.25 sec). The comparison between the published traces (displacement and impact force time traces) and those obtained using INDAP shows a good agreement (Figure 3.9). The RMS of the impact forces at all supports was obtained over the 5th to the 10th driving cycle. The same example was used by Fisher *et al.* (1989) to verify the VIBIC (VIbration of Beams with Intermittent Contact) code which utilized an explicit time integration of the modal equations of motion. Figure 3.10 shows the predicted RMS impact force at each support for four different radial clearances along with comparisons of the predictions by H3DMAP and VIBIC. The predicted RMS impact forces obtained by INDAP agree reasonably well with those of H3DMAP and VIBIC, there are being no systematic differences between the predictions of the three codes.

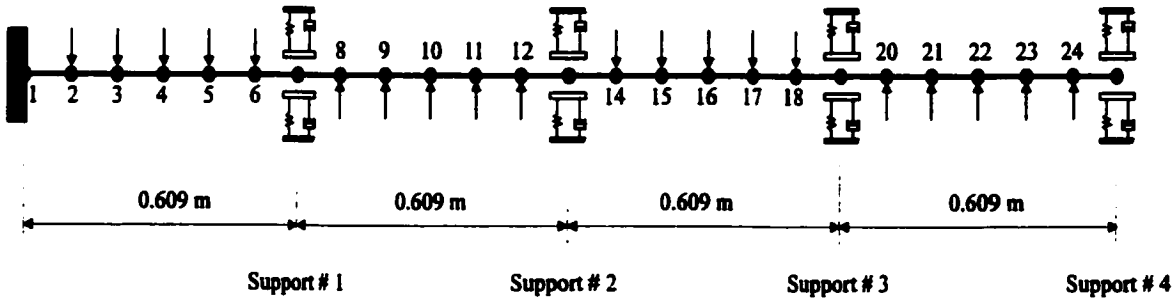

Tube : 2.436 m Long
15.9 mm OD
13.6 mm ID

Material : $E = 2.07 \times 10^{11}$ Pa
$\rho = 7.87 \times 10^3$ kg/m^3

Support : $K_{gap} = 1.75 \times 10^7$ N/m
$C_{gap} = 0.28$ N.s/m

Damping : $C = \beta M + \gamma K$
$\beta = 0.1526$
$\gamma = 1.7983 \times 10^{-5}$

Forcing Function : $F_i = 4.2 \sin(2\pi f t)$ i = 2-6, 14-18
$F_i = -4.2 \sin(2\pi f t)$ i = 8-12, 20-24
$F_{25} = 2.1 \sin(2\pi f t)$ f = 40 Hz

Figure 3.8 Four-span tube subjected to high flow forces (Sauvé and Teper 1987)

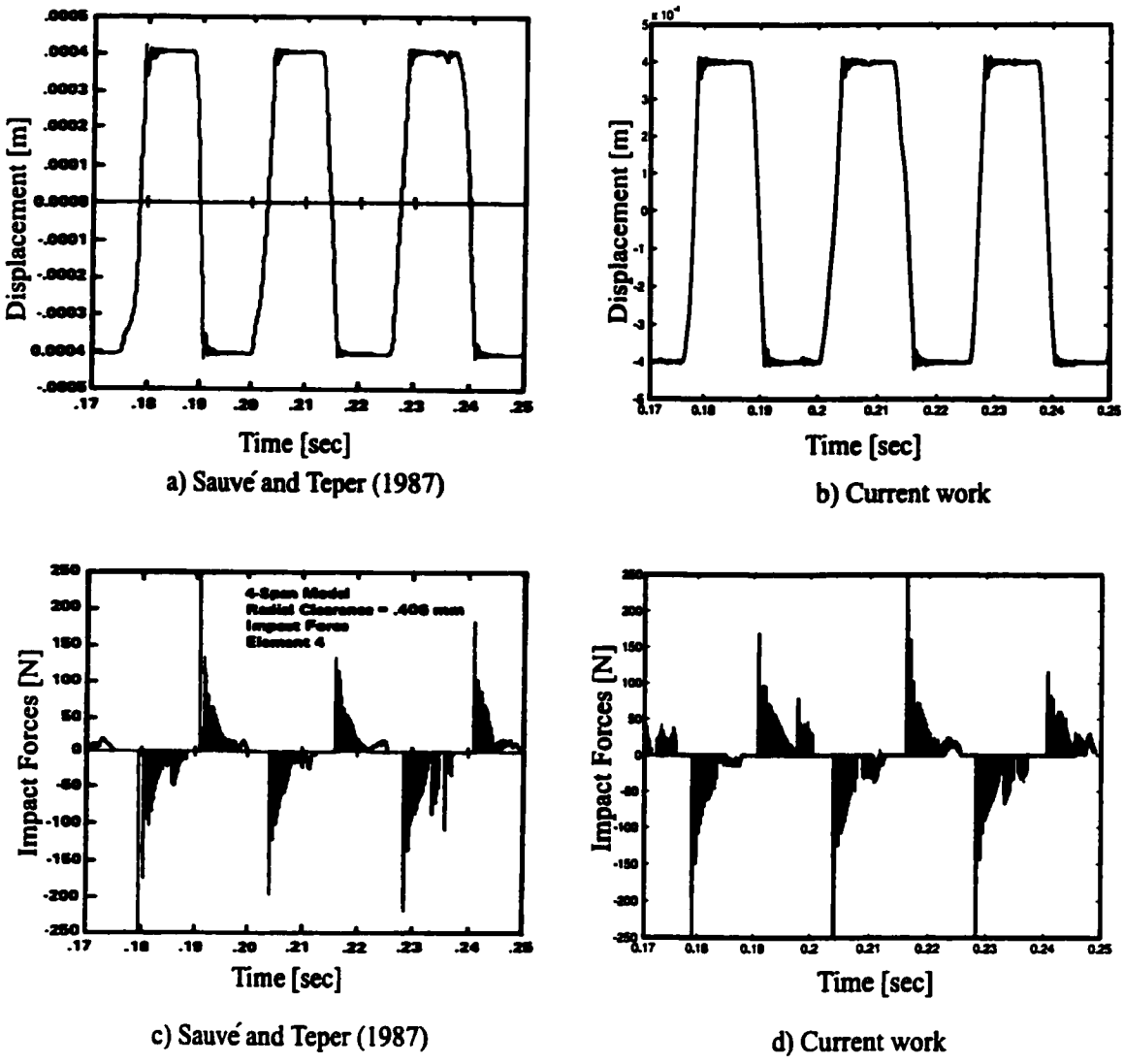

Figure 3.9 A comparison of the displacement and impact forces traces for a multi-span tube

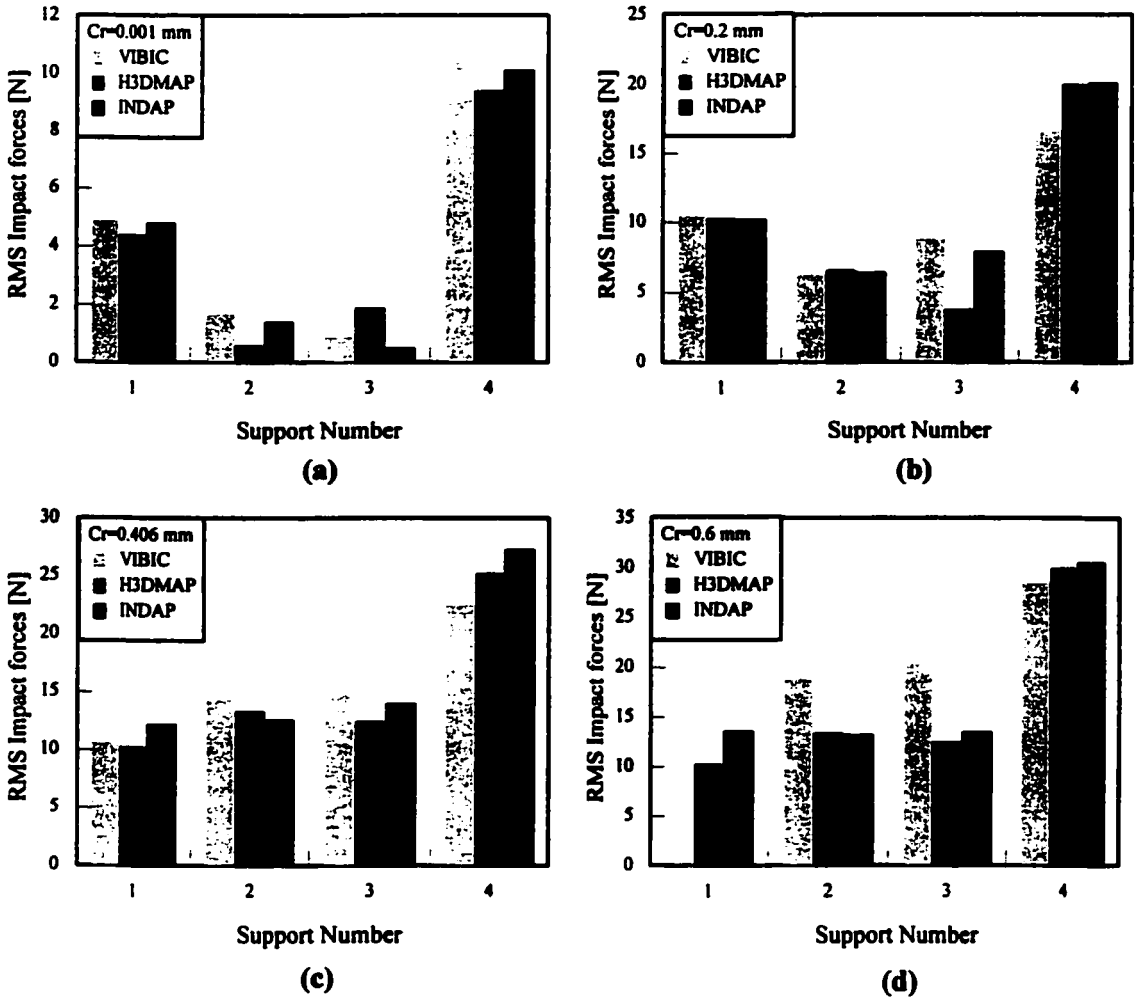

Figure 3.10 Comparison of the RMS impact force for different radial clearances

3. 8 TURBULENCE MODELLING

3. 8. 1 INTRODUCTION

The turbulence excitation mechanism often dominates the flow-induced vibration of tubes within heat exchangers and steam generators. The case of crossflow-induced random vibration due to turbulence is often referred to as buffeting. The turbulence-induced random vibration of a tube bundle, sometimes called the sub-critical vibration, is usually of a much smaller amplitude than that experienced in fluidelastic instability. This mechanism is usually characterized by a relatively low-amplitude excitation, which leads to long-term fretting wear and possible tube failure. Hence, turbulence-induced random vibration can determine the long-term reliability of steam generator tube bundles. To study the effect of turbulence, force coefficients are needed to calculate the tube response. These force coefficients can be obtained from the turbulence bounding spectra. Figure 3.11 shows the turbulence bounding spectra given by Oengören and Ziada (1995) which expresses the PSD of turbulence forces (S_{FF}) in nondimensional form ($\widetilde{S}_{FF}$):

$$\widetilde{S}_{FF} = (\frac{1}{2}\rho U^2 D)^2 \frac{D}{U} S_{FF} \tag{3.29}$$

where D, ρ, and U are tube diameter, flow density, and flow velocity, respectively.

3. 8. 2 SPECTRAL ANALYSIS OF THE TURBULENT FORCES

A number of assumptions are usually employed to simplify the random vibration analysis and make it tractable:

1. The fluid excitation forces are assumed to be independent of the deformation of the structure. Deformation independence excludes such phenomena as flutter,

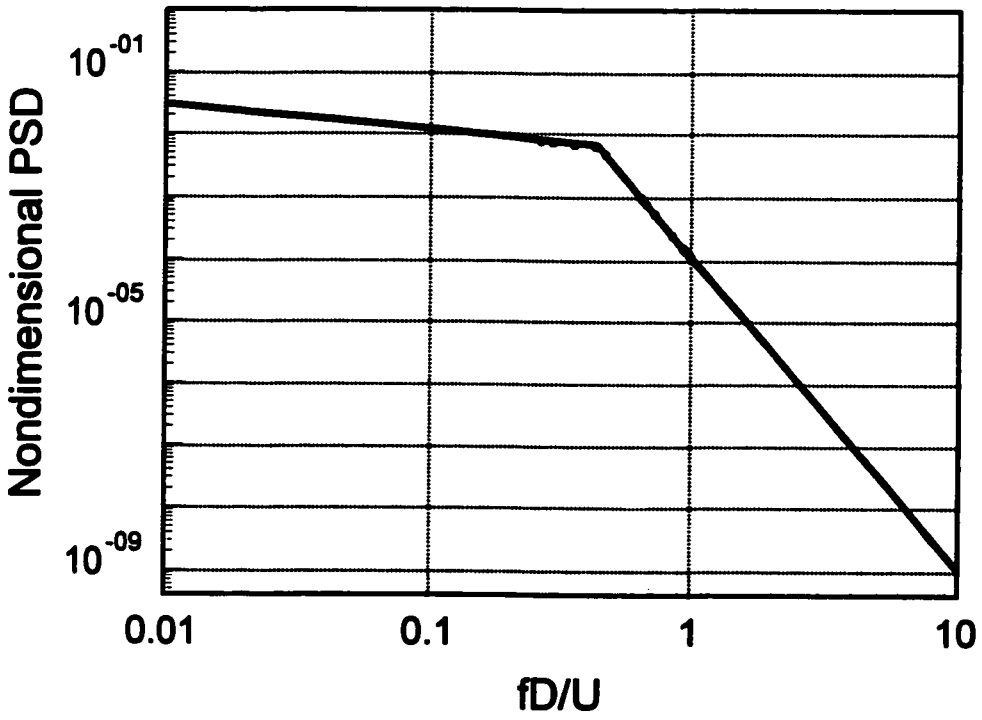

Figure 3.11 Turbulence bounding spectra given by Oengören and Ziada (1995).

galloping (a strong feedback between the structure deformation and the fluid force), and vortex shedding resonance.

2. The turbulence forces can be modelled as a stationary random process. This means that the time-averaged statistical characteristics of the turbulence are nearly independent of the start and finish time of an averaging interval.

3. The structure responds linearly to the imposed forces.

These assumptions have been validated experimentally.

3. 8. 3 RANDOM TIME HISTORY FORCE GENERATION

This section presents the method adopted to generate a random forcing time history based on an input power spectral density (PSD) profile. Turbulence excitation forces can be assumed to have a zero mean, so that the turbulent force time history, $F(t)$, can be written as:

$$F(t) = \sum_{i=1}^{N} A_i \sin\left(2\pi\ f_i t + \phi_i\right) \tag{3.30}$$

In the above equation, the excitation force is expressed as a summation of N harmonics. Each of these harmonics has an amplitude A_i, with a frequency f_i, and a phase angle ϕ_i. The phase angle ϕ_i is assumed to have an equal probability between zero and 2π. The mean square value, $\overline{F}^2$, of $F(t)$ is the sum of the mean square value, $\overline{A_i}^2$, of each harmonic component. Hence:

$$\overline{F}^2 = \sum_{i=1}^{N} \frac{\overline{A}_i^2}{2} \tag{3.31}$$

The power spectral density $S(\omega_i)$ is defined as the density of the mean square value in an

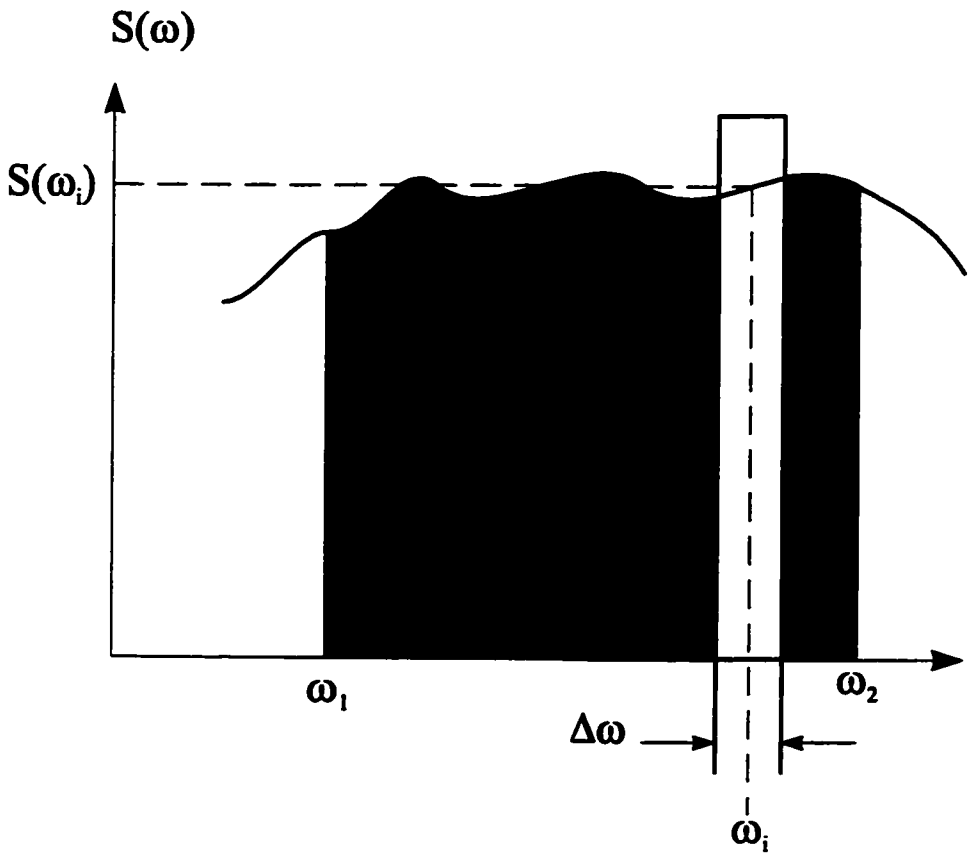

Figure 3.12 General PSD curve

interval (Figure 3.12), i.e.:

$$S(\omega_i) = \frac{\overline{F_i}^2}{\Delta\omega} \tag{3.32}$$

Therefore, the amplitude of each component can be expressed in terms of the PSD as follows:

$$\overline{A_i}^2 = 2\Delta\omega\, S(\omega_i) \tag{3.33}$$

Thus, *F(t)* becomes:

$$F(t) = \sum_{i=1}^{N} \left[2\Delta\omega\, S(\omega_i)\right]^{\frac{1}{2}} \sin(\omega_i t + \phi_i) \tag{3.34}$$

The aforementioned expression gives a direct relation between the PSD for turbulent forces and the force/time history.

3. 8. 4 IMPLEMENTATION IN INDAP

The procedure for generating a time domain forcing function was implemented in INDAP. This procedure permits the random forcing application of both the concentrated and the distributed forces on the beam element. As was mentioned in Section (3.8.3), a phase angle ϕ_i has to be chosen randomly. A random shuffle procedure was used to eliminate the possibility of having a sequential correlation between these random numbers (Sauvé 1995).

3. 8. 5 VERIFICATION CASES

In order to examine the validity of this procedure, a number of tests were performed. The examples presented in this section were analysed using the implemented routine in INDAP and the numerical results were compared to the analytical solution.

3. 8. 5. 1 SINGLE DOF

A SDOF system was used since it is very simple and the analytical solution available for such a problem can be obtained. The data for the problem is given in Figure 3.13. A limited-band white noise with a power of 1.0 lb^2/Hz over a range of 0 to 50 Hz was applied to the system. The root mean square (RMS) of the SDOF resonance response to a broad-band force excitation is (see for example, Thomson and Dahleh,1998) :

$$y_{rms} = \left[\frac{S_{FF}(f)}{8\omega_n^3 M^2 \zeta} \right]^{\frac{1}{2}} \tag{3.35}$$

Substituting the system values into Equation (3.35) yields $y_{rms} = 0.0088627$ in.

INDAP was used to solve this problem by utilizing the implemented procedure. The solution was obtained using both zero and a random phase angle ϕ_i. In both cases, the simulation was carried out over 10 seconds of simulation time using time increments of 1 msec. The limited-band white noise was discretized using increments of 0.5 Hz. INDAP results demonstrate good agreement with the exact solution as shown in Table 3.2, especially for the case of random phase.

Table 3.2 Comparison of the INDAP prediction and the exact solution for the SDOF case

	$\phi = 0$	$0 \le \phi \le 2\pi$
Analytical	0.0088627	0.0088627
INDAP	0.0086054	0.0088179

3. 8. 5. 2 SIMPLY SUPPORTED BEAM

The simply supported tube under consideration, as well as its geometric and material data, are shown in Figure 3.14. A limited-band white noise was applied as a distributed load. The PSD of the white noise is 0.01 lb^2/Hz covering the frequency range of 0 to10 Hz. The analytical frequency domain solution for the RMS mid-span response of a simply supported beam vibrating at its fundamental frequency under uniform loading is given by:

$$y_{rms} = \left[\frac{S_{FF}(f_1)}{4\pi^5 f_1^3 m^2 \zeta_1} \right]^{\frac{1}{2}} \tag{3.36}$$

The analytical solution yields an RMS response at the mid-span of 0.1829 in. A simulation using INDAP was carried out over 100 seconds using time increments of 1 msec. The simulation results are summarized in Table 3.3. The corresponding INDAP time domain solution agrees well with the analytical results provided that the frequency resolution is sufficiently fine, $\Delta f \le 0.1$ Hz.

Table 3.3 A comparison between the INDAP predicted and the exact solution for a simply-supported tube

Δf [Hz]	y_{rms} [in]
1	0.1177
0.5	0.1253
0.1	0.183

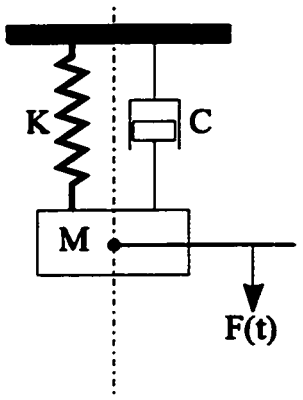

Mass M=0.2533 lb.s^2/in
Stiffness K=1000 lb/in
Damping ratio ζ=0.1

Figure 3.13 Single degree of freedom verification case

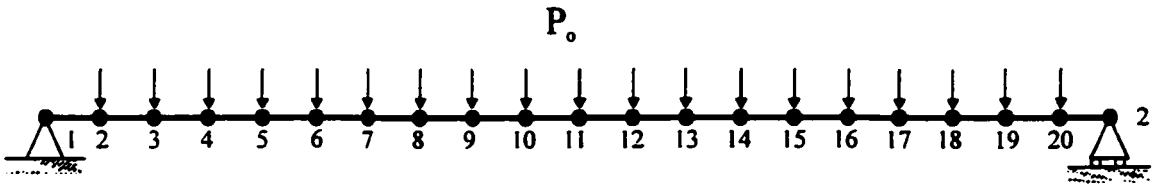

Tube :	36	in Long	Material :	E=	28x10^6	psi
	0.625	in OD		ρ=	0.289	lb/in^3
	0.536	in ID				

Fundamental Frequency : f_1 = 2.455 Hz ζ=1%

Forcing Function :
Limited-band White Noise
a-Freq range 0 to10 Hz
b-PSD 0.01 lb^2/Hz

Figure 3.14 Simply supported beam verification case

3.9 SUMMARY

This chapter describes the implementation and validation of the tube/support interaction model in a general purpose in-house finite element program (INDAP). Pseudo-forces were utilized in conjunction with the familiar modal superposition to solve the nonlinear equations of motion. The mathematical modelling of the flat-bar supports was described in detail. The implemented model was bench-marked by a SDOF system for which the analytical solution is available. In addition, two published examples were used to validate the implemented model. The comparison indicated a good agreement between the implemented model and the comparison examples. In addition, a procedure to generate random force time histories was presented and implemented in INDAP. The implemented procedure was verified by several examples which have an analytical solution. The implemented procedure is very useful for analysing cases where the frequency domain solution is not available. A typical example is tubes with loose supports which require nonlinear time-domain solution of tube/support impacting. Moreover, it permits the utilization of appropriate turbulence bounding spectra.

CHAPTER 4

PARAMETRIC STUDIES AND SCALING

4. 1 INTRODUCTION

In this chapter, the implemented tube/support model will be utilized to study the nonlinear response of heat exchanger tubes subjected to turbulence-induced forces. The turbulence forces will be modelled as a combination of a fluctuating-force component and a steady drag component. A set of non-dimensional parameters are introduced to collapse the obtained results. These dimensionless parameters are used in examining the case of a multispan tube. The effect of the support arrangement, the flow orientation, and the support offset on the tube dynamics will also be investigated.

4. 2 EFFECT OF THE STEADY DRAG FORCES

Heat exchanger tubes are usually subjected to a significant level of turbulence at the entrance region. Tubes in this region can usually be modelled as straight tubes. The system under consideration consists of a straight tube which is fixed at one end and loosely-supported at the other end (Figure 4.1) and subjected to a turbulent cross-flow of air. The lattice bars are arranged for a triangular array (60° included angle). As it was indicated earlier, an accurate estimate of the support stiffness is not required (Axisa *et al.*, 1988). The support stiffness used in this analysis (10^6 N/m) should give reasonable and consistent results. Damping at the support may vary in the range of 0 to 50 N sec/m with a negligible effect on the results (Fricker, 1992). Literature reported a range of 0.1 to 0.4 for the coefficient of friction. Haslinger and Steininger (1995) recommended values of 0.36-0.4 for flat-bar supports. In this analysis, a single coefficient of friction value of 0.1 will be utilized since this value represents the lower bound. The overall tube length is 2 m with an outside diameter of 0.015 m, and a wall thickness of 0.00235 m. The tube's mass per unit length is 0.7397 kg/m and the Young's modulus is 2.3×10^{11} Pa. The first twenty-four unconstrained modes, excluding the axial and the twisting modes, were calculated and used in these simulations. The predicted tube natural frequencies for the fixed-free and the fixed-hinged configurations are shown in Table (4.1).

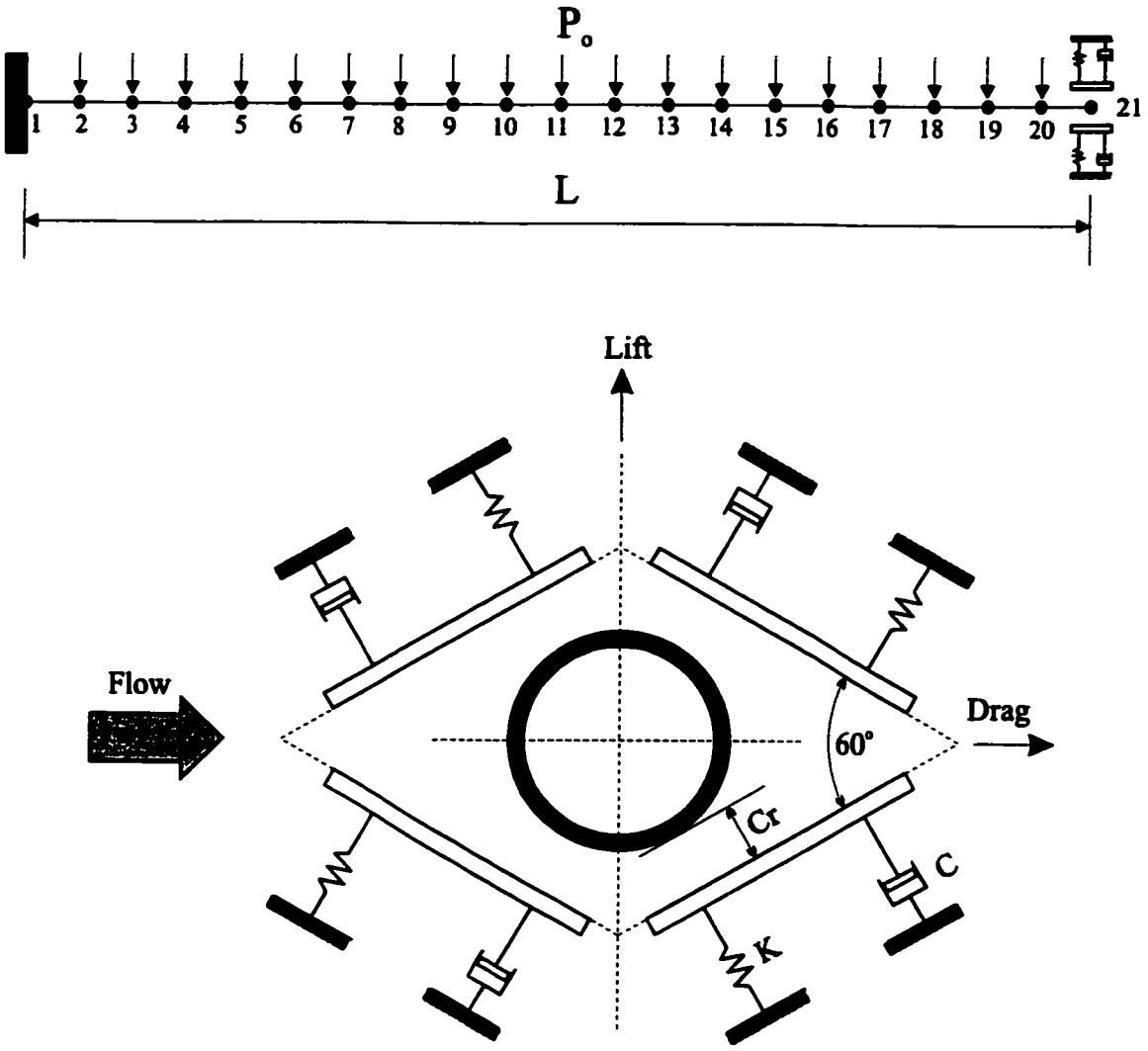

Figure 4.1 Finite element model of a loosely supported cantilever tube

Table 4.1 The predicted natural frequencies of the tube with support-active and support-inactive

	Mode 1	Mode 2	Mode 3	Mode 4	Mode 5
Support-active	3.429	21.49	60.18	117.9	195
Support-inactive	15.04	48.74	101.7	173.9	265.4

4. 2. 1 TURBULENCE EXCITATION

The bounding power spectral density (PSD) measured by Oengören and Ziada (1995) was utilized to generate the time-domain fluid forces. Depending on the flow velocity and the tube's diameter, the PSD curve of turbulence excitation is obtained. This PSD curve is then transformed into a force-time record using the inverse Fourier transform algorithm described in Chapter 3. The resulting fluctuating forces are Gaussian in nature with a zero mean value. Two different force versus time records were used to represent the fluid excitation in the lift and the drag directions. The lift force record only contains the fluctuating force component with a zero mean. On the other hand, the drag force record consists of the fluctuating force component superimposed on a static component which represents the steady drag forces. These are then input into the nonlinear tube support model.

4. 2. 2 RESULTS AND DISCUSSION

For each support case study, the response time history was computed over twenty seconds. A wide range of radial clearance values ranging from 0.001 mm to 1 mm was examined. Because of the clearance, the tube can respond in different modes depending on

the effectiveness of the support. As discussed in Chapter 3, the effectiveness of the support is categorized as either support-active or support-inactive (Chen et al., 1985). For the model under consideration, support active means that the tube's boundary conditions are considered as fixed-hinged. On the other hand, the support-inactive yields a fixed-free end condition. These two modes are shown in Figure 4.2.

4. 2. 2. 1 RESPONSE SPECTRA

Figure 4.3 shows the PSD of the response in the lift direction at node 2. The spectra presented are for the tube with different clearance values subjected to the same flow velocity (4 m/s). Depending on the clearance value, two groups of frequency peaks can be easily identified. For a small clearance (Figure 4.3a), the PSD of the tube response is dominated by frequencies corresponding to the natural frequencies of the fixed-hinged configuration (support-active). At large clearances, the PSD of the tube response is dominated by the free modes of the tubes (support-inactive) as shown in Figure 4.3d. Figures 4.3b and 4.3c depict the PSD of the tube response for an intermediate clearance where a transition takes place between the modes. This behaviour is known as the mode switch and was also observed by Chen et al. (1985). Note that the response spectra for the intermediate cases appear noisy with rather poorly defined natural frequencies.

4. 2. 2. 2 CONTACT RATIO

Contact ratio is defined as the ratio of the tube-to-support contact duration to the total time. Figure 4.4 shows the contact ratio (Ct) for various flow velocities. Increasing the flow velocity increases the contact ratio. For a given flow velocity, the contact ratio remains

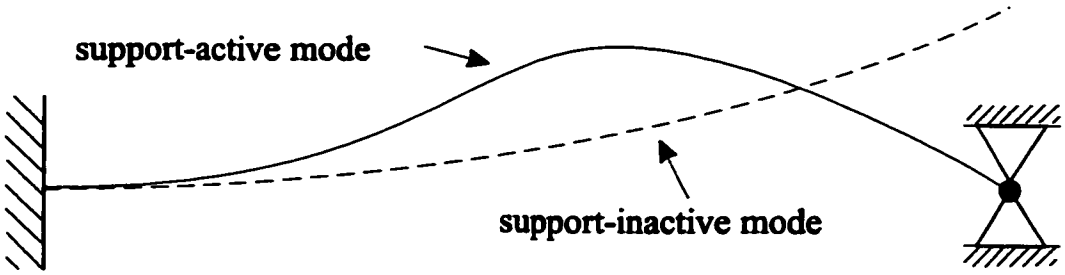

Figure 4.2 Support-active and Support-inactive modes

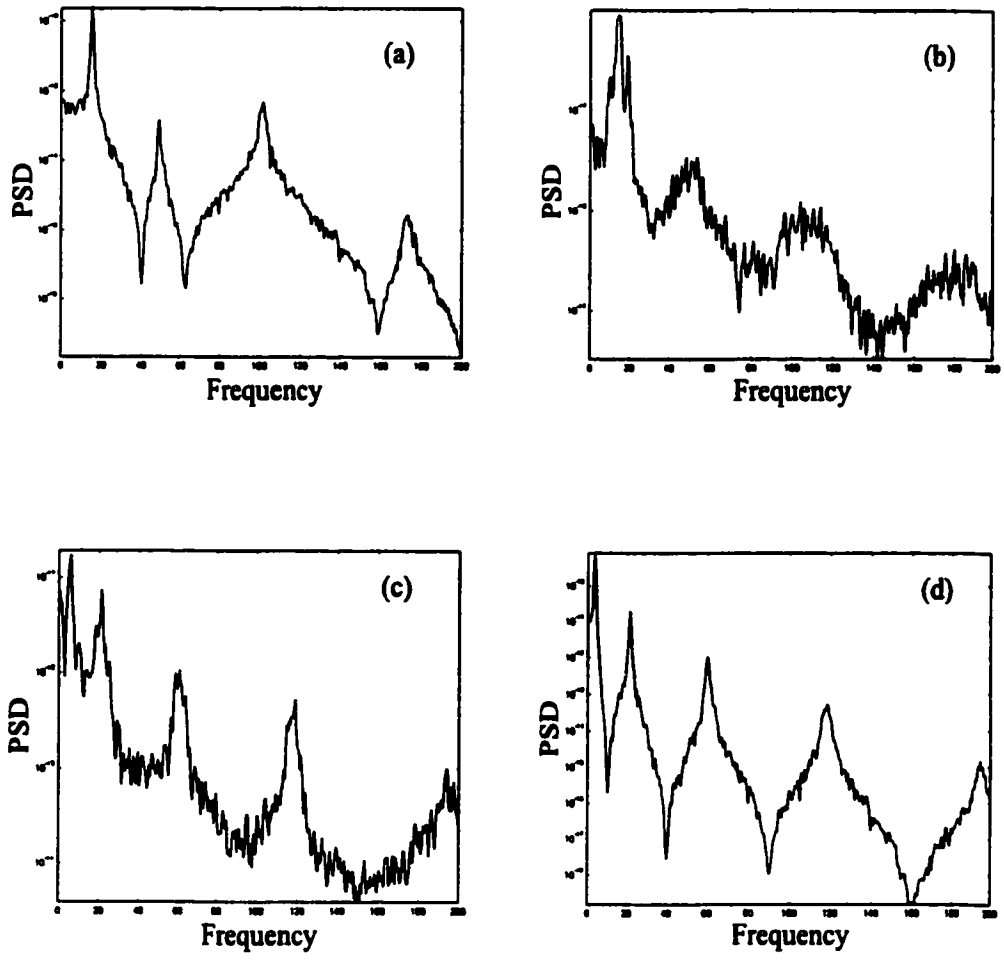

Figure 4.3 Response spectra for various clearance values.
a) 0.001 mm; b) 0.3 mm; c) 0.4 mm; d) 0.7 mm.

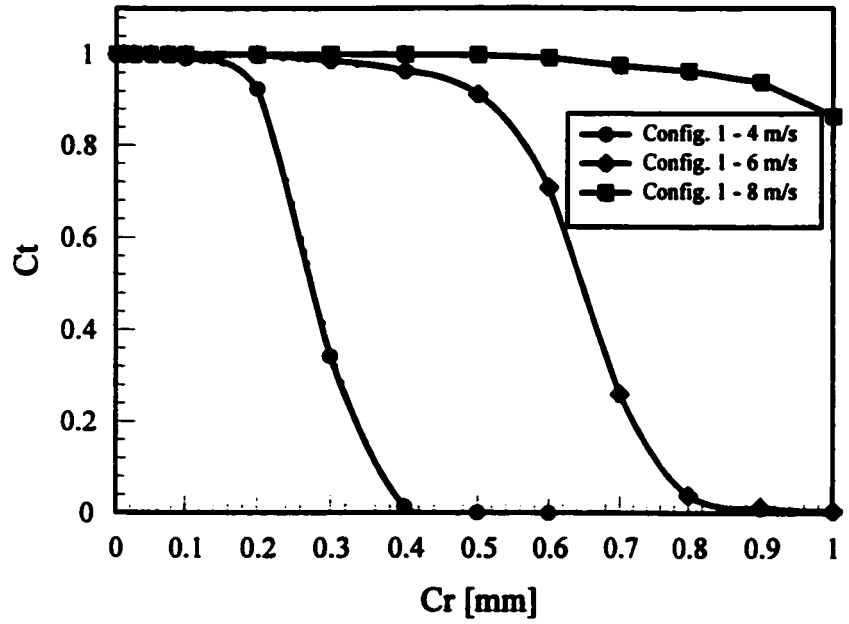

Figure 4.4 Effect of the clearance on the contact ratio for various flow velocities (configuration 1)

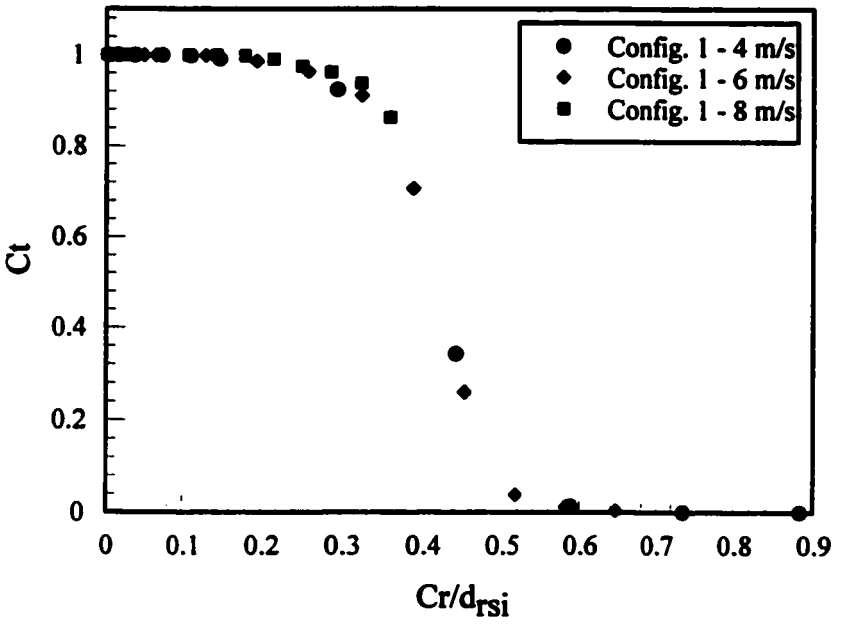

Figure 4.5 Effect of the dimensionless clearance on the contact ratio for various flow velocities (configuration 1)

approximately constant for a range of clearances (*Cr*). For a higher flow velocity, this range of clearances is larger. This is because the tube is kept in continuous contact with the support by the steady drag component which is larger for a higher flow velocity. Increasing the clearance beyond this range results in a sharp decrease in the contact ratio. It then levels off asymptotically to zero. This behaviour is observed for all flow velocities under investigation. The mode switch takes place in the clearance range where a sharp drop in the contact ratio occurs.

It is also observed that tubes with a similar excitation-to-clearance ratio have a similar vibration pattern. This is consistent with the findings of Yetisir and Weaver (1986), who concluded that doubling the clearance produces results similar to that of halving the excitation level. Accordingly, one can conclude that the dynamic patterns of tubes for similar overlap-to-excitation ratios are the same. Low excitation leads to a low tube vibration amplitude and the tube can vibrate within the support space without contacting the support provided that the clearance is significantly large. Now, if a higher excitation is applied to a tube with the same clearance, the tube would contact the support. The higher the excitation, the higher the tube's deflection, leading to a higher contact ratio. The clearance limits the tube's deflection due to a specific excitation level. It follows that the response of the free tube could be a suitable parameter to normalize the clearance.

To illustrate this idea, the contact ratio was plotted as a function of the dimensionless clearance (Figure 4.5). The dimensionless clearance was obtained by dividing the radial clearance (*Cr*) by the RMS support-inactive resultant response (d_{rsi}), ie., the linear response of a tube without an end support. Using this dimensionless parameter, (Cr/d_{rsi}) leads to a

significant data collapse of the contact ratio for various flow velocities. Moreover, it is found that the mode switch observed in the response spectra occurs in the same dimensionless clearance range ($0.4 < d_{rsi} < 0.5$)for all flow velocities.

4. 2. 2. 3 IMPACT FORCES

The RMS impact force (F_{imp}) depends on both the amplitude of the impact peaks and the contact duration; the higher the contact duration, the higher the impact force. Increasing the radial clearance decreases the contact ratio, which in turn decreases the RMS impact force. In addition, inducing higher energy due to a higher flow velocity results in a higher impact force. This is illustrated in Figure 4.6 which depicts the RMS impact force values versus the clearance for various flow velocities. The RMS impact force decreases linearly as the support clearance increases, then levels off asymptotically to zero. For any clearance size, increasing the flow velocity increases the RMS impact force. Since the resulting impact force must be related to the level of excitation, it is logical to use the RMS input force to normalize the resulting RMS impact force. The dimensionless RMS impact force is presented as:

$$F = \frac{F_{imp}}{P_{tur} L} \tag{4.1}$$

where F, P_{tur} and L are the dimensionless RMS impact force, the RMS distributed turbulence force per unit length, and the tube length respectively. The dimensionless clearance used herein is the same as that used in Section (4.2.2.1). Using these dimensionless parameters, the RMS impact force collapses over a single curve for the same support configuration, as

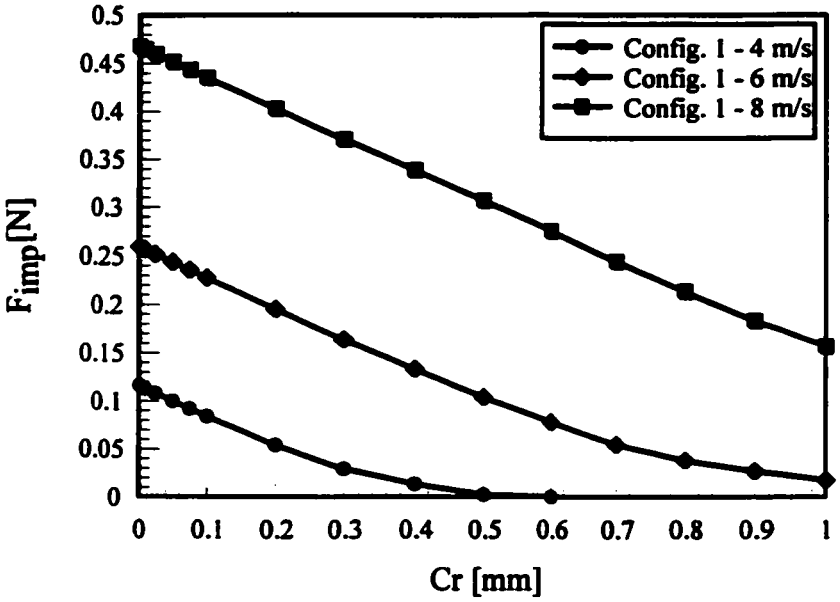

Figure 4.6 Effect of the clearance on the RMS impact force for various flow velocities (configuration 1)

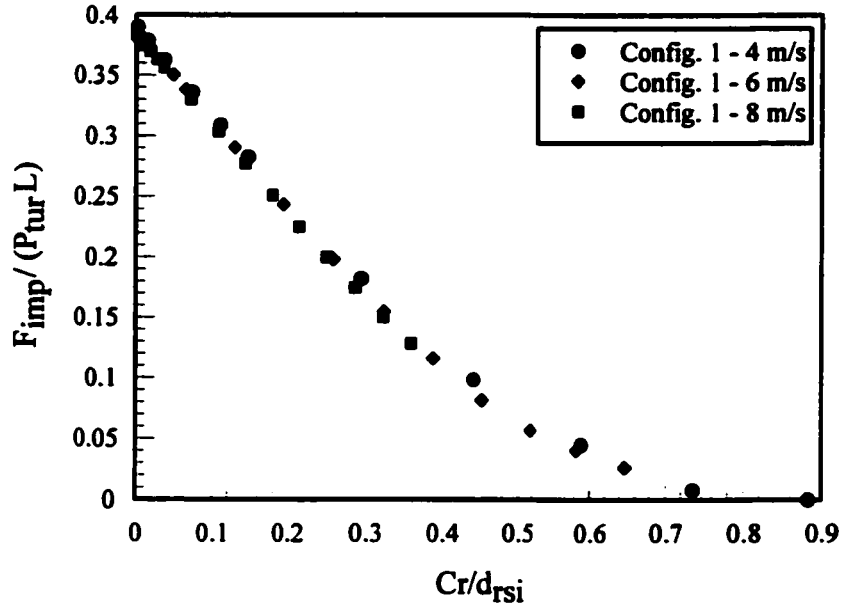

Figure 4.7 Effect of the dimensionless clearance on the dimensionless RMS impact force for various flow velocities (configuration 1)

shown in Figure 4.7. At a near-zero clearance, the dimensionless impact force is 0.39. With a larger dimensionless clearance, it decreases linearly and becomes asymptotic to zero as contact with the support ceases.

4. 2. 2. 4 TUBE DISPLACEMENT

In Figure 4.8, the mid-span tube response in the lift direction (d_y) is plotted against the radial clearance (Cr) for various flow velocities. The lift response shows a similar trend for all flow velocities. At a very small radial clearance, the tube maintains continuous contact with the support. The lift response is approximately equal to that of a fixed-hinged configuration. As the radial clearance increases, intermittent contact takes place and higher modes are excited. This leads to a gradual decrease in the RMS tube response. This gradual decrease in the tube response continues up to a certain clearance value. At this point, the mode switch occurs and the support becomes inactive. The tube response is then dominated by low frequency modes, and the RMS tube response is almost proportional to the radial clearance. At larger support clearances, the RMS response, as expected, approaches the support-inactive RMS tube response. The point of minimum RMS response, however, shifts to a larger clearance as the flow velocity increases. For a given clearance ($Cr < 0.3$ *mm*), increasing the flow velocity increases the response level. The RMS lift response and the support clearance are normalized by the RMS lift support-inactive response and the resultant support-inactive response respectively. Using these dimensionless parameters, data for various flow velocities are represented by a single curve (Figure 4.9). The dimensionless lift response for a near-zero clearance is approximately 0.2. This is the ratio of the constrained

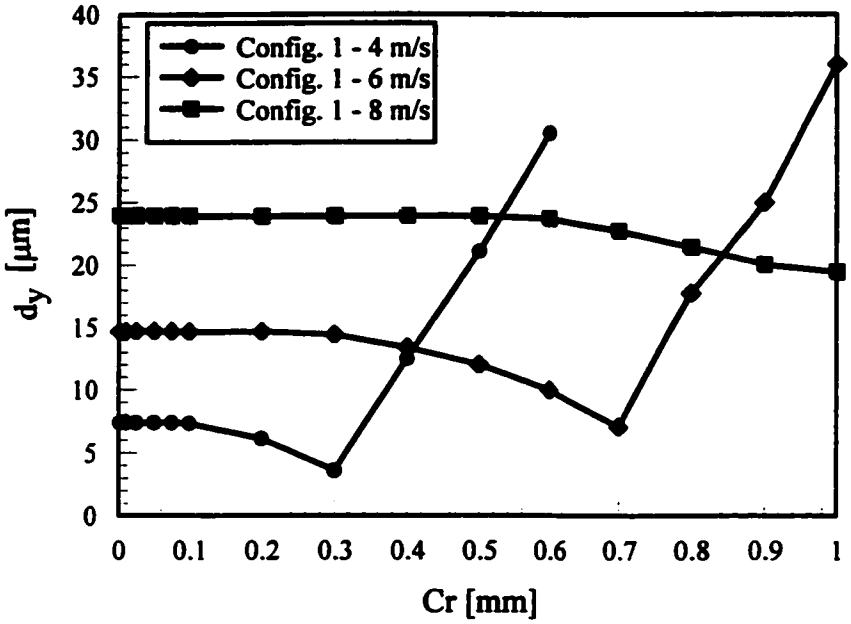

Figure 4.8 Effect of the clearance on the RMS lift displacement for various flow velocities (configuration 1)

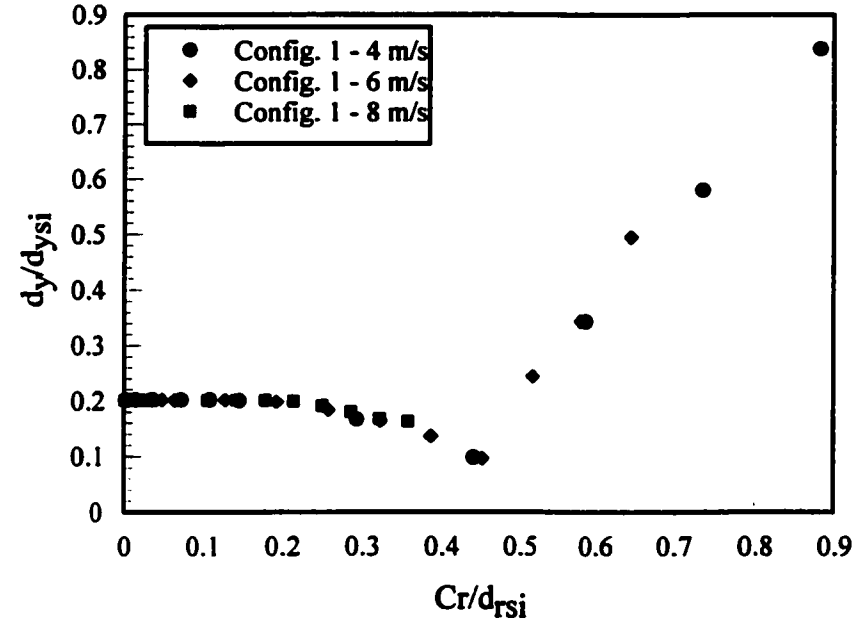

Figure 4.9 Effect of the dimensionless clearance on the dimensionless RMS lift displacement for various flow velocities (configuration 1)

tube response (support-active) to the unconstrained tube response (support-inactive). At dimensionless clearances larger than 1.0, the dimensionless lift displacement approaches unity. The point of minimum dimensionless displacement for all flow velocities is at a dimensionless clearance of 0.45.

Figure 4.10 shows the RMS mid-span tube response ($d_{\_}$) in the drag direction as a function of the support clearance for various flow velocities. The effect of drag forces is evident where the tube drag response increases linearly as the clearance increases. This behaviour is maintained up to a certain clearance after which the response approaches the RMS support-inactive tube response. As both axes were replaced by dimensionless parameters, a single curve can be obtained, as shown in Figure 4.11. Again, the mode switch can be identified by the change of the slope at a dimensionless clearance of 0.45.

4. 2. 2. 5 WORK RATE

Tube fretting wear is usually estimated by correlating the experimental wear rate with the work rate. Work rate (W_N) is calculated by averaging the product of the impact forces and the tube sliding displacement:

$$W_N = \frac{1}{T}\int_0^T F_N ds \qquad (4.2)$$

where T, F_N, and ds are the averaging time, normal impact force, and the sliding distance respectively. Figure 4.12 shows the predicted work rate as a function of the clearance. The

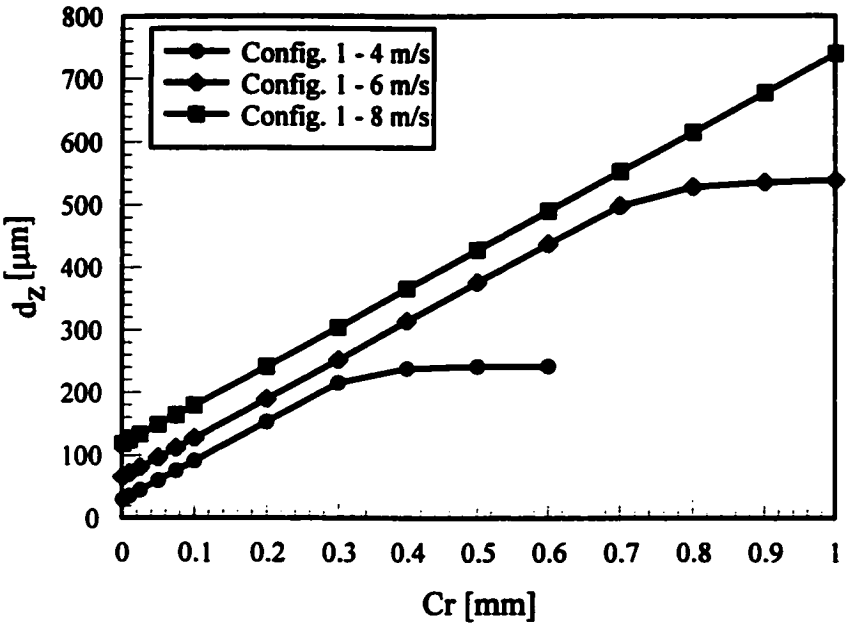

Figure 4.10 Effect of the clearance on the RMS drag displacement for various flow velocities (configuration 1)

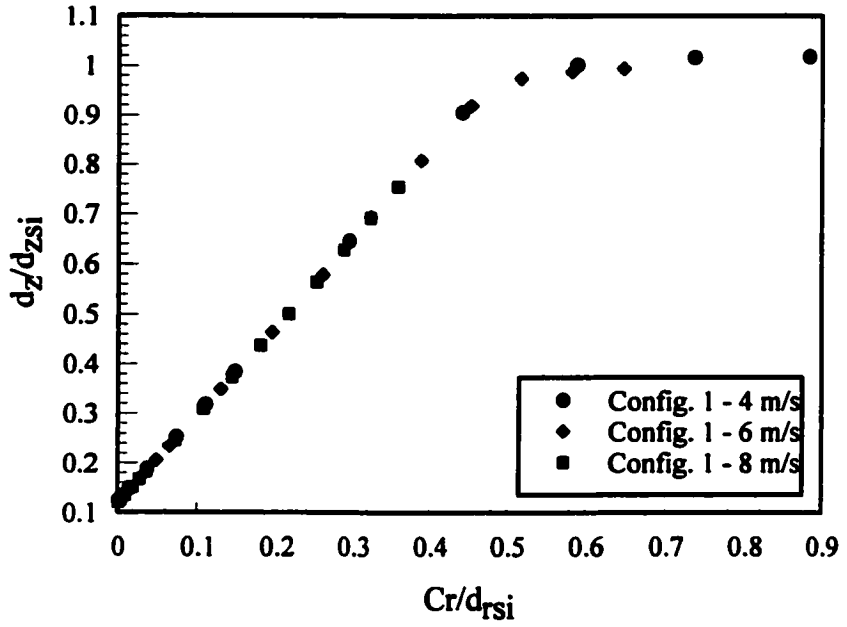

Figure 4.11 Effect of the dimensionless clearance on the RMS dimensionless drag displacement for various flow velocities (configuration 1)

general behaviour of the work rate was the same for all flow velocities under consideration. The normal work rate increases gradually as the clearance increases. The increase in the work rate continues to a certain clearance where less contact is being maintained. The mode switch then takes place. A further increase in the clearance causes the work rate to drop dramatically. The values of the work rate were normalized by the input power due to turbulence. The total power absorbed by a tube of length , L, and mass per unit length, m, was expressed by Yetisir et al. (1997):

$$W_{tur} = \sum_{i=1}^{N} \frac{S_{FF}(f_i) J_i^2 L}{2m} \tag{4. 3}$$

where $S_{FF}(f_i)$ and J^2_i are the PSD of the local force per unit length at the i^{th} mode, and the joint acceptance respectively. The joint acceptance of a mode is a measure of the degree to which the spatial distribution of the turbulence forces is compatible with the tube's mode shape. The clearance was also normalized by the RMS support-inactive tube response. These dimensionless parameters are presented in Figure 4.13. A good collapse of the results for different flow velocities was obtained. It should be noted that only the turbulence excitation is considered. Therefore, as the mode switch occurs for sufficiently high flow velocities, the work rate may continue to increase as the clearance increases. This is due to the evolution of fluidelastic instability in a lower mode which was previously supported. This behaviour is not included in this thesis.

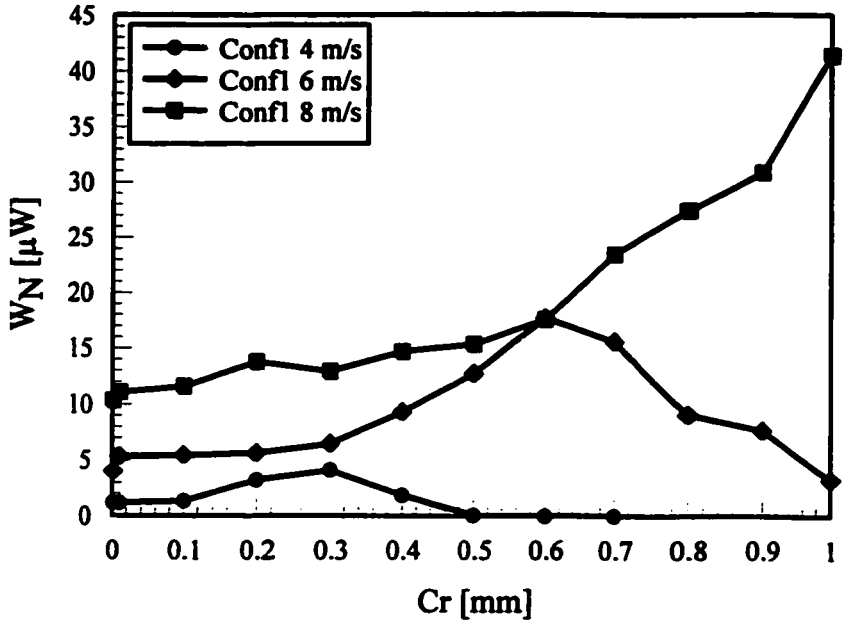

Figure 4.12 Effect of the clearance on the normal work rate for various flow velocities (configuration 1)

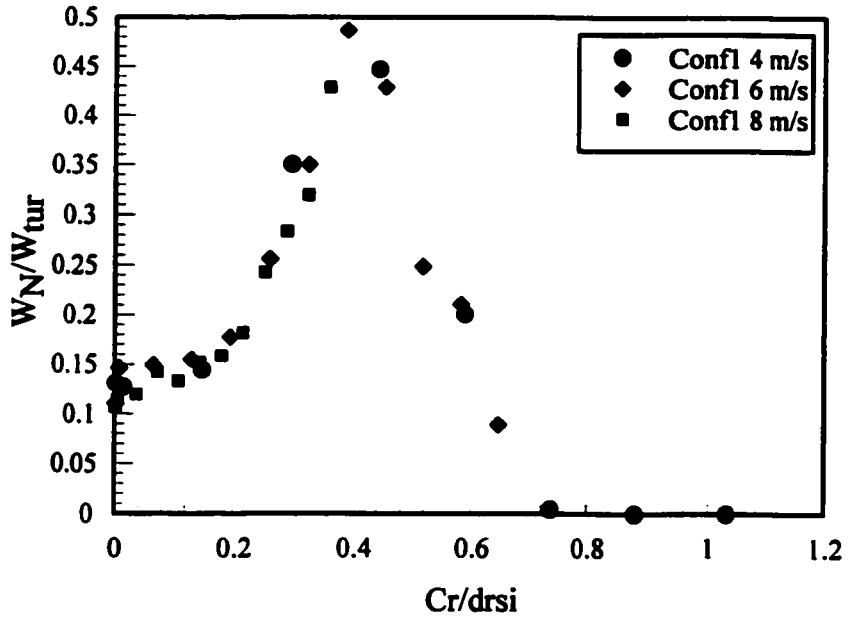

Figure 4.13 Effect of the dimensionless clearance on the normal work rate for various flow velocities (configuration 1)

4. 3 SCALING FOR DIFFERENT CONFIGURATIONS

To investigate the applicability of scaling the dimensionless results reported herein, additional configurations with different tube lengths and diameters were analysed. These configurations were designated as configuration 2 and configuration 3 respectively. Configuration 2 utilizes a 305 mm long tube with a diameter of 6.35 mm, while a 617 mm long tube with a 15.88 mm diameter is used in configuration 3. The lowest natural frequencies of these configurations are 38.6 and 28 Hz respectively. Simulations for configurations 2 and 3 were carried out assuming a flow velocity of 6 m/s. At this flow velocity, the lift response of configuration 1 (with a radial clearance of 0.025 mm) is 16 times that of configuration 3 with a radial clearance of 0.01 mm.

The response spectra in both cases are similar in terms of the participating modes. This suggests the dynamic similarity of both configurations under these conditions. It turns out that projecting these values on the dimensionless coordinates yields identical dimensionless responses and dimensionless clearances. This shows that the similarity principle based on the value of the dimensionless clearance can also be applied to single-span tubes with different dimensions. Results pertaining to the whole range of clearances obtained from configuration 2 and configuration 3 are plotted using the proposed dimensionless parameters, and compared with those of configuration 1.

4. 4 MULTISPAN TUBE CASE

4. 4. 1 MODEL DESCRIPTION

Figure 4.18 shows the finite element model for a tube supported by three loose supports each of which is the same as shown in Figure 4.1. The overall tube length is 3.4 m

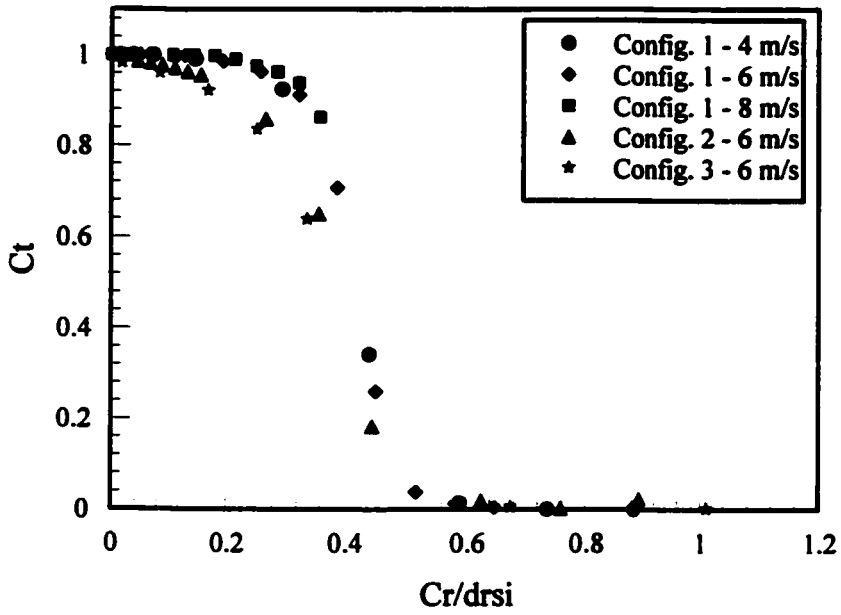

Figure 4.14 The contact ratio for all configurations

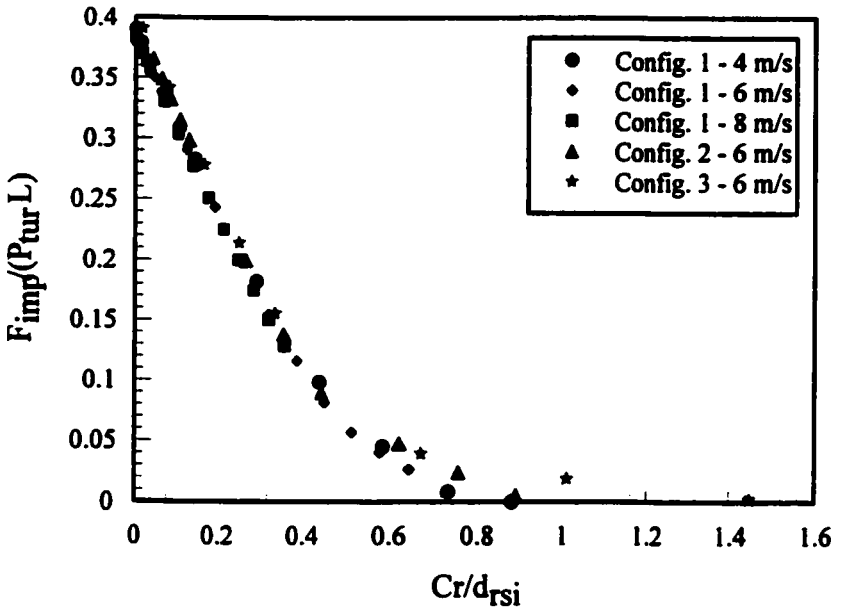

Figure 4.15 The dimensionless RMS impact force for all configurations

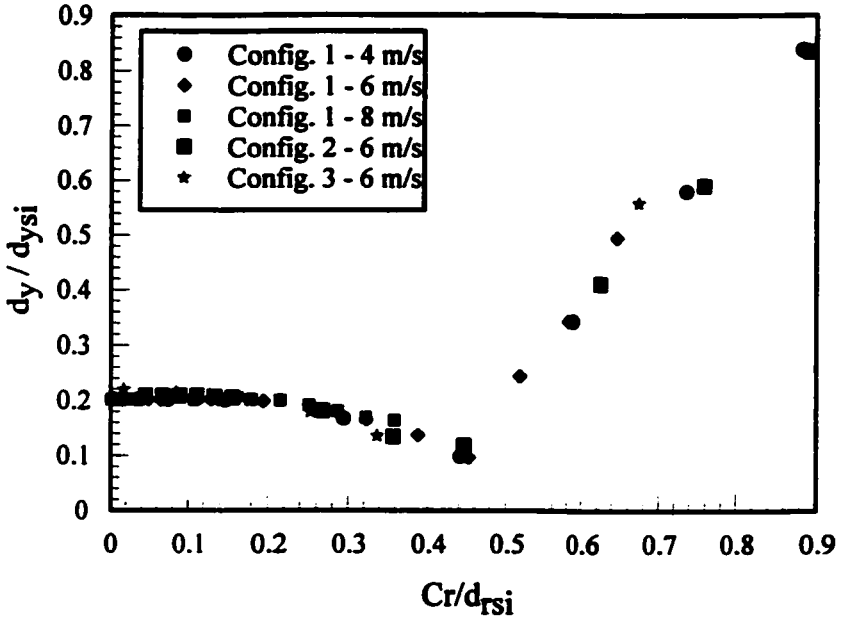

Figure 4.16 The dimensionless RMS lift response for all configurations.

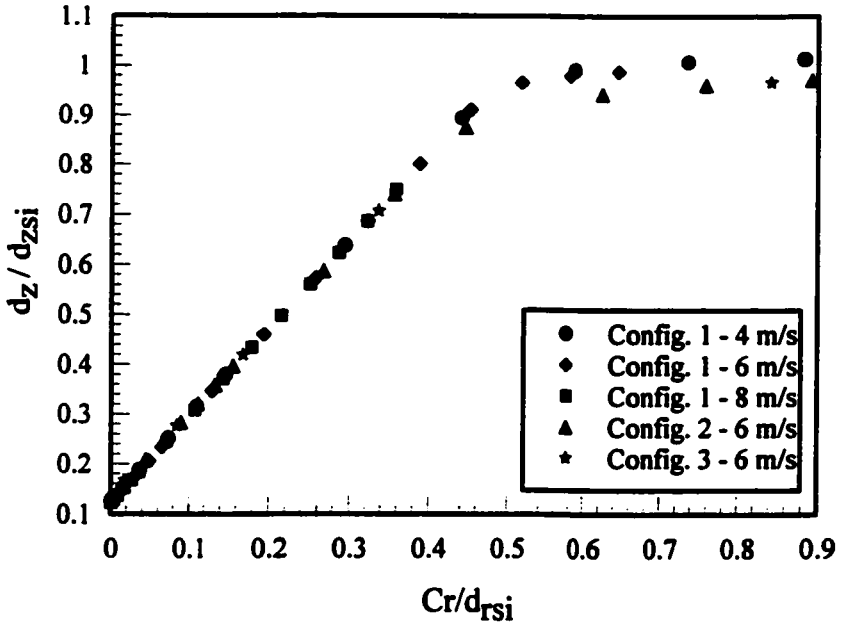

Figure 4.17 The dimensionless RMS drag response for all configurations.

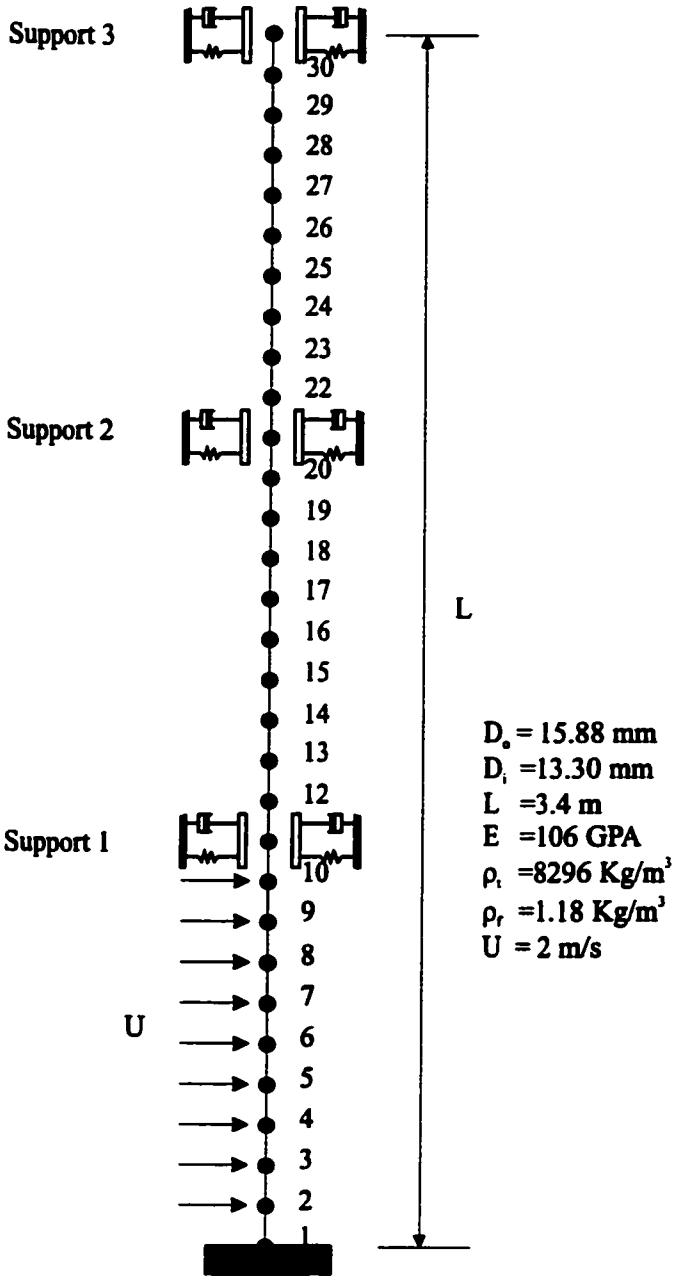

Figure 4.18 A multispan tube model.

with a 15.88 mm outer diameter and a 13.3 mm inner diameter. The three loose supports are placed such that equal spans are maintained and the clearance is assumed to be the same at all supports. Random forces representing turbulent air flow are assumed. The turbulence excitation is modelled as a distributed load along the lower span.

4. 4. 2 RESULTS AND DISCUSSION

4. 4. 2. 1 CONTACT RATIO

Figure 4.19 depicts the contact ratio between the tube and the three supports for various support clearances. The clearance is normalized by the constrained tube response at the support 3. The contact ratio between the tube and the first support is similar to that of a single-span tube in that the contact ratio initially decreases at a small rate and then decreases sharply. At a larger clearance ($0.05 < Cr/d_{ni} < 0.09$), the contact ratio decreases asymptotically to zero. The contact ratio between the tube and the second support shows an interesting behaviour. At zero clearance, the tube maintains contact with all supports. For a non-zero clearance, since the excitation forces are distributed along the first span only, the deflection in the other spans is not large enough to maintain continuous contact between the tube and both the second and the third support. Thus, as the clearance increases slightly, the contact ratio at the second and the third support decreases dramatically. A further increase in the dimensionless clearance permits intermittent contacts which excite higher modes. Moreover, the first support becomes less effective in resisting the tube's motion. A larger tube deflection is therefore transferred to the second span. Consequently, the deflection of the tube in the neighbourhood of the second support significantly increases with the increase

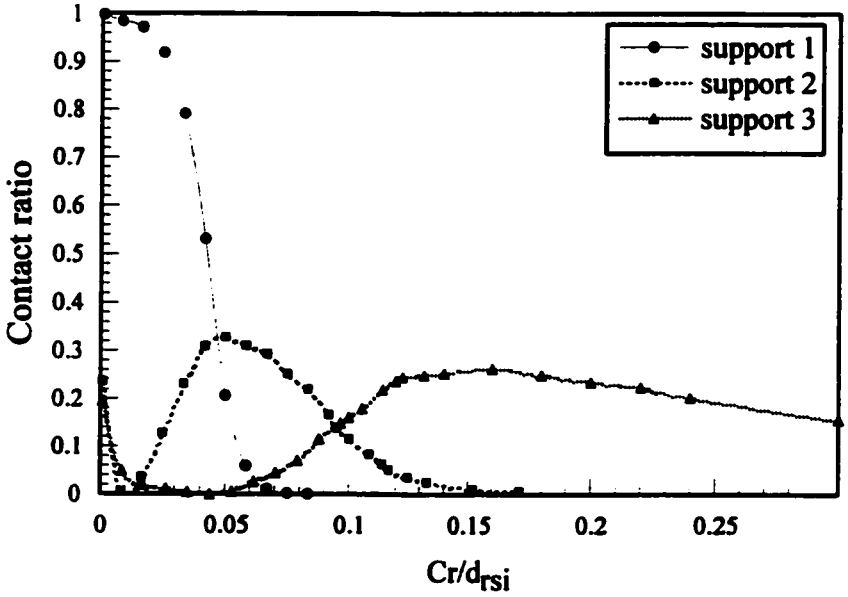

Figure 4.19 Effect of the clearance on the contact ratio for all supports

in the support clearance. This leads to an increase in the contact ratio at the second support. Thus, there is a support duty exchange between first and second support. This process of duty exchange continues until the tube loses contact with the first support. The contact ratio then between the tube and the second support continues to increase until a dimensionless clearance of 0.06. Beyond this clearance, the contact ratio decreases gradually as the dimensionless clearance increases. Now, the support duty exchange between the second and third support takes place. The tube loses contact with the second support at a dimensionless clearance of about 0.2. The contact ratio at the third support reaches its maximum at a dimensionless clearance of 0.14, after which it deceases gradually and levels off asymptotically to zero.

4. 4. 2. 2 RMS IMPACT FORCE

The RMS impact forces for the three supports are shown in Figure 4.20. The behaviour of the RMS impact force is similar to that of the contact ratio. Impact forces at the first support are high at small clearances and decrease nearly linearly as the clearance increases. As less contact is maintained by the first support, a higher impact force arises at the second support and reaches its maximum at a dimensionless clearance of 0.05. A further increase in the support clearance results in a decrease in the impact force. At this point, the RMS impact force at the third support increases gradually to its maximum at a dimensionless clearance of about 0.14 then decreases.

In summary, the intensity of the impact forces at each of these supports depends on the clearance at these supports. It is also concluded that a process of load redistribution

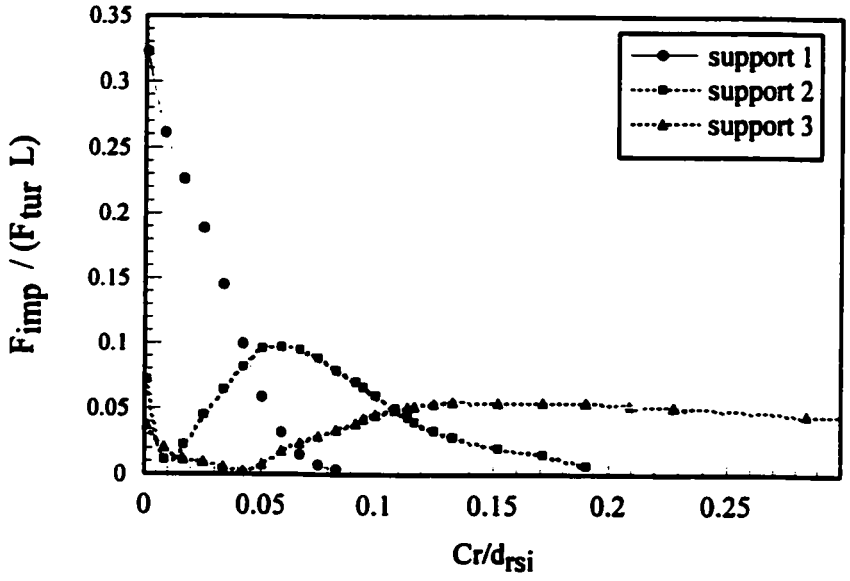

Figure 4.20 Effect of the clearance on the RMS impact force for all supports

occurs among the three supports. This load redistribution is controlled by the effectiveness of the neighbouring supports.

4. 4. 2. 3 TUBE DISPLACEMENT

The dimensionless tube response at x/L= 0.16 (approximately the middle of the lowest span) in the lift direction is plotted against the dimensionless clearance in Figure 4.21. Generally, an increase in the support clearance results in an increase in the dimensionless tube response. However, there are several undulations in the resulting curve, each of which is associated with one of the mode switches which will be discussed in the next section.

Figure 4.22 shows the dimensionless tube response ($d_{\_}/d_{\_si}$) in the drag direction as a function of the support clearance. Similar to the single-span tube, the tube drag response increases monotonically as the clearance increases up to the point that no contact occurs. The drag response curve can be divided into approximately four different regions. Within each of these regions, the dimensionless drag response increases approximately linearly as the dimensionless clearance increases. The transition between these regions corresponds to one of the major mode switch events. In the fourth region, the first and the second supports are inactive, while the tube maintains little contact with the third support.

4. 4. 2. 4 RESPONSE SPECTRA

The response spectra of the tube lift response for various dimensionless clearances is illustrated in Figure 4.23. The response spectra of a multispan tube are very complex because they consist of peaks belonging to combinations of different modes. The

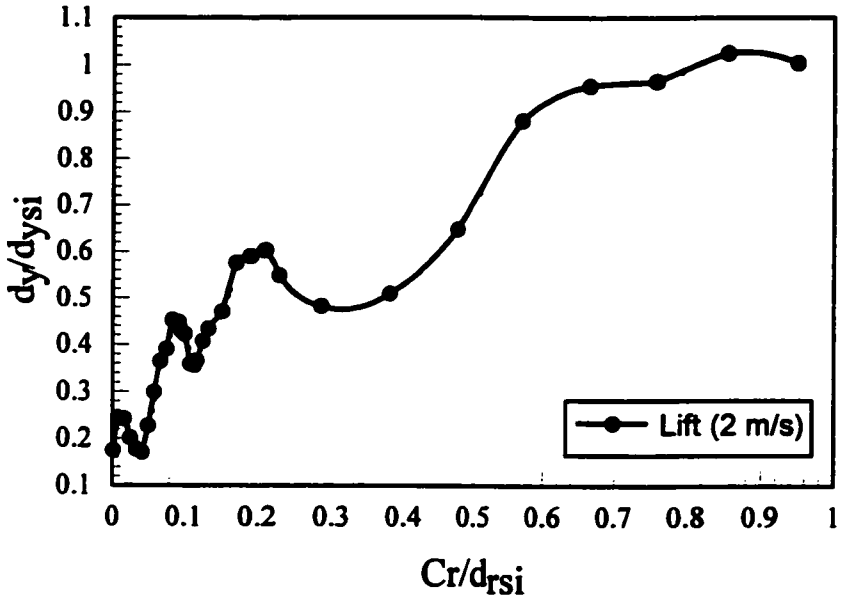

Figure 4.21 Effect of the clearance on the RMS lift response for all supports

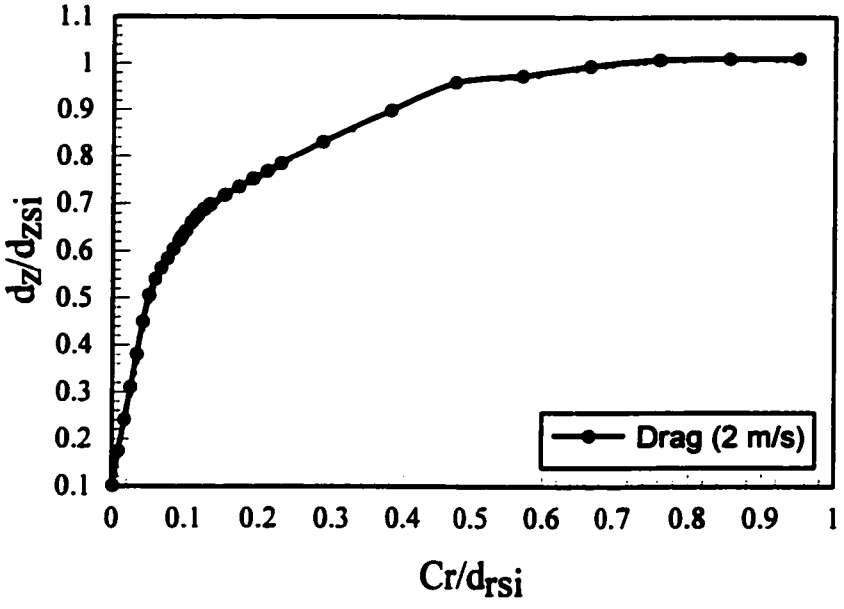

Figure 4.22 Effect of the clearance on the RMS drag response for all supports

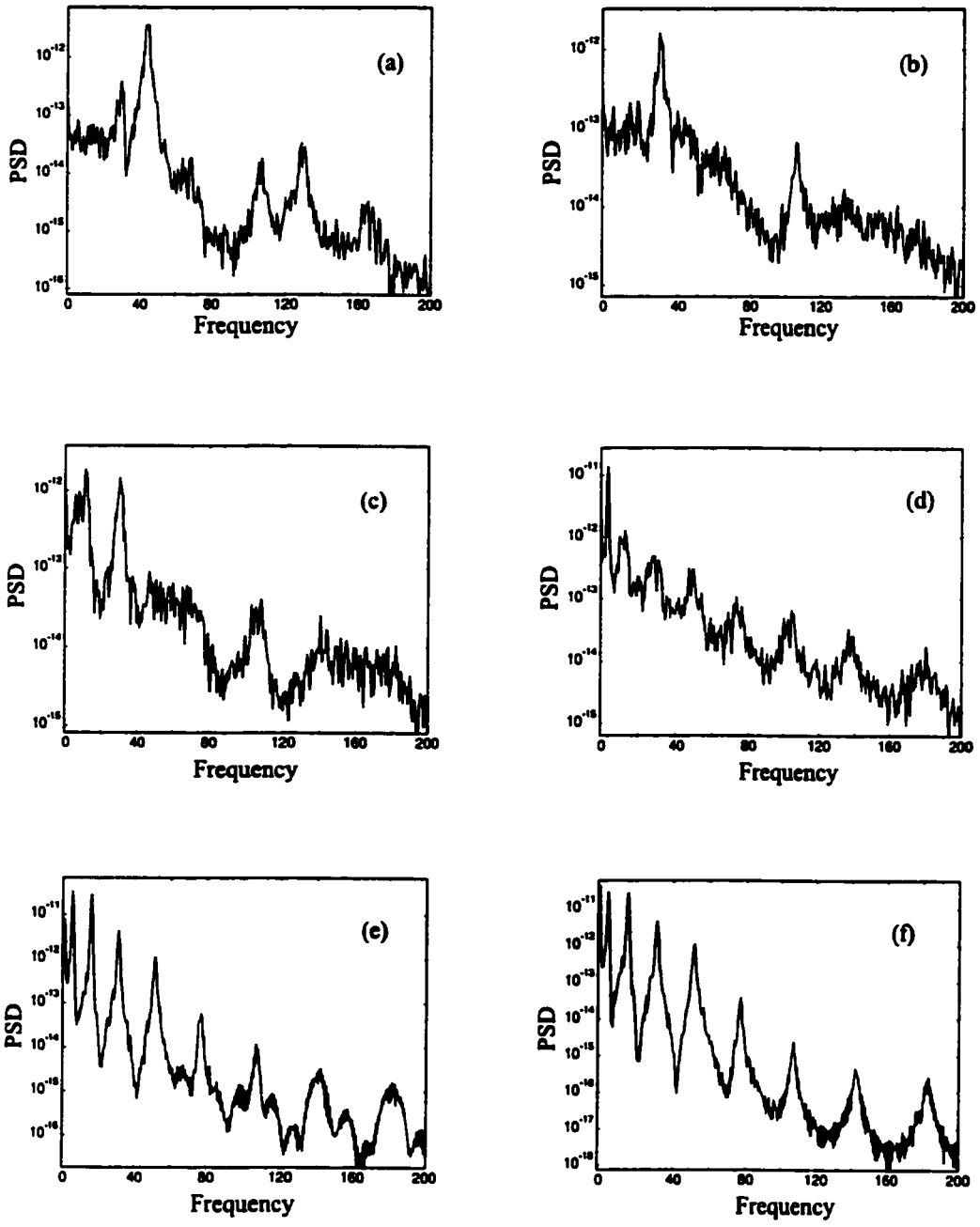

Figure 4.23 Response spectra for various dimensionless support clearances. a) 0.02; b) 0.05; c) 0.07; d) 0.18; e) 0.8; f) 0.9.

appearance of certain modes depends on the effectiveness of each of the three supports. At low dimensionless clearances ($0<Cr/drsi<0.05$), the tube maintains a high contact ratio with the first support. This is manifested by the appearance of high frequency modes in the response spectra. The frequency of the fundamental mode is 30 Hz. However, the dominant mode is 44 Hz (Figure 4.23a). These frequencies correspond to the case in which the tube is effectively restrained at the first support, is partially supported at second and has little restraint at the third. Within this dimensionless clearance range, the amplitude of the fundamental frequency (30 Hz) increases as the dimensionless clearance increases. Finally it becomes the dominant mode at a dimensionless clearance of 0.05 (Figure 4.23b). This corresponds to the configuration where the tube is fully restrained at the second support, is partially restrained at the first support, and has very little restraint at the third support. Moreover, at this dimensionless clearance the peak of the contact ratio between the tube and the second support occurs (Figure 4.19). As the dimensionless clearance increases, the tube faces less restraint at the second support and an increasing restraint at the third support. This is demonstrated by the appearance of a peak at a frequency of 12.0 Hz. With an increase in the dimensionless clearance, this peak (12 Hz) increases until it becomes dominant at a dimensionless clearance of 0.07 (Figure 4.23c). At this dimensionless clearance, the tube completely loses contact with the first support. As the dimensionless clearance increases further, the fundamental frequency is gradually reduced until it reaches 4.0 Hz at 0.18 (Figure 4.23d). At this dimensionless clearance, the tube has its maximum contact ratio with the third support while it faces less restraint at the second support. Response spectra contain distinct peaks at frequencies of 31, 51, 76, 107, 141, and 179 Hz. These frequencies are

approximately the natural frequencies of the unconstrained system. The first two peaks, however, are at frequencies around 3.7 and 12 Hz. The frequency of the second peak (12.0 Hz) increases progressively until it reaches the frequency of the third unrestrained mode (16 Hz). Concurrently, the frequency of the fundamental mode decreases continuously (Figure 4.23e). The mode switch is totally achieved by the appearance of the second unconstrained mode at a dimensionless clearance of 0.5 (Figure 4.23f). Tube's natural frequencies for a support active at one support are shown in Table 4.2.

To examine the applicability of the proposed dimensionless parameters, additional simulations were performed at a flow velocity of 4 m/s. Results obtained from the two flow velocities are compared. A sample of the dimensionless response of the tube due to these flow velocities are shown in Figure 4.24 and 4.25. An excellent collapse of the results is obtained.

Table 4.2 The predicted natural frequencies of the tube with only one support active

Mode 1	Support 1 active	Support 2 active	Support 3 active
1	1.7	3.4	3.9
2	10.9	11.7	12.8
3	30.3	30.4	26.7
4	44.3	43.9	45.7
5	66.2	66.1	69.8
6	105.8	105.8	98.9

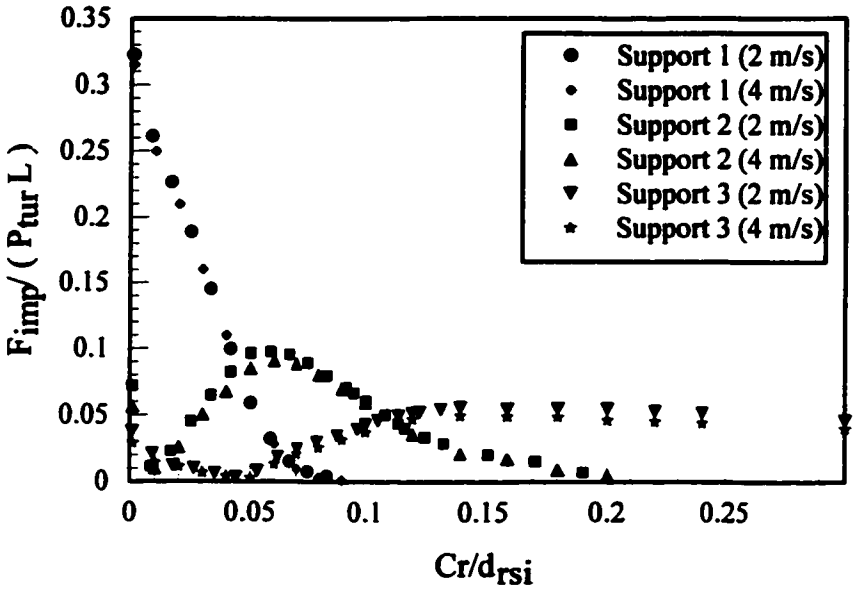

Figure 4.24 Effect of the clearance on the contact ratio for all supports due to different flow velocities

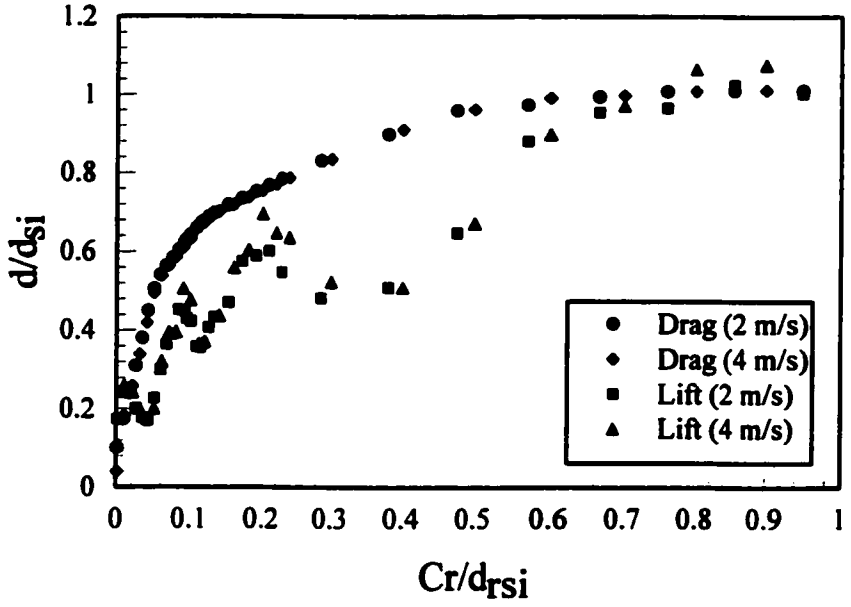

Figure 4.25 Effect of the clearance on the RMS drag and lift response for all supports due to different flow velocities

4.5 EFFECT OF LATTICE-BAR GEOMETRY

4.5.1 TUBE/SUPPORT MODEL

Two types of lattice-bar supports will be investigated in this section: square flat-bar (SFB) and rhomboid flat-bar (RFB) supports, as shown in Figure 4.26. The SFB support (Figure 4.26a) consists of two pairs of flat bars (pairs A and B) perpendicular to each other. Due to the geometry of the SFB, the tube-to-support clearance in the drag and lift directions is equal to the nominal radial clearance regardless of the direction of the flow. The nominal radial clearance is the clearance between the tube and its supports in the direction normal to the support surface. In comparison, the RFB support (Figure 4.26b) consists of two pairs of flat bars which form a diamond-shaped support space. In the case of the RFB support, the ratio of the clearance in the drag and lift directions to the nominal clearance are 2 and 1.155 respectively for the flow direction shown in Figure 4.26b.

4.5.2 SIMULATION RESULTS

Both square flat-bar (SFB) and rhomboid flat-bar (RFB) supports are considered in this study. Since the use of dimensionless parameters collapses the results of different excitation levels (flow velocities) over a single curve, a single flow velocity of 6 m/s was considered. Configuration 3 from Section 4.3 was utilized in this analysis.

In order to determine the general features and differences between these types of supports, details of the tube/support interaction at each of the support pairs are studied. The two pairs in the RFB support are at equal angles (30°) to the flow direction. Therefore, the tube has an equal probability of contact with either pair regardless of differences in the force

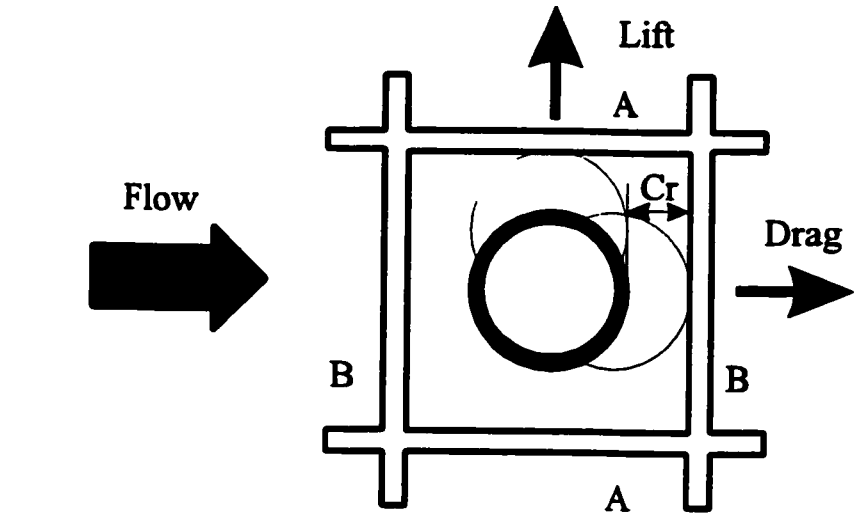

a)

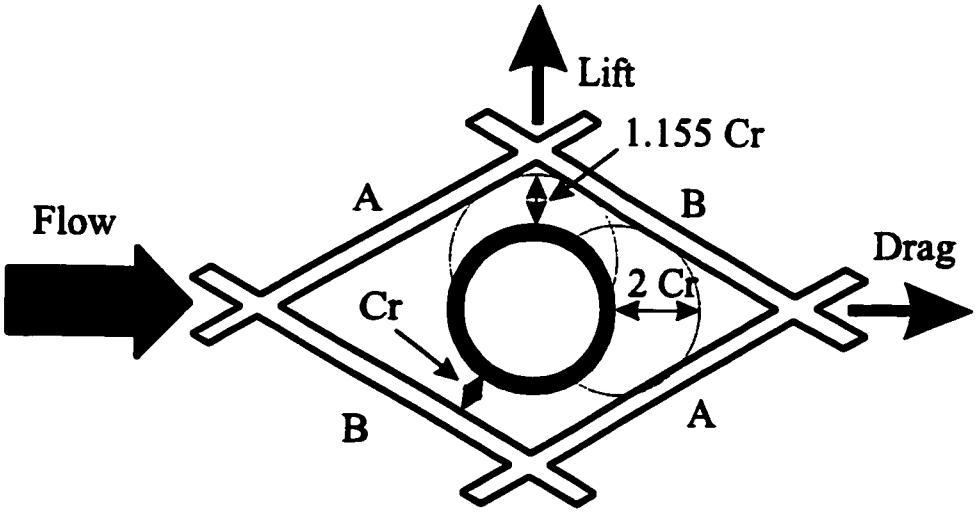

b)

Figure 4.26 Types of lattice-bar supports. a) SFB lattice-bar support b) RFB lattice-bar support

level applied in the lift and drag directions. In the case of the SFB support, each of these pairs is perpendicular to one of the excitation directions (drag or lift). Hence contact with either pair depends on the excitation level in the lift and the drag directions. Figure 4.27 depicts the contact ratio at both pairs for the two support configurations (SFB support and RFB support). The contact ratio for pairs A and B are identical in the case of the RFB support. The RFB support exhibits a higher contact ratio than the SFB support for pair A. The contact ratio at pair A of the SFB support drops dramatically to zero at a dimensionless clearance (Cr/d_{rsi}) of 0.1. This is where the tube loses contact with this pair because pair A is perpendicular to the lift direction of tube response. On the other hand, the contact ratio at both pairs deceases to zero at a dimensionless clearance (Cr/d_{rsi}) of 1.1 for the RFB support. The SFB support, however, exhibits a higher contact ratio at pair B. This is because the clearance in the drag direction for the SFB support is half that of the RFB support.

A similar behaviour is expected for the RMS impact force since it is dependent on the contact ratio. The RFB support exhibits an identical RMS impact force level for both pairs as shown in Figure 4.28. On the other hand, the SFB support exhibits a higher impact force level at pair B (drag direction) than at pair A (lift direction).

The RMS tube response in the lift direction is shown in Figure 4.29. The RFB support exhibits a characteristic behaviour. Up to a certain dimensionless clearance, the tube response decreases gradually. The support then becomes inactive which leads to the mode switch. This results in the evolution of low-frequency modes. A further increase in the clearance will yield an increase in the tube response. This will finally approach the response

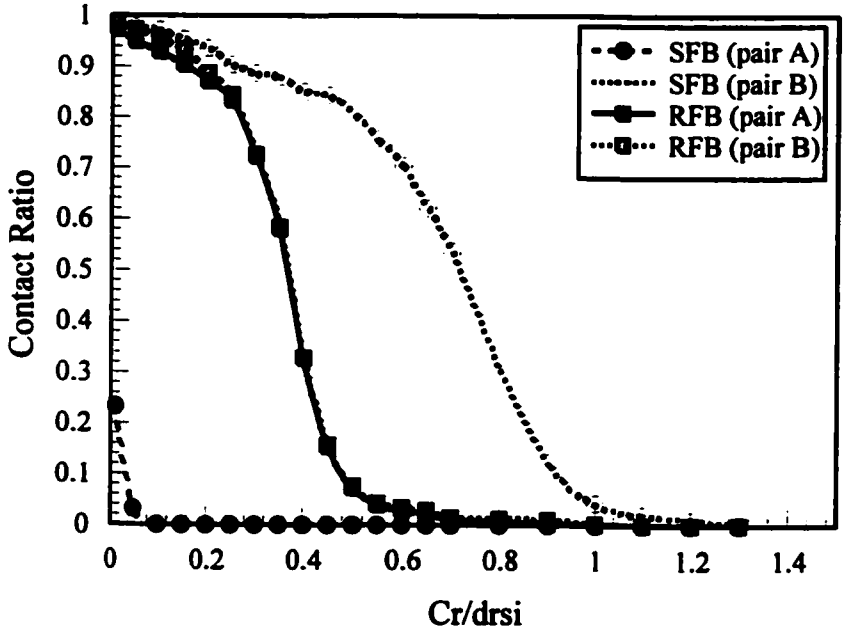

Figure 4.27 Effect of the dimensionless clearance on the contact ratio for the SFB and RFB supports

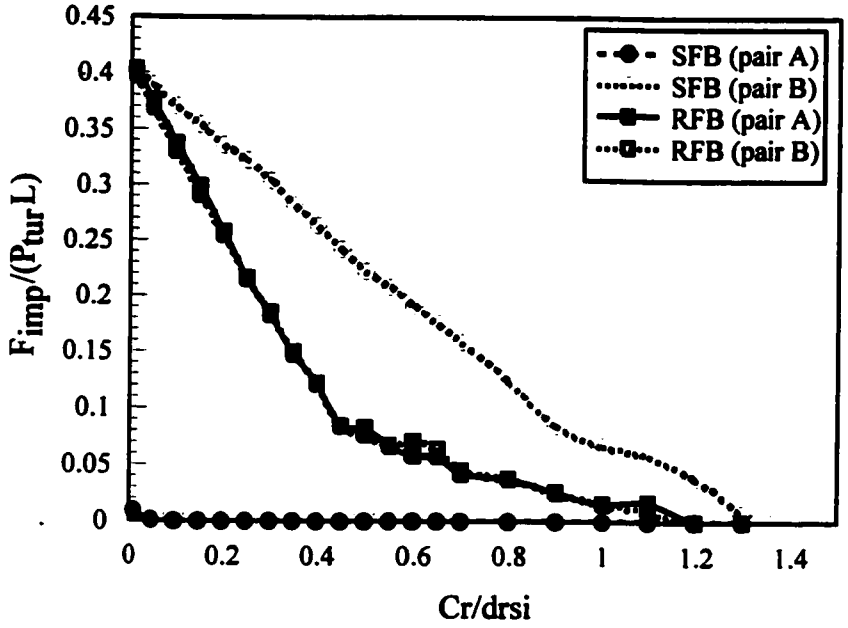

Figure 4.28 Effect of the dimensionless clearance on the RMS impact force for the SFB and RFB supports

level of the linear unconstrained system.

In the case of the SFB support, three different response regions can be identified. The first and the second regions cover dimensionless clearance values ranging from 0 to 0.1 and 0.1 to 0.6 respectively. The third region describes the tube response beyond 0.6. Initially, the tube lift response increases rapidly in the first region due to an early mode switch. In the second region, the tube response increases at a very low rate. In this clearance range, the tube's motion in the lift direction is resisted only by friction forces. This is because there is no contact between the tube and the support pair in the lift direction. The strong effect of these friction forces is driven by the high normal forces caused by the steady drag forces. In the third region, less contact is maintained, which leads to a lower friction resistance at the tube/support interface. This is manifested by the response increase at a higher rate beyond a dimensionless clearance of 0.6.

The tube's response is totally controlled by the clearance in the drag direction. Hence, the drag response is higher in the case of the RFB support. This is illustrated in Figure 4.30. As mentioned earlier, the ratio of the effective clearance to the nominal clearance for the SFB and RFB are 1 and 2, respectively. Therefore, the displacement in the drag (for the range of clearance/excitation values that provides support-active end condition) for the RFB support is twice that of the SFB support. In other words, the drag response curve of the SFB (Figure 4.30) is scaled horizontally by a factor of 2.

Predicted normal work rates for both support types are presented in Figure 4.31. The work rate at pair A is higher in the case of the RFB support. However, the work rate for the SFB support is higher than that of RFB support for the same level of excitation at pair B. These results are not surprising since the geometry of the SFB support should promote more

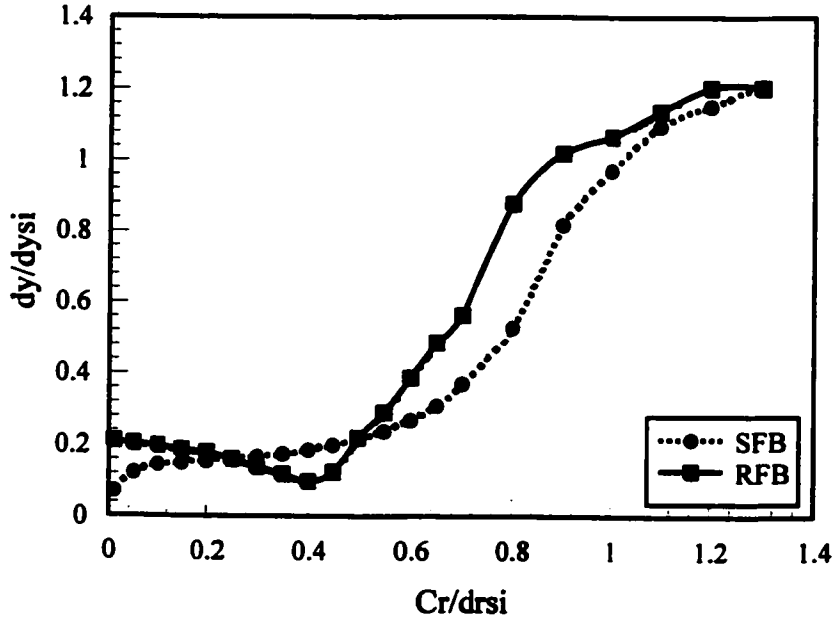

Figure 4.29 Effect of the dimensionless clearance on the dimensionless RMS lift response for the SFB and RFB supports

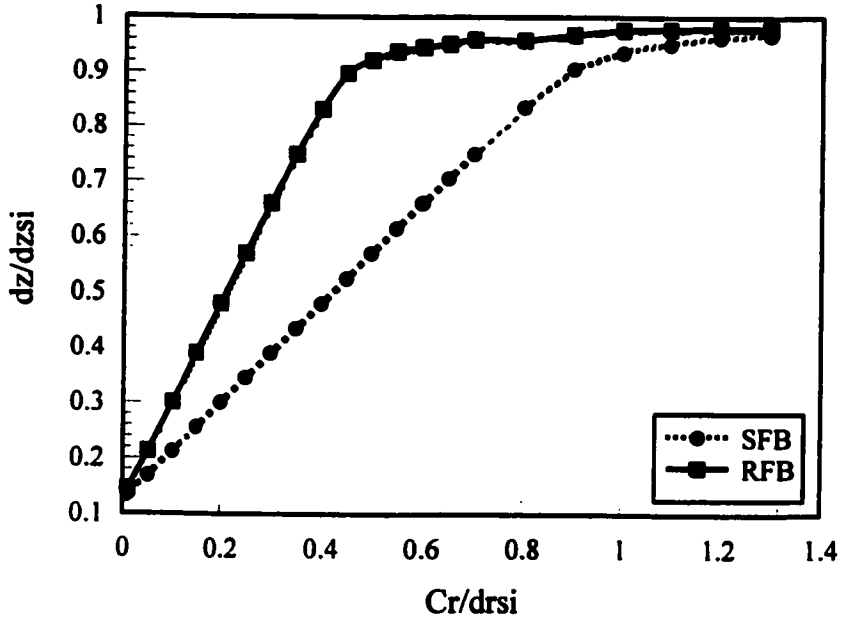

Figure 4.30 Effect of the dimensionless clearance on the dimensionless RMS drag response for the SFB and RFB supports

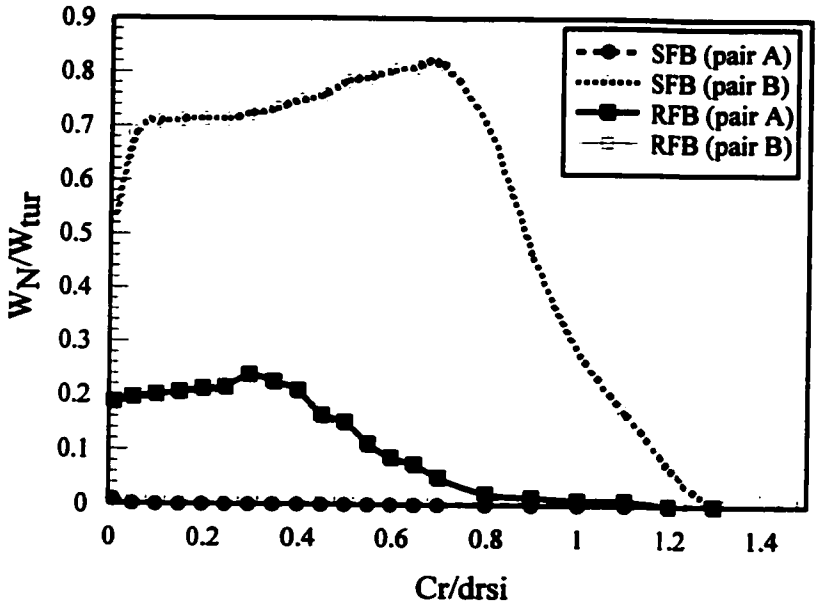

Figure 4.31 Effect of the dimensionless clearance on the dimensionless normal work rate/pair for the SFB and RFB supports

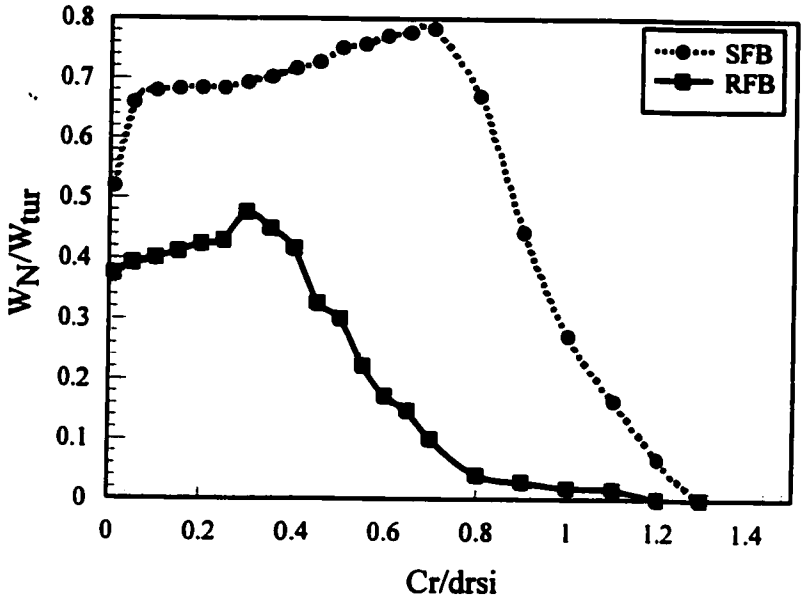

Figure 4.32 Effect of the dimensionless clearance on the dimensionless total normal work rate for the SFB and RFB supports

sliding motion and therefore, a higher work rate. Impact force always has a component in both the lift and the drag directions. This limits the sliding motion of the tube in an RFB support. However, friction is the only resistance to tube motion in the lift direction if no contact is maintained with pair A of the SFB. This has a great effect on the total work rate which is higher in the case of the SFB support (see Figure 4.32).

4. 6 EFFECT OF FLOW ORIENTATION

Tubes within the entrance region of heat exchangers or steam generators are usually subjected to a significant level of turbulence. The flow field is characterised by a variable mean velocity as well as a direction which is dependent on the location, as shown in Figure 4.33. To study the effect of the flow field, numerical simulations are carried out for a single-span tube (Configuration 3 of Section 4.3) subjected to flow velocity of 6 m/s. Seven flow angles ranging from 0° to 90° are investigated with an average of 21 radial clearance values per flow angle. These simulations were carried out considering a tube supported by a loose RFB support, as shown in Figure 4.34a. A typical tube response at the support location is shown in Figure 4.34b. The tube motion reflects the influence of the steady drag forces. This is manifested by the confinement of the trajectory of the tube's centre to an area where the tube is pushed against the support plate. It can also be seen that the tube slides along the flat bars.

The contact between the tube and the specific pair is dependent on the flow direction. When the flow angle is zero, the flow direction is at an angle of 30° with either pair. Therefore, the contact ratio for both pairs is the same. As the flow direction changes, the tube maintains an unequal contact ratio with the two pairs. The contact ratio is expected to

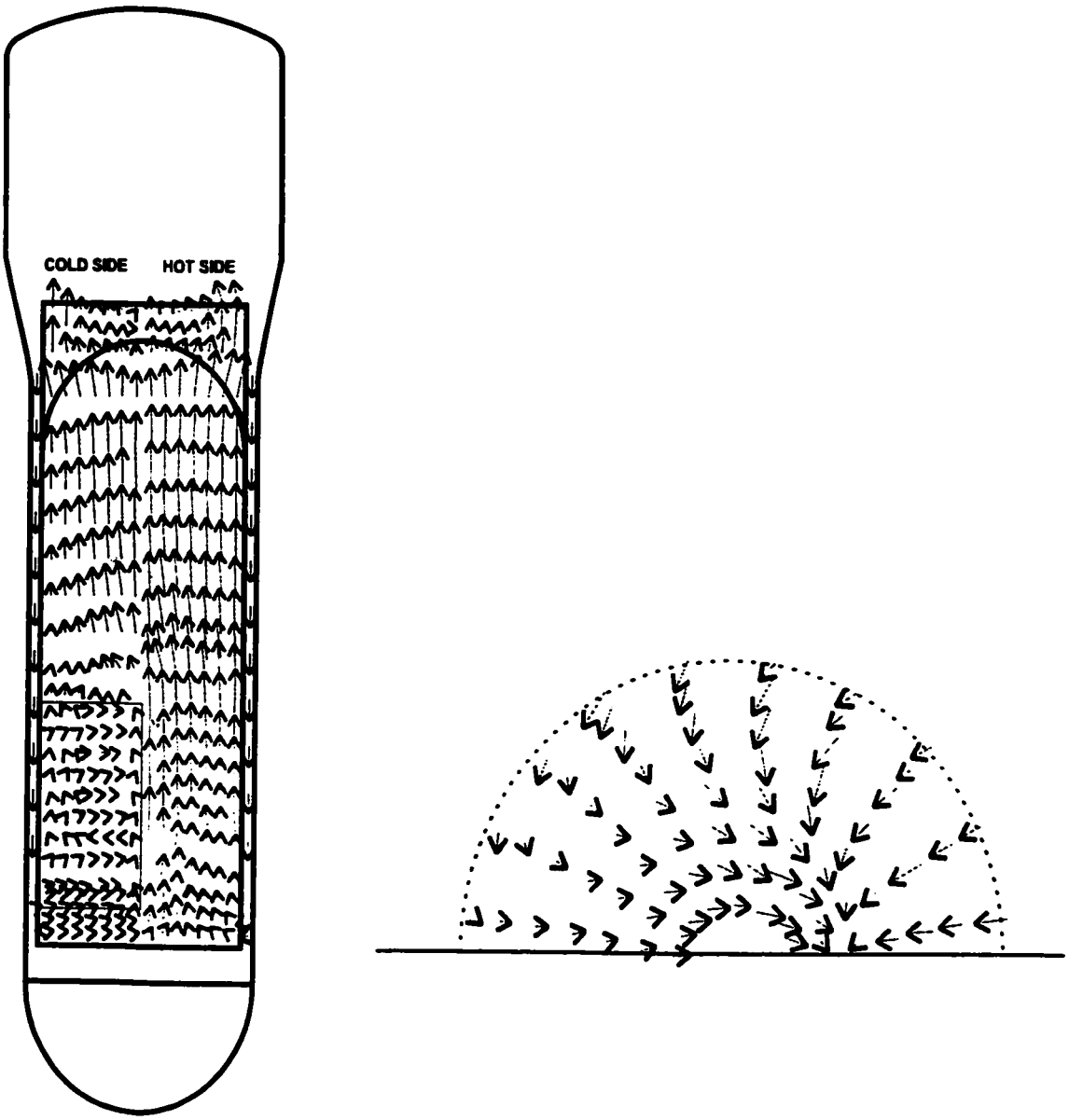

Figure 4.33 Flow distribution in the entrance region (Pettigrew *et al.*, 1991)

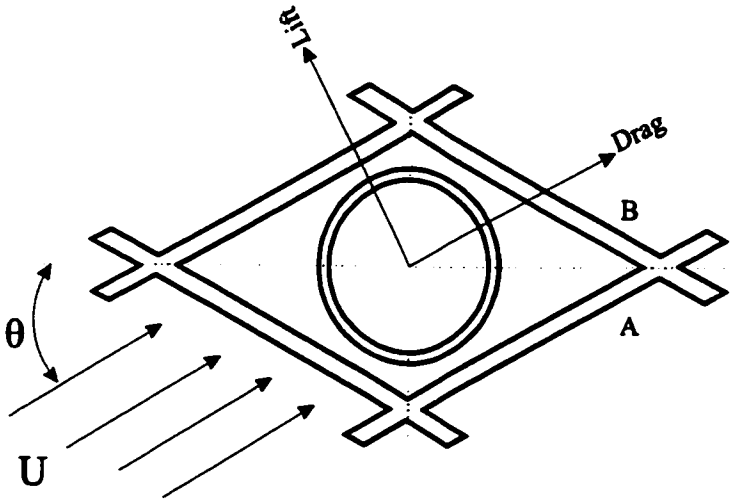

a) Flow orientation

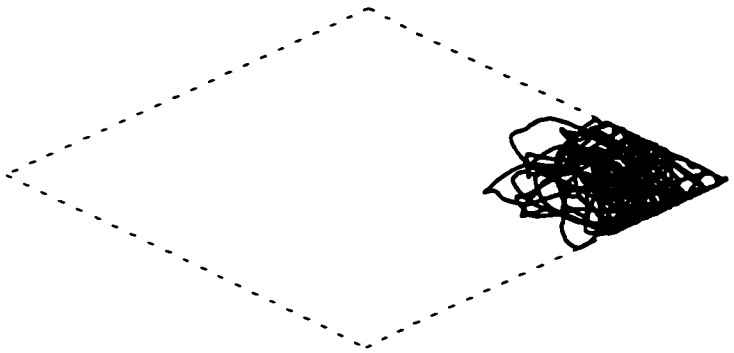

b) Response trajectory

Figure 4.34 Tube in a RFB support

be higher at the pair with the larger angle with drag direction. Figure 4.35 depicts the contact ratio between the tube and support pair A for various flow orientations. For a given support clearance, the contact ratio initially decreases gradually as the flow angle increases. It then decreases sharply to a minimum at a flow angle of 60°. Increasing the flow angle beyond 60° results in an increase in the contact ratio. For a given flow angle, increasing the radial clearance decreases the contact ratio. The rate at which the contact ratio decreases is strongly dependent on the flow angle. For small clearances, flow angles in the range of 100° to 180° have little effect on the contact ratio. For a range of flow angles between 100° and 180°, the contact ratio decreases gradually. This is followed by a sharp drop which decreases asymptotically to zero. In the vicinity of the 60° flow angle, the contact ratio drops dramatically, then decreases asymptotically to zero as the radial clearance increases.

Figure 4.36 shows the contact ratio at pair B. For a flow angle in the range of 0° to 80°, the contact ratio is approximately independent of the flow angle. As the flow angle is increases further, the contact ratio decreases dramatically. The minimum contact ratio occurs at a flow angle of 120°.

Impact forces created at pair A are shown in Figure 4.37. The general behaviour of the dimensionless impact force is maintained for all flow angles. Similar to the contact ratio results, initial increasing of the flow angle reduces the impact forces at pair A. It reaches its minimum value at the 60° flow angle. At this angle, the flow is parallel to pair A, making it perpendicular to the lift force component. The dimensionless impact force then increases gradually to a maximum at a flow angle of 150°.

Figure 4.38 depicts the impact forces at pair B. The dimensionless impact force

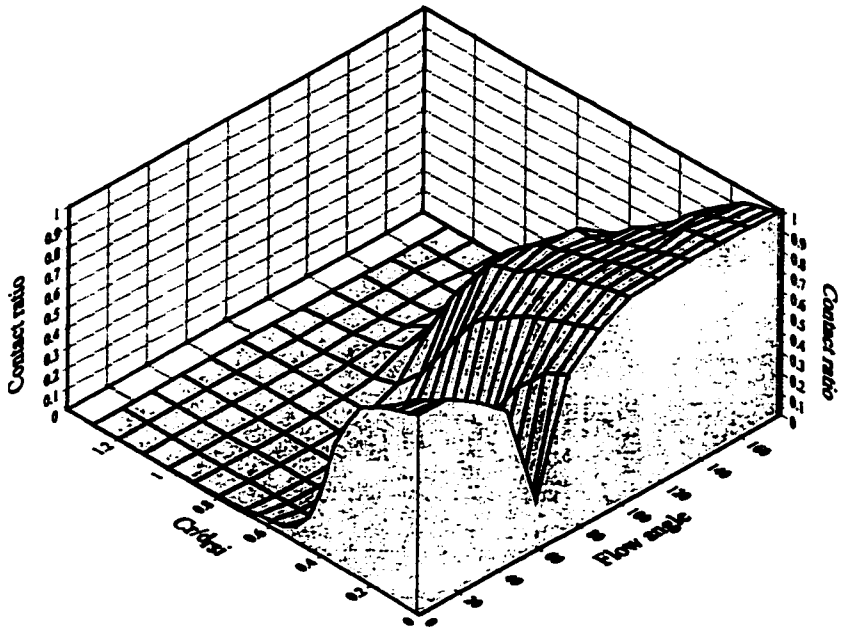

Figure 4.35 Effect of the flow orientation on the contact ratio of the tube with pair A

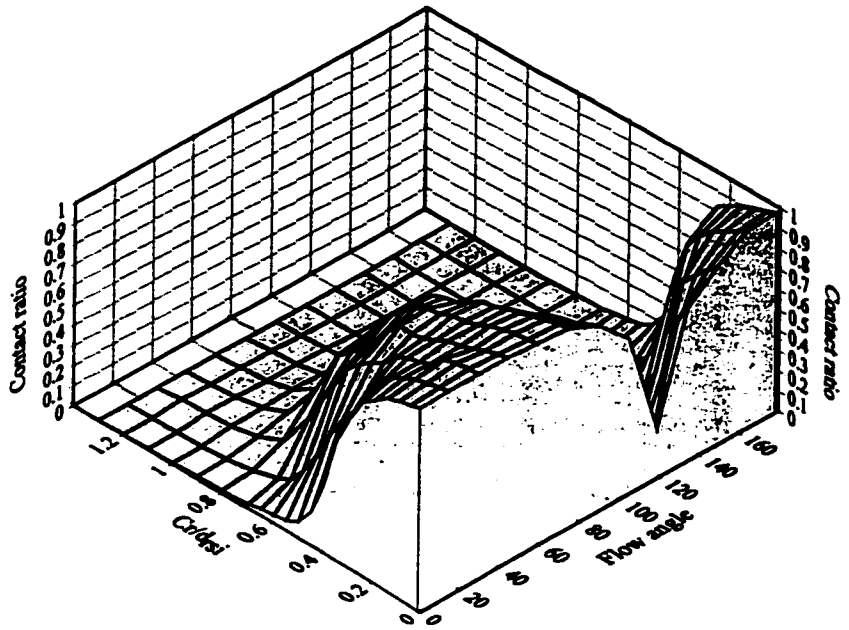

Figure 4.36 Effect of the flow orientation on the contact ratio of the tube with pair B

increases gradually as the flow angle increases, and reaches a maximum value at 30°. This is followed by a reduction to a minimum value at a flow angle of 120°.

In a fashion similar to the contact ratio results, impact forces are affected by the flow angle. The impact force level at each pair is affected by the excitation force level in both the lift and the drag directions depending on the flow angle. Since the force level in the lift direction is lower than that in the drag direction, the maximum impact force level is obtained when the pair under consideration is perpendicular to the direction of the resultant excitation force. On the other hand, the maximum impact force level is obtained when the pair under consideration is at 30° to the flow direction

The predicted normal work rates are presented in Figure 4.39-4.41 in dimensionless form. The dimensionless work rate is normalized by the input power introduced to the tube through turbulence excitation. For a given flow orientation, the general behaviour of the work rate was the same. The normal work rate increases gradually as the clearance increases. The increase in the work rate continues to a certain clearance where less contact is being maintained and the mode switch occurs. The mode switch marks the transition of the tube dynamics from the fixed-pinned to the fixed-free end condition. A further increase in the clearance causes the work rate to drop dramatically. For a given support clearance, the dimensionless work rate at the tube/flat-bar interface of pair A decreases gradually as the flow angle increases (Figure 4.39). The minimum work rate is obtained at a flow angle of 60°. On the other hand, the maximum work rate occurs at the 120° flow angle. The trend of the normal work rate curve at the tube/flat-bar interface of pair B (Figure 4.40) is totally opposite to that of pair A. The maximum and the minimum work rate at pair B occurs at 60°

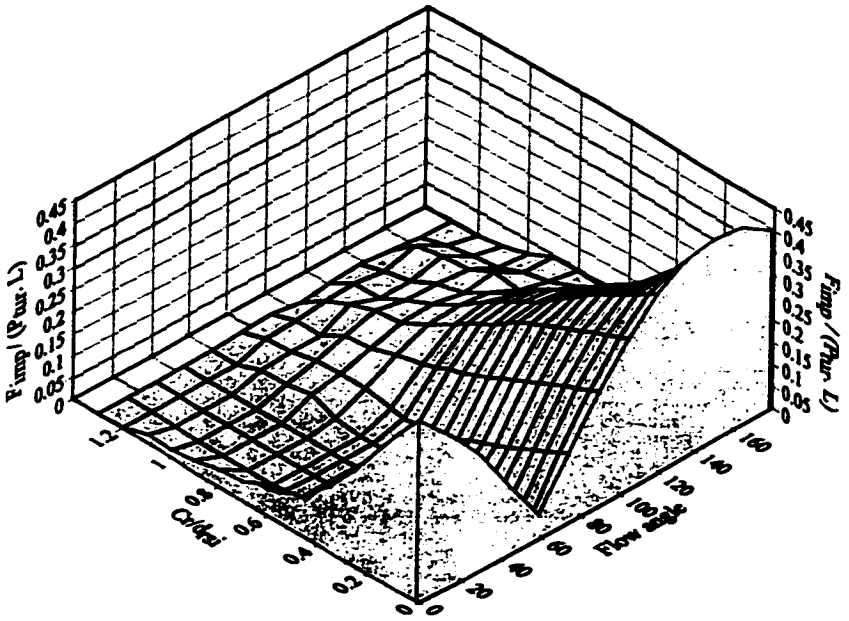

Figure 4.37 Effect of the flow orientation on the RMS impact force of the tube with pair A

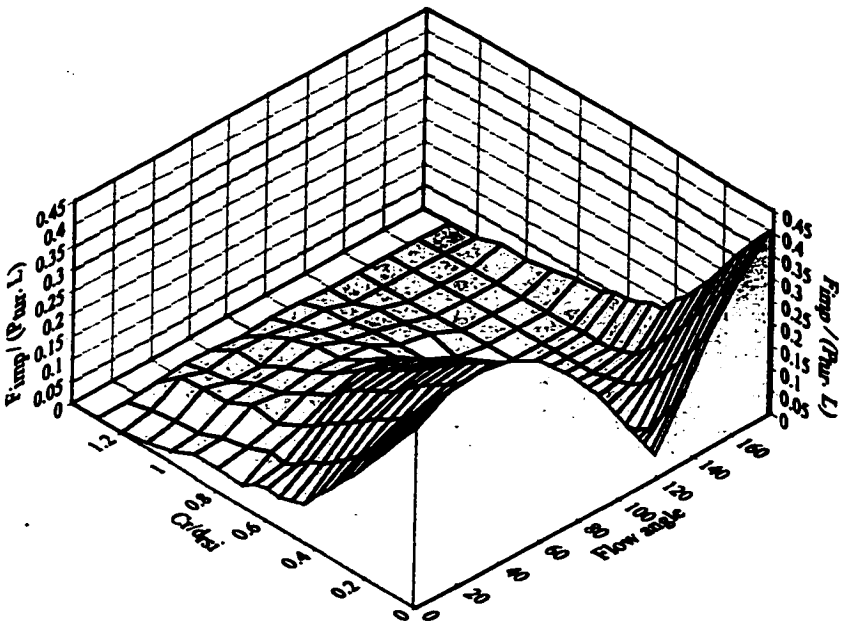

Figure 4.38 Effect of the flow orientation on the RMS impact force of the tube with pair B

and 120° respectively.

The total work rate results are shown in Figure 4.41. The maximum total work rate is obtained at the 60° and the 120° the flow angle. Each of these angles corresponds to a case in which the flow direction is perpendicular to one of the support pairs. The minimum total work rate is obtained at a 0° flow angle. This is associated with both pairs being symmetric about the flow direction. Figure 4.41 suggests an increase in the total work rate for a given clearance when the flow angle increases in the range of 0° to 60°. As the flow angle is further increased, the work rate gradually increases. In addition, the total work rate curve is symmetric about a flow angle of 90°. The maximum total work rate is obtained at flow angles of 60° and 120°. Comparing these results with those of Section 4.5, it can be seen that a flow angle of 60° yields similar results to those of the SFB support. At an angle of 60°, the drag direction is perpendicular to pair B and friction is the main restraint to the tube motion in the lift direction. This situation results in high friction forces and sliding motions at the tube/support interface.

The tube response in the presence of loose supports unfolds in a large variety of contact conditions. These range from continuous contact, to intermediate contact with occasional lift-offs, to intermittent occasional impacts. These contact conditions were investigated through examining the trajectories of the tube response at the support. Figure 4.42 shows a sample of the tube displacement trajectories at a flow angle of 15° for various dimensionless clearances. For a small clearance (Figure 4.42a), the tube's drag forces push the tube against the support corner. For a slightly higher dimensionless clearance (Figure 4.42b), more sliding motion is permitted. Tube lift-off is continuously resisted by the drag,

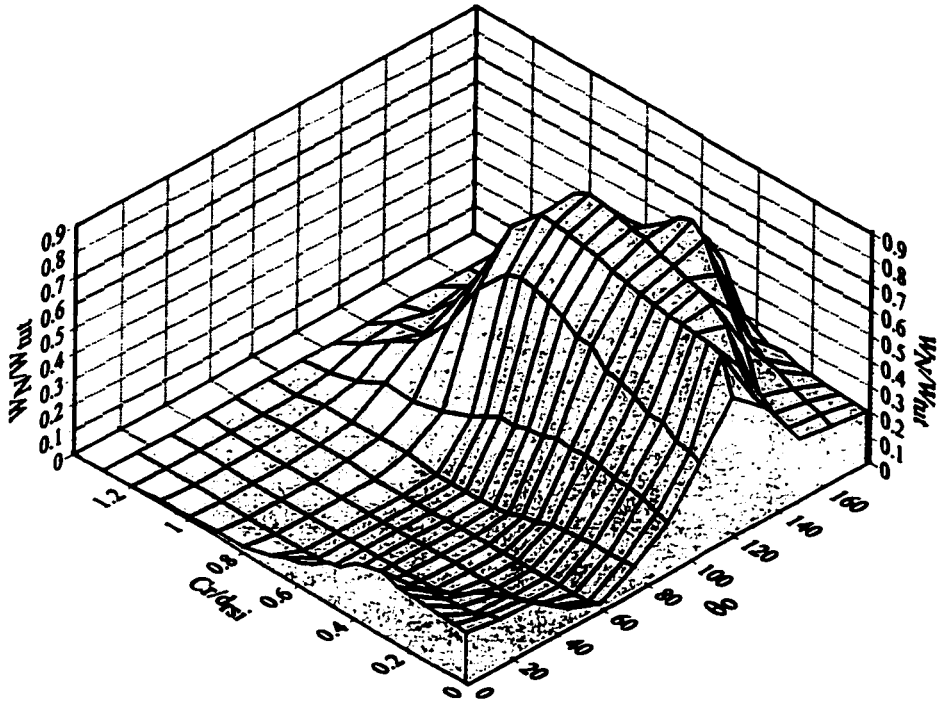

Figure 4.39 Effect of the flow orientation on the normal work rate at pair A

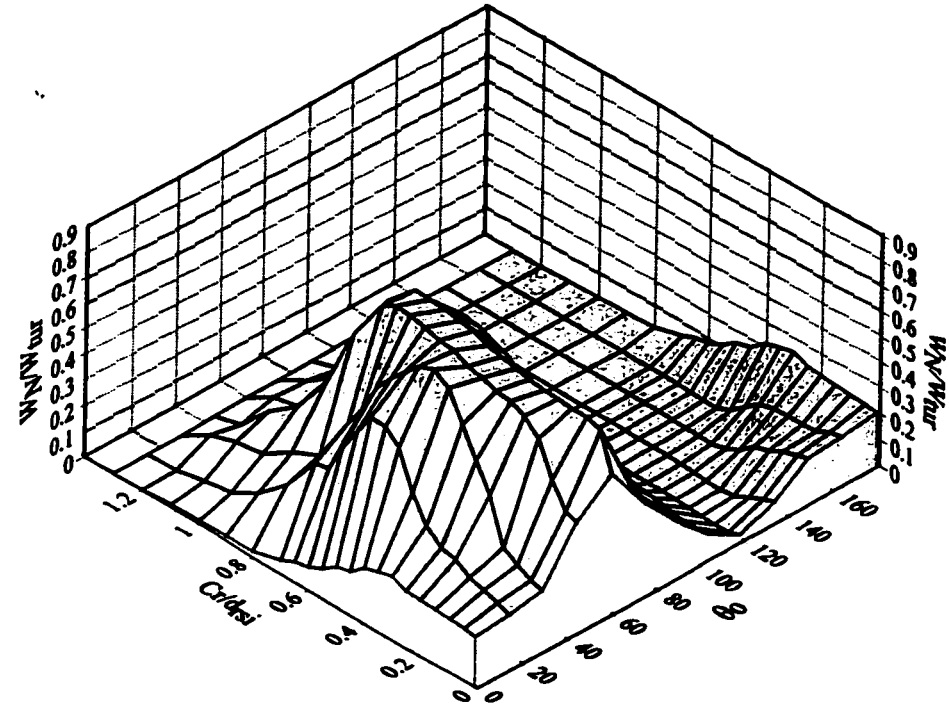

Figure 4.40 Effect of the flow orientation on the normal work rate at pair B

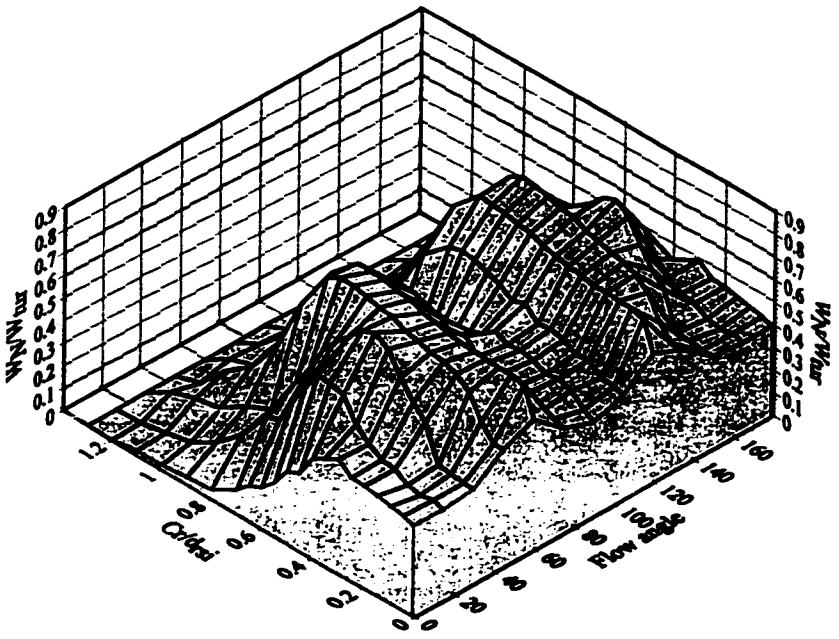

Figure 4.41 Effect of the flow orientation on the total normal work rate

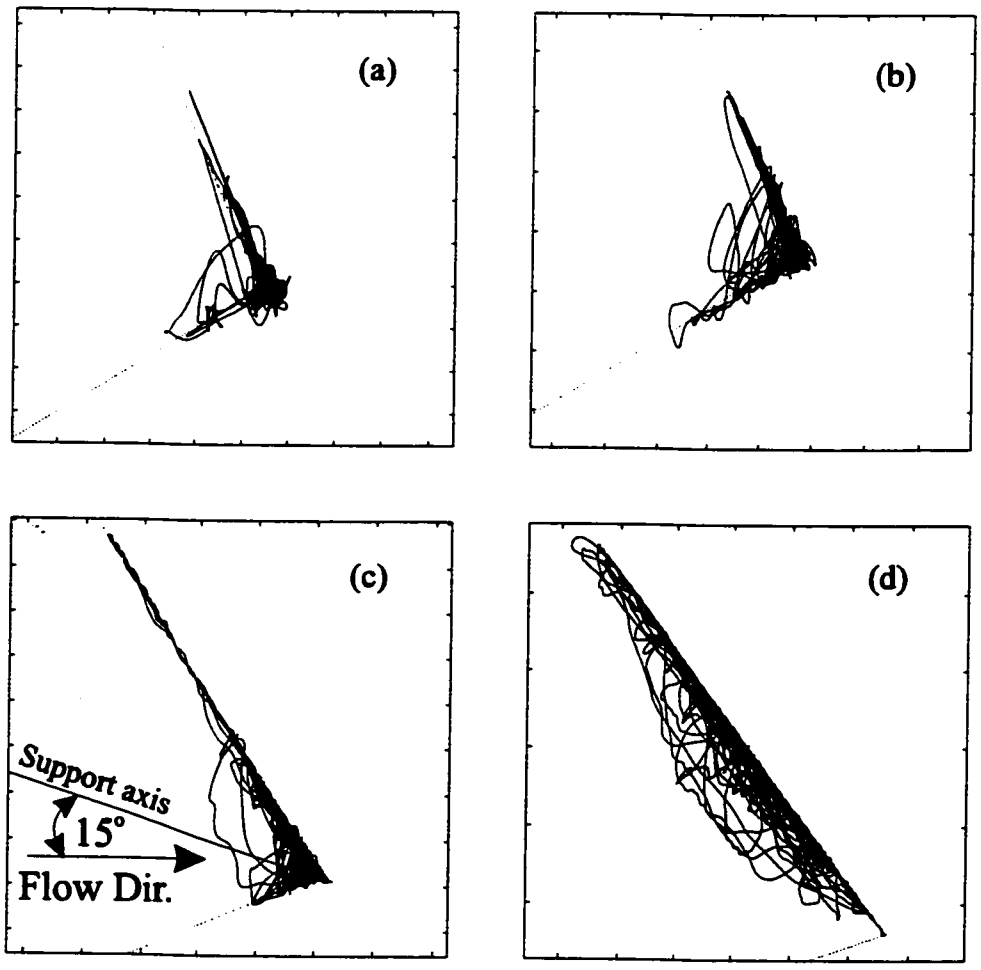

Figure 4.42 Orbital tube motion for a 15° flow angle at various dimensionless clearance. a) 0.15; b) 0.25; c) 0.35; d) 0.6.

while sliding and the motion in the lift direction are resisted by both pairs. Moreover, the tube maintains approximately equal contact with both pairs. For a larger dimensionless clearance (Figure 4.42c), the tube maintains more contact with pair B than with pair A. Hence, the tube motion exhibits higher sliding behaviour along pair B. A further increase in the support clearance causes the tube to impact and slide against pair B only (Figure 4.42d).

Figure 4.43 shows the tube lift response PSD for a tube subjected to crossflow at a 0° flow angle with different clearances. Depending on the clearance value, two groups of frequency peaks can be easily identified. For a small clearance (Figure 4.43a), the PSD of the tube response is dominated by high-frequency peaks at 122, 398, and 831 Hz. These frequencies correspond to the natural frequencies of the fixed-hinged configuration (support-active). Modes related to support active conditions dominate the response for a range of dimensionless clearance values from 0 to 0.4. Within this range of clearances, the impact force amplitude intensifies, the peaks are progressively broadened, and the higher modes are excited (Figure 4.43b). Figure 4.43c depicts the PSD of the tube response for an intermediate clearance where no significant mode is dominant below 120 Hz. With a further increase in clearance, the PSD of the tube response is dominated by another set of frequency peaks (28, 176, 492, and 963 Hz), as shown in Figure 4.43d. These peaks represent the free modes of the tube (support-inactive). This type of behaviour is known as the mode switch and was also observed by Chen et al. (1985).

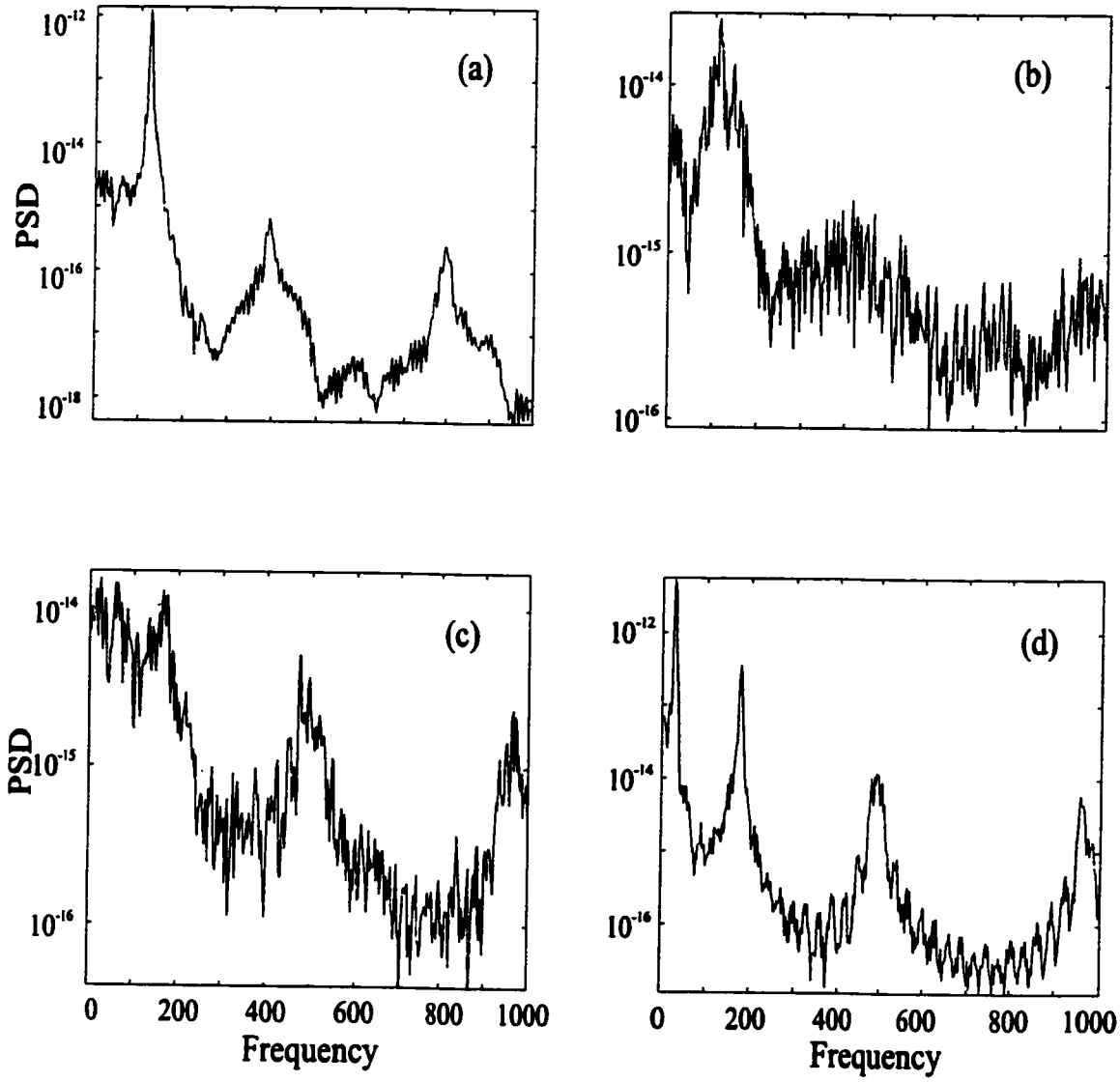

Figure 4.43 Response spectra for various clearances (0° flow angle)
a) 0.01; b) 0.4; c) 0.45; d) 0.8.

The response (lift) spectra of a tube subjected to crossflow at a 30° flow angle are shown in Figure 4.44 Similar to that of a flow angle of 0°, the tube's response depicts a domination of the tube's constrained modes (Figure 4.44a) at a small clearance. As the clearance increases, higher peaks are flattened. At a clearance of 0.25, in addition to the 122 Hz peak, two peaks appears at 28 and 176 Hz. These correspond to the natural frequencies of the unconstrained configuration (Figure 4.44b). As the clearance increases, the amplitude of the 28 Hz mode increases gradually while the amplitude of the 122 Hz mode decreases. At a clearance of approximately 0.3, the 28 Hz peak becomes dominant (Figure 4.44c). The first constrained mode (122 Hz) vanishes at a dimensionless clearance of 0.8. At this point, the response spectrum is essentially composed of the linear unconstrained modes (28, 176, and 492 Hz) as shown in Figure 4.44d.

Figure 4.45 shows the lift response spectra of the 60° flow angle. This case is similar to that of the SFB support. The lift response spectrum (Figure 4.45a) shows the presence of a cluster of low-frequency peaks around 17 Hz in addition to a strong peak at 110 Hz (first constrained mode). A further increase in the clearance causes the disappearance of the 110 Hz peak, and the appearance of peaks at frequencies around those of the unconstrained system (Figure 4.45b). The frequency of the first peak continues to increase gradually with an increase in the clearance (Figure 4.45c). Eventually, at a large clearance, the first peak's frequency coincides with the fundamental frequency of the unconstrained system. The tube's motion in the drag direction is constrained by pair B, while the lift motion is resisted only by the friction forces. This causes an early mode switch of the tube lift response, and it is also responsible for the low frequency modes.

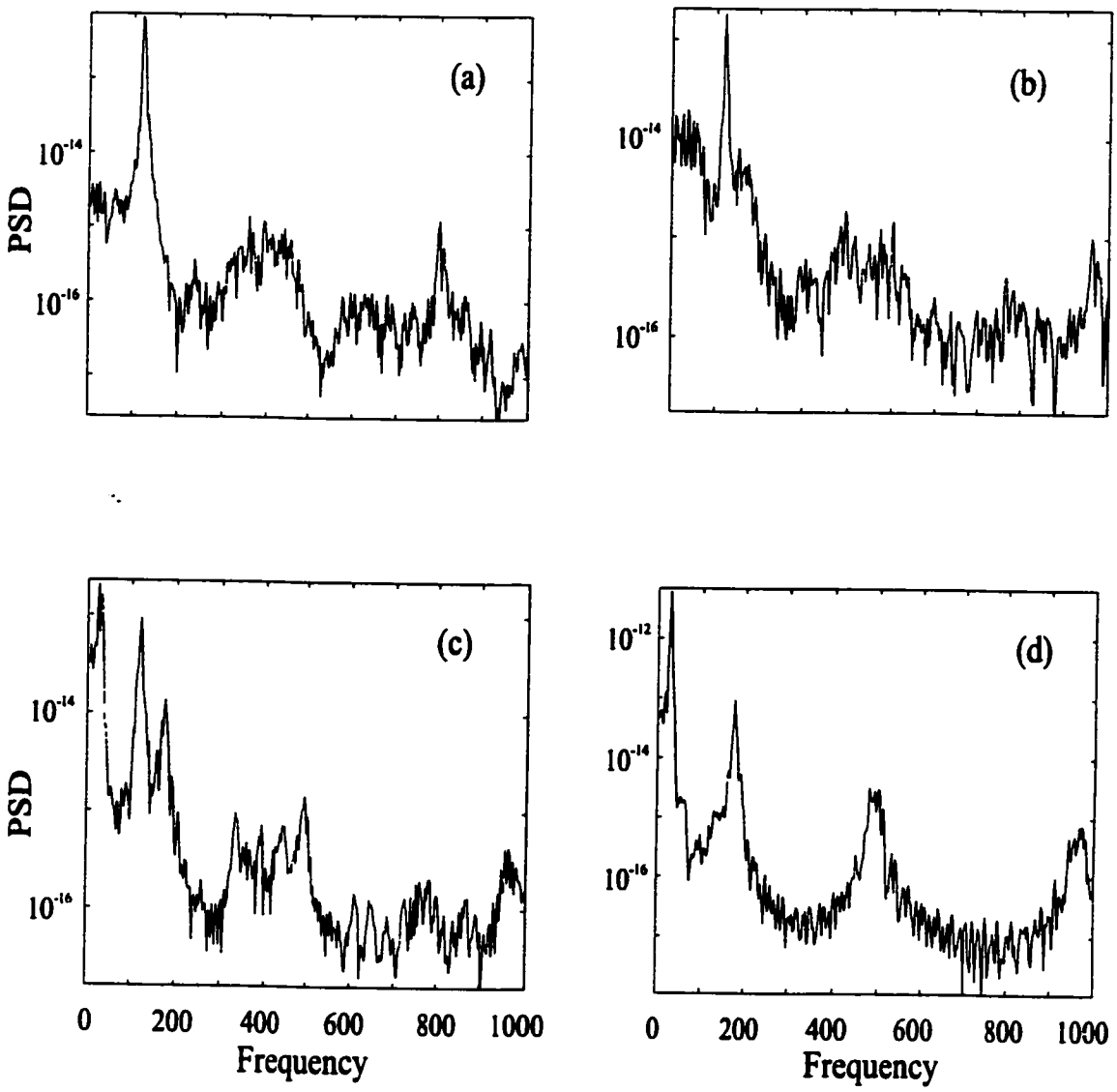

Figure 4.44 Response spectra for various clearances (30° flow angle) a) 0.01; b) 0.25; c) 0.35; d) 1.1.

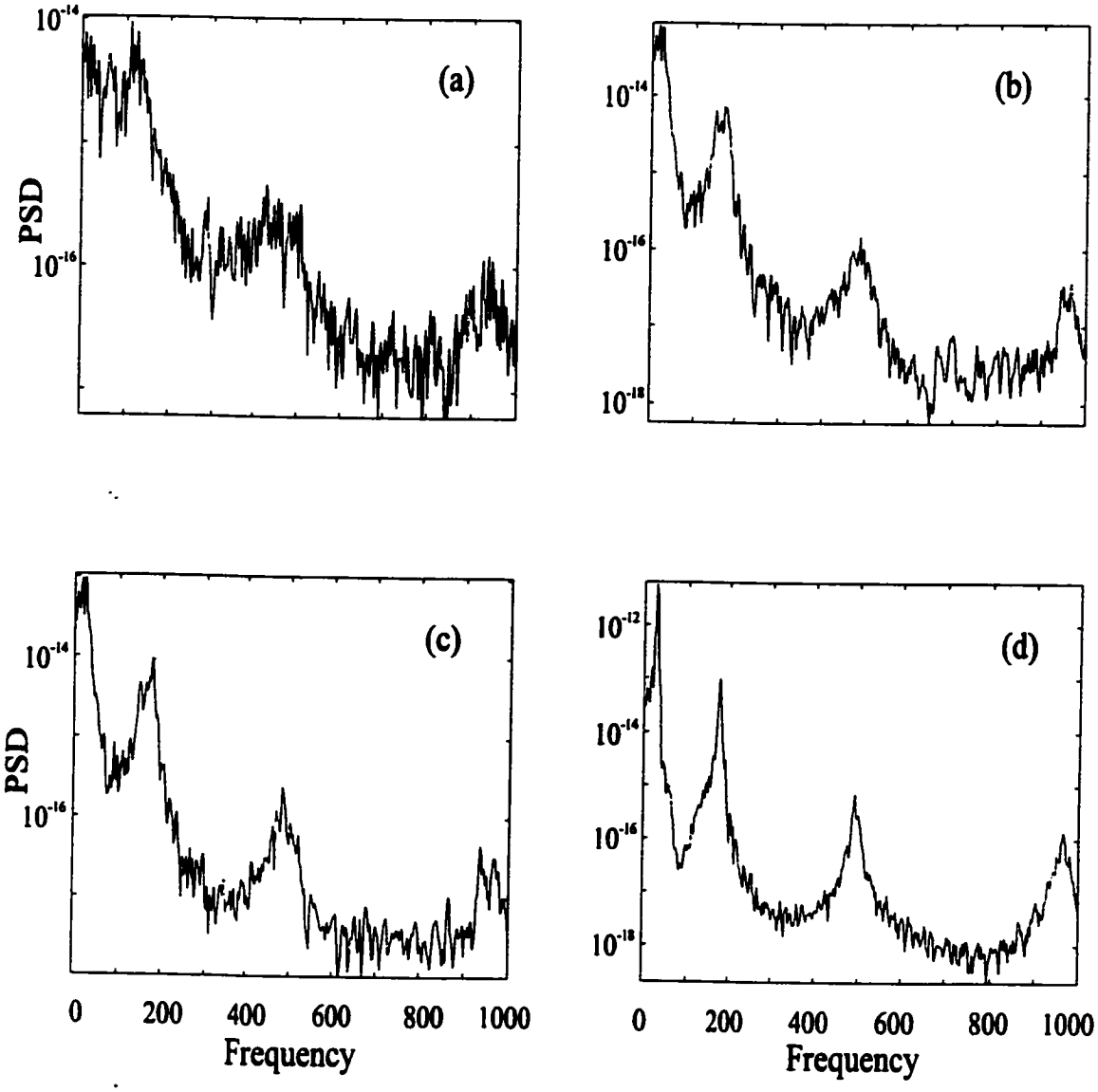

Figure 4.45 Response spectra for various clearances (60° flow angle) a) 0.01; b) 0.35; c) 0.45; d) 1.0.

The unconstrained fundamental frequency represents the lower bounds on the frequency of peaks that may appear in the response spectra. Therefore, the appearance of a cluster of peaks with a central frequency lower than that of the fundamental frequency is somewhat unusual. One question arises immediately: "Is it possible for the system response spectra to contain frequency response peaks that are lower than the fundamental frequency of the unconstrained system?" To address this issue, a single DOF system is considered. The system, shown in Figure 4.46, consists of a mass with friction forces acting between it and the ground. This problem was first treated by Den Hartog (1931), and later by Levitan (1960) and Hundal (1979) by considering harmonic excitation. They showed analytically and experimentally, that the mass may move continuously, or it may come to a stop during parts of each cycle. They also presented plots of the magnification factor as a function of the frequency ratio. These plots show that as the friction force increases, the system response decreases. Moreover, the response peak shifts to a lower frequency. These facts support the results obtained in this section. To further verify the system's behaviour under random external excitation, a limited-band white noise was utilized. The basic parameters of the system are listed in Table 4.3.

Table 4.3 The parameters of the SDOF system

Name	Value	Unit
Mass	$M = 1$	(kg)
Spring	$K = (2\pi)^2$	(N/m)
Damping	$C = 0.125$	(N.s/m)

In this simulation, the temporal integration was carried out using a Rung-Kutta 2nd order method. Friction was imposed by applying a normal force. A friction coefficient of 0.1 was assumed for all of the simulation cases. The ratio of the normal force to the RMS tangential excitation force was varied from 0 to 1. Figure 4.47 shows a sample of the response spectra for various force ratios. It is apparent that with an increase in the friction forces, the response peak flattens due to the increased amount of friction damping. A further increase in the friction forces spreads the response over a wider range of frequencies and hence, a cluster of peaks appear. The central frequency of this cluster shifts gradually to a lower frequency as the friction forces increase. These results confirm the behaviour of the response in the case of a flow angle of 60°.

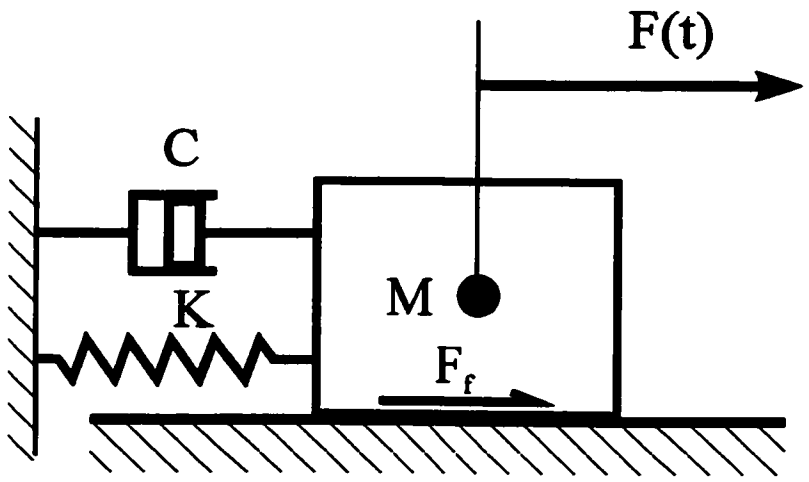

Figure 4.46 SDOF system with friction between the mass and the ground, with random excitation of the mass.

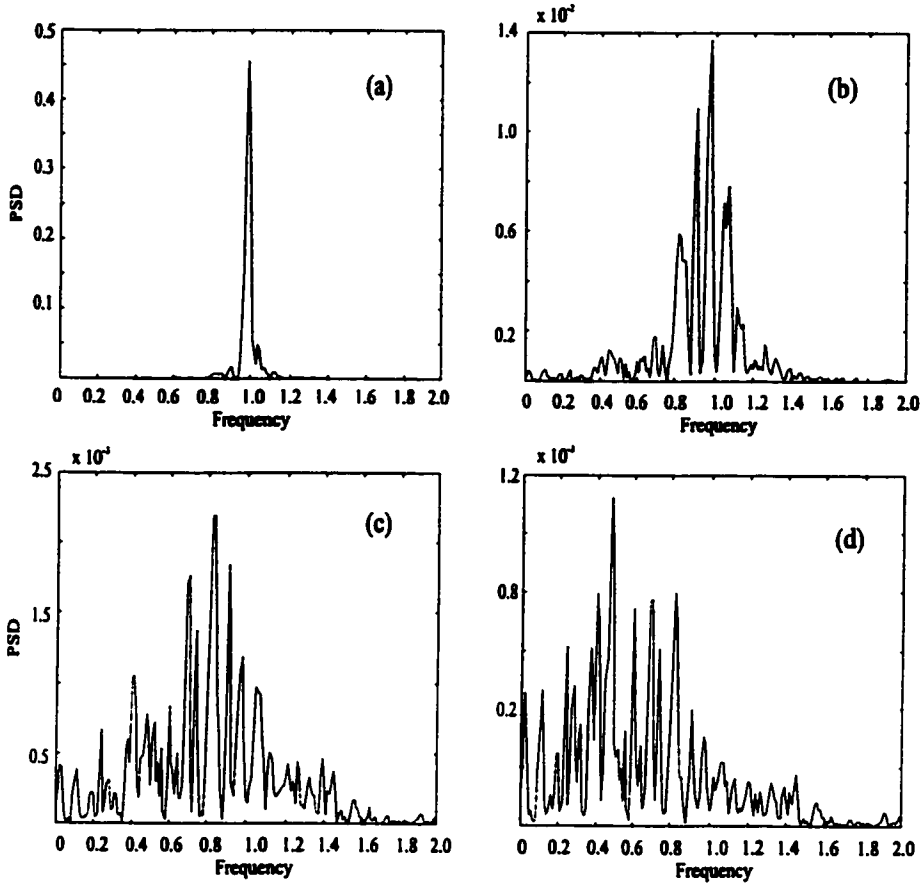

Figure 4.47 PSD of the mass response for different friction-to-excitation force ratios. a) 0; b) 0.3; c) 0.6; d) 0.8.

4. 7 EFFECT OF THE SUPPORT OFFSET

In this section, the effect of support offset on the tube's dynamics is investigated. Support offset is defined as the axial distance between two successive pairs of flat bars (Figure 4.48). Numerical simulations are performed using a single span tube (Configuration 3 of Section 4.3) subjected to a flow velocity of 6 m/s. Support offset values are presented as percentages of the tube length ranging from 0 % to 30%. For each of these support offset values, sixteen radial clearance values are investigated. These simulations were carried out assuming a tube held by a loose RFB support. The cross-flow is assumed to be at a 0° angle with the support axis. Pair B was set at the tip of the tube, while pair A was given a different location along the span to produce the desired offset.

The contact between the tube and a specific pair depends on the location of this pair on the span. The contact ratio for both pairs is therefore the same when the support offset is zero. As the support offset is introduced, the tube maintains an unequal contact ratio with both pairs. Figure 4.49 depicts the contact ratio between the tube and support pair A for various support offset values. For a given dimensionless clearance in the range of 0 to 0.3, the contact ratio increases slightly as the support offset increases. This is attributed to the fact that a vibration node is created at the tip of the tube and hence the displacement is higher towards the mid-span. A higher offset is created by placing a pair of flat bars away from the tip and closer to the mid-span at which the tube exhibits a higher response. A higher tube response results in a higher overlap, and consequently, a higher contact ratio. As was mentioned earlier, if the clearance is increased, the tube loses its effectiveness and a mode switch occurs. This results in a different displacement distribution along the tube's span,

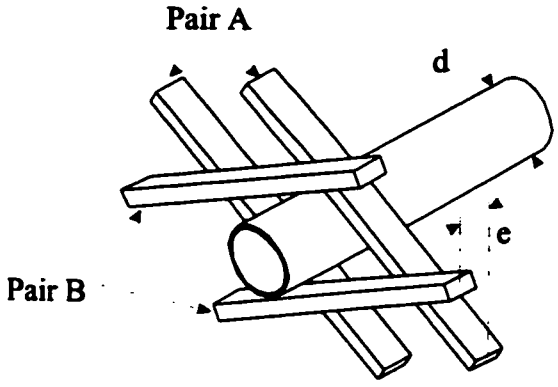

Figure 4.48 Tube in a lattice-bar support with an offset

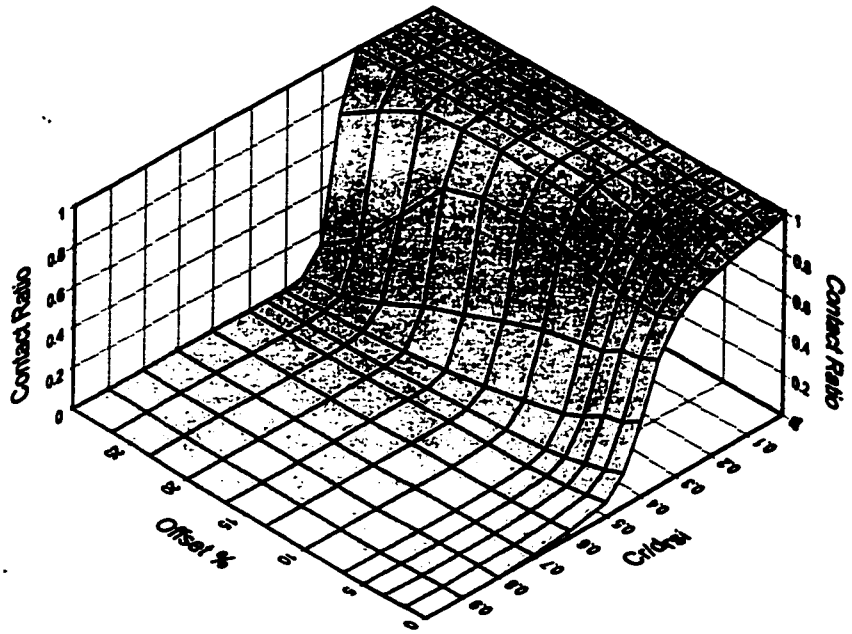

Figure 4.49 Effect of the support offset on the contact ratio between the tube and the support (pair A)

where the maximum displacement is at the tip of the tube. For higher clearances values, increasing the support offset decreases the contact ratio between the tube and pair A. Moreover, the introduction of these offsets does not change the general behaviour of the contact ratio as a function of the clearance. Introduction of the offset results in a region of continuous contact ($Ct = 1$) for a range of small clearances. For example, when the support offset is 6.7 %, the tube remains in continuous contact with pair A up to a dimensionless clearance of approximately 0.2. As the offset increases, the tube maintains continuous contact over a larger clearance range.

Figure 4.50 depicts the contact ratio between the tube and pair B, which is similar to the contact ratio with pair A. The contact ratio for pair B is relatively higher than that of pair A, especially for higher clearances. This is because the support is located at the tip of the tube. As the clearance increases, the tube has less contact with support A, and hence more contact with support B. This can be illustrated by plotting the duty factor R_c versus the dimensionless clearance. The duty factor R_c is defined as follows:

$$R_c = \frac{Ct_A}{Ct_B} \tag{4.4}$$

where Ct_A and Ct_B are the contact ratios at pair A and pair B respectively. Figure 4.51 depicts the duty factor for various support offsets. For a 0 % offset, the contact ratio is the same for pair A and pair B. Therefore, the duty factor is unity for all clearance values. As offset is introduced, R_c is unity up to a certain dimensionless clearance, then it decreases sharply. The larger the offset is, the smaller the duty factor R_c will be.

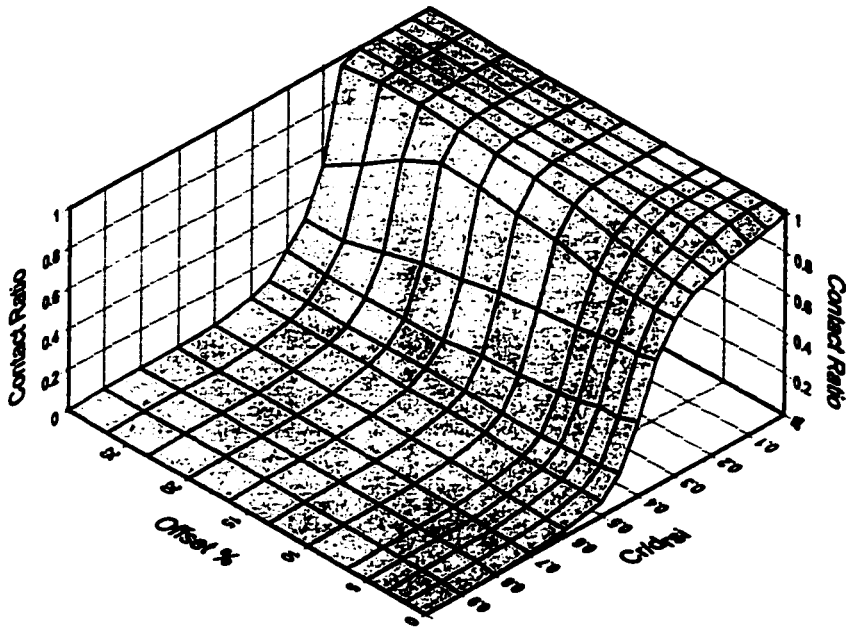

Figure 4.50 Effect of the support offset on the contact ratio between the tube and the support (pair B)

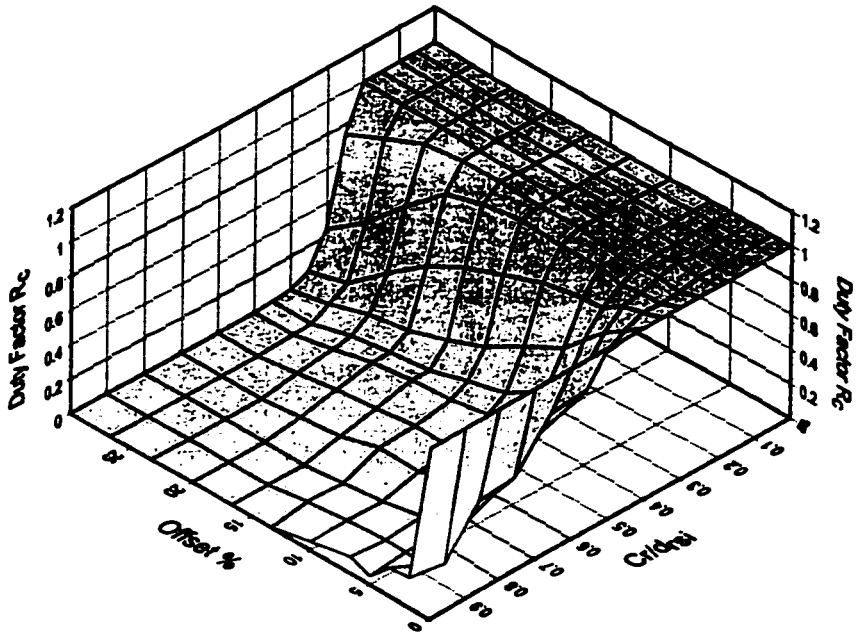

Figure 4.51 Effect of the support offset on the pair contact duty factor

Impact forces created at pair A are shown in Figure 4.52. The general behaviour of the dimensionless impact force is maintained for all support offset values. The introduction of the support offset increases the RMS impact force at pair A in the range of dimensionless clearances up to 0.2. On the other hand, the offset slightly decreases the impact force at pair B (Figure 4.53). The effect of the support offset on the RMS impact forces diminishes after a dimensionless clearance of 0.4.

The behaviour of a tube with a support offset is very complex. The tube response at a particular clearance and offset is composed of a combination of modes. These modes correspond to the possible linear subsystems, *i.e.*, the unconstrained system, the fully constrained system, the system with support active at pair A, or the system with support active at pair B. The term support-active at pair B means that the tube is hinged at pair B and can respond in the plane containing the flat bars of pair A (Figure 4.54). Similarly, the term support active at pair A means that the tube is hinged at pair A and the tube responds in the plane containing the flat bars of pair B (Figure 4.55). The natural frequencies of the tube with support active at pair A are shown in Table 4.4 for various support offsets.

There are three main patterns of tube response observed in the range of support offsets under consideration. For each of these patterns, a sample of response spectra will be presented.

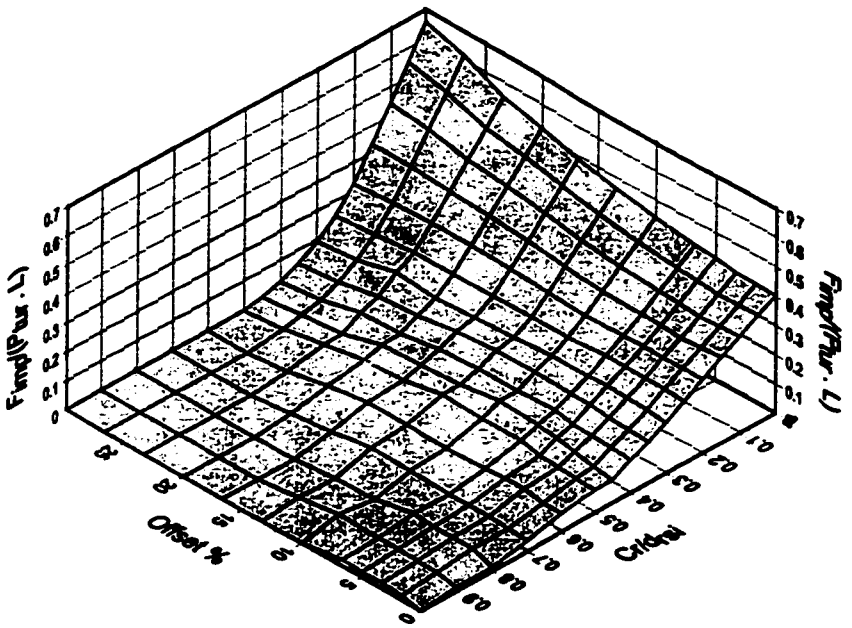

Figure 4.52 Effect of the support offset on the RMS impact force (pair A)

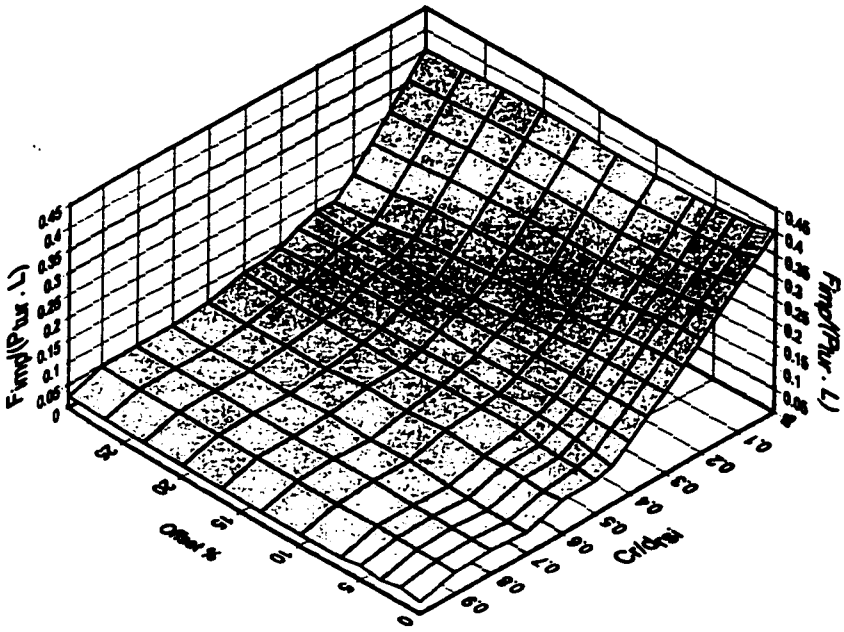

Figure 4.53 Effect of the support offset on the RMS impact force (pair B)

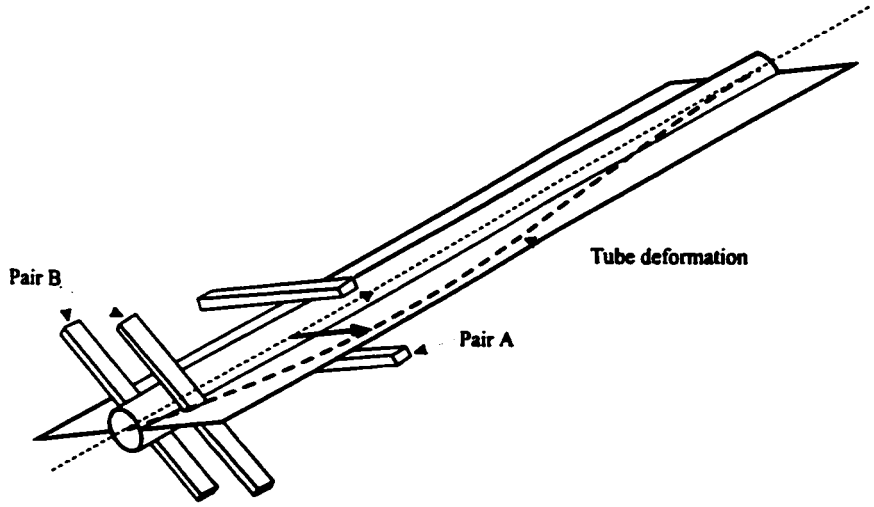

Figure 4.54 Tube motion in the plane of pair A

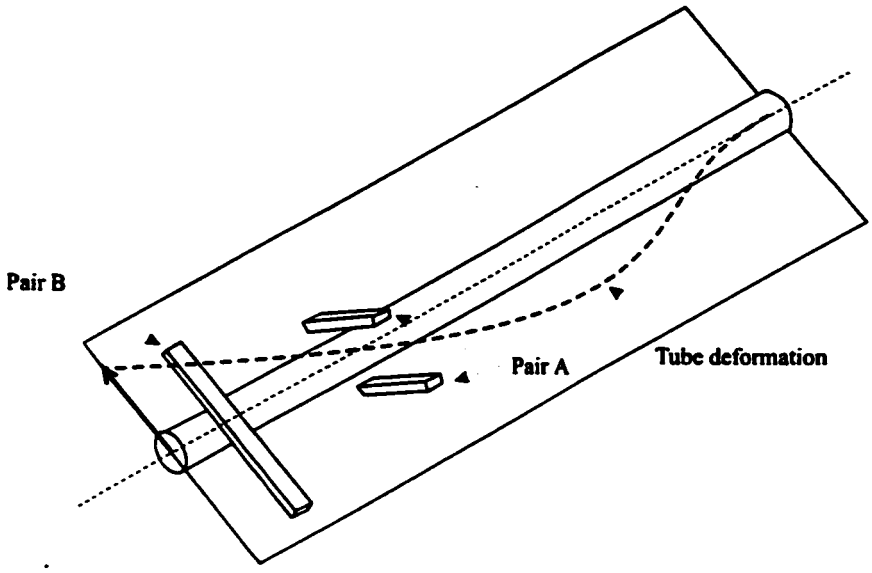

Figure 4.55 Tube motion in the plane of pair B

Table 4.4 Natural frequencies for different support offset values (Support-active at pair A)

Offset	Mode 1	Mode 2	Mode 3
0 %	122	398	831
1.67 %	127	413	861
3.33 %	132	426	888
5 %	137	442	919
6.7 %	140	454	941
10 %	150	480	962
13.3 %	160	492	881
16.7 %	169	470	776
20 %	175	418	756
23.33 %	175	372	784
26.67 %	167	350	833
30 %	152	349	891
Support-inactive	28	176	492

The tube response spectra for a support with a 5% offset are shown in Figure 4.56. The tube response spectra for a small dimensionless clearance of 0.001 is shown in Figure 4.56a which contains several peaks belonging to two different support-active modes. There are two peaks at frequencies of 123 Hz and 137 Hz, which correspond to the fundamental frequency of the support active at B and A respectively. The amplitude of the 137 Hz peak is larger than that of the 123 Hz peak. As the clearance is increased further, the amplitude of the first peak at 123 Hz increases gradually (Figure 4.56b). At a larger clearance (0.35), a single peak appears at a frequency of 127 Hz instead of the two peaks at 123 Hz and 137

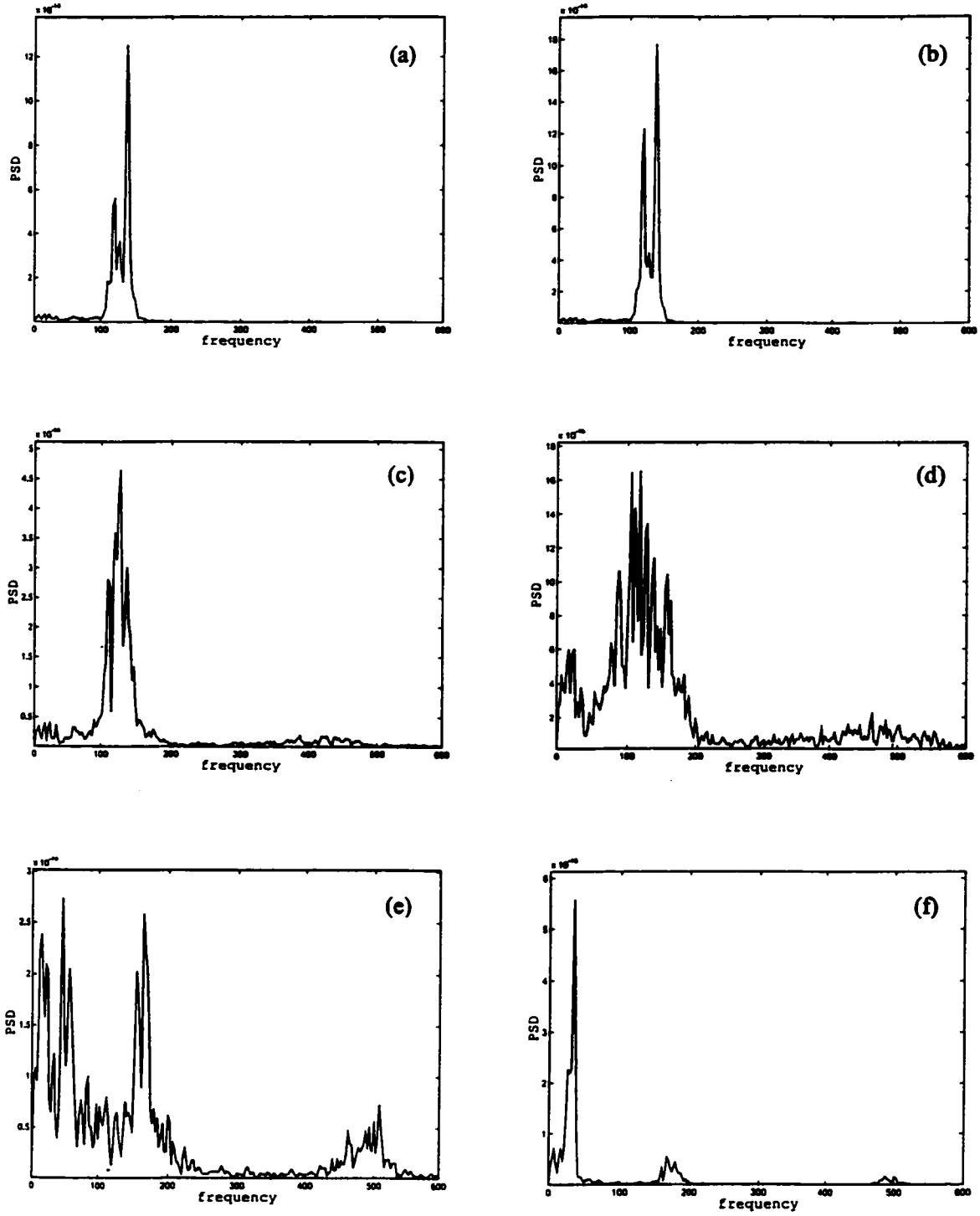

Figure 4.56 Response spectra of a tube lattice-bar support (5% offset) at various dimensionless clearance values. a) 0.001; b) 0.15; c) 0.35; d) 0.4; e) 0.45; f) 0.6.

Hz (Figure 4.56c). At larger dimensionless clearance (0.4), the band width of the fundamental peak increases (Figure 4.56d). At this point, the system is at the point of mode switch. This point is marked by a flattening of the peaks and the appearance of two peaks at 47 Hz and 165 Hz (Figure 4.56e). Moreover, the response spreads over a wider range of frequencies around the first mode. For larger clearances (Figure 4.56f), the frequency of the first two peaks approaches the frequencies corresponding to the natural frequencies of the fixed-free configuration.

The tube response spectra for the case of a support with a 16.7% offset are shown in Figure 4.57. The tube response spectra for a small dimensionless clearance (0.001) are shown in Figure 4.57a. This is a wide-band response which is spread over a range of frequencies (0 Hz to 200 Hz). At a higher clearance (0.25), two well-separated peaks form at frequencies of 120 Hz and 167 Hz. Each of these peaks correspond approximately to the support-active mode of one of the pairs (Figure 4.57b). The amplitude of the first peak, occurring at120 Hz, is larger than that of the second peak, which occurs at 167 Hz. As the clearance increases, the amplitude of the mode which corresponds to the support active at pair A increases (Figure 4.57c). This behaviour continues up to a dimensionless clearance of 0.35. At this clearance, the system approaches the point of mode switch. This is shown in Figure 4.57d. At this point, the two peaks are not well separated, and the response is spread over a wider range of frequencies. For larger clearances (Figure 4.57e), the PSD of the tube response contains peaks at frequencies of 35, 175, and 495 Hz. These frequencies are approximately around those of the natural frequencies of the fixed-free configuration. As the clearance is further increased, these frequencies approach the exact values of the natural frequencies of the unconstrained system.

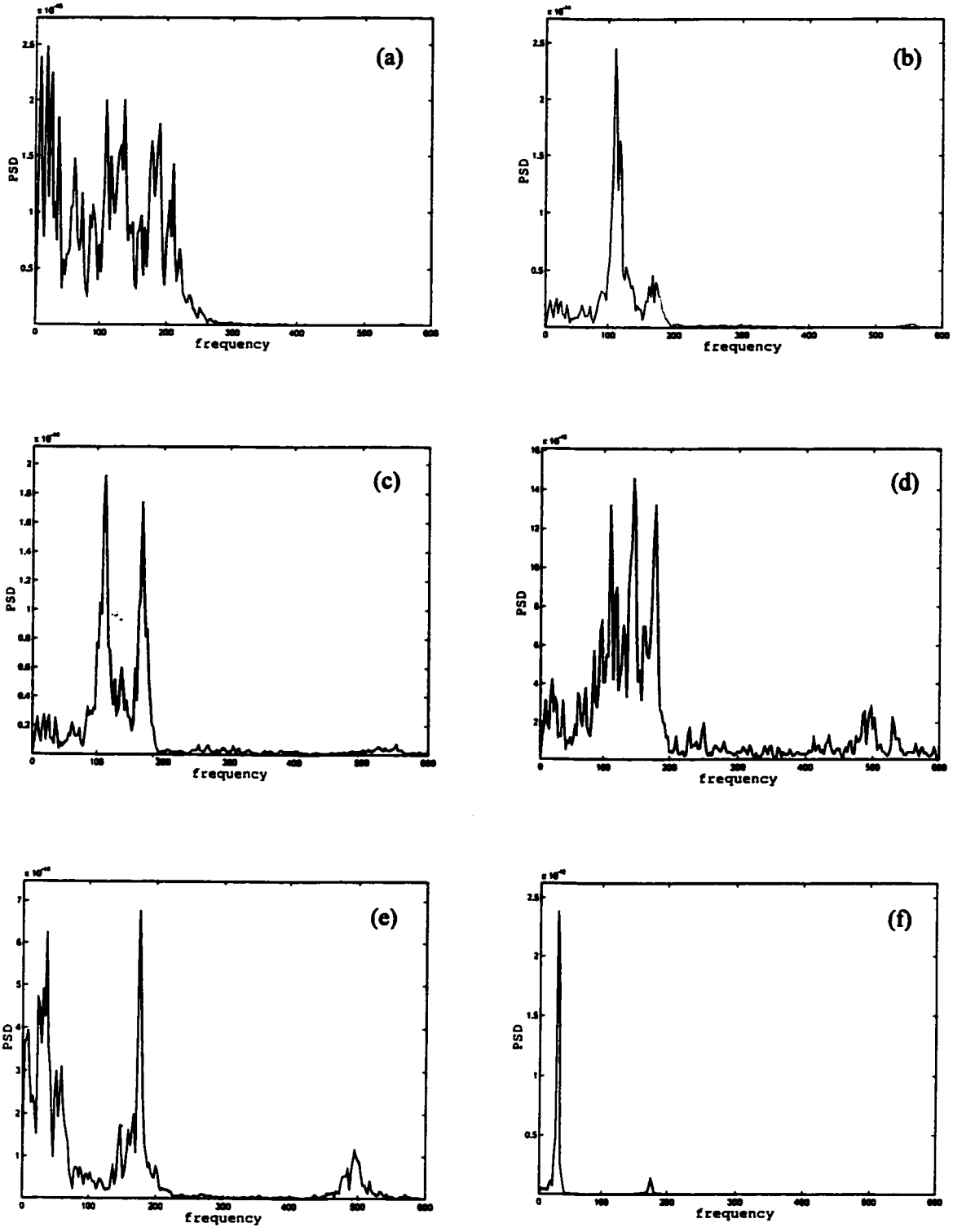

Figure 4.57 Response spectra of a tube lattice bar support (16.67% offset) at various dimensionless clearance values. a) 0.001; b) 0.25; c) 0.3; d) 0.35; e) 0.45; f) 0.7.

Figure 4.58 shows the lift response spectra in the case of a tube with a 23.33% support offset. For a small dimensionless clearance, the lift response spectra (Figure 4.58a) contains a peak at 251 Hz which corresponds to the case where both pairs A and B are active. A further increase in the dimensionless clearance causes the 251 Hz peak to decrease gradually. Concurrently, another peak appears at a frequency of 110 Hz (Figure 4.58b). The peak at 251 Hz vanishes and another peak appears around the frequency of support active at pair A (Figure 4.58c). The frequency of the first peak continues to decrease gradually with an increase in the dimensionless clearance (Figure 4.58d). Yet a further increase in the clearance causes the mode switch to take place (Figure 4.58e). Eventually, at a large dimensionless clearance, the first peak's frequency coincides with the fundamental frequency of the unconstrained system.

The predicted dimensionless normal work rates are presented in Figure 4.59. The introduction of the offset has a dramatic effect on the normal work rate at pair A. For a given dimensionless support clearance in the range of 0 to 0.3, increasing the support offset causes the normal work rate at pair A to increase rapidly. This behaviour is maintained for a support offset in the range of 0 to 10%. This is attributed to the amount of sliding motion permitted in the plane of pair A. When the offset is zero, the tube sliding motion on pair A meets two types of resistance: a) the friction opposing the tube motion in both directions, and b) the flat bar belonging to pair B. As the offset increases, the second constraint becomes less effective since it restrains the tube at a point away from the plane containing pair A. Referring back to Figure 4.54, pair B creates a vibration node at the tip of the tube. In the plane of pair A, friction is the only resistance to the sliding motion along this pair. This

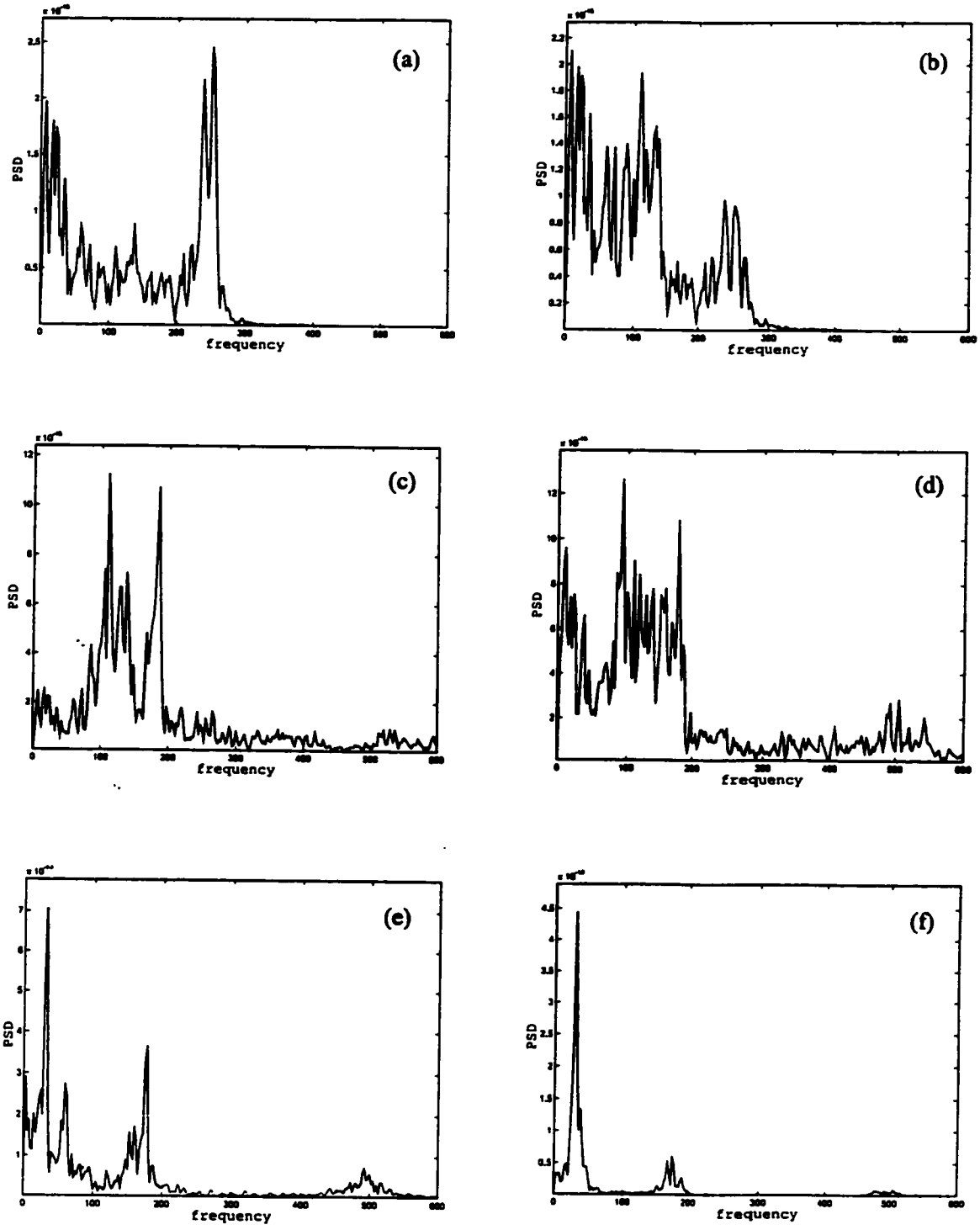

Figure 4.58 Response spectra of a tube lattice-bar support (23.33% offset) at various dimensionless clearance values. a) 0.001; b) 0.15; c) 0.3; d) 0.35; e) 0.4; f) 0.5.

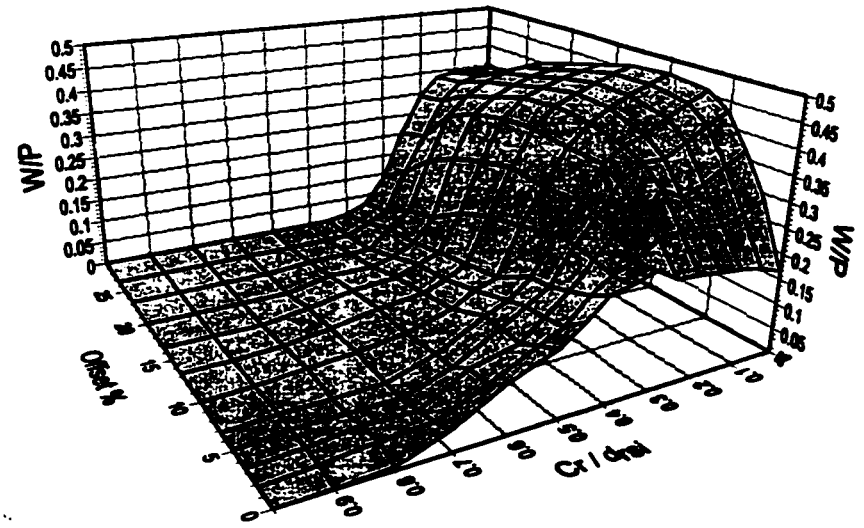

Figure 4.59 Effect of the support offset on the normal work rate (pair A)

situation is applicable as long as the clearance is small enough to permit a support active at the tube tip (pair B). The tube vibration is mainly in the first constrained mode with a frequency of approximately 123 Hz. Therefore, the sliding velocity, which is directly related to the frequency of oscillation, is dependent on the location of the support on the tube. Hence, a higher velocity component in this plane is obtained for a larger offset. Moreover, the sliding velocity also depends on the degree of participation of this mode in the overall system response. For instance, the participation of this mode to the system response as indicated by the PSD of the tube displacement increasing as the offset increases. On the other hand, offsets larger than 10% result in a gradual decrease in the dimensionless work rate. This is attributed to the response of the tube which is a broad-band response covering a low range of frequencies. Now, as the clearance increases, the effectiveness at pair A is reduced. This translates to a slight decrease in the vibration frequency for a range of dimensionless clearances up to 0.3. In addition, the RMS impact force decreases linearly as the dimensionless clearance increases. Therefore, the normal work rate, which is the average product of the impact force and the sliding velocity, decreases almost linearly for this range of dimensionless clearance. The frequency decreases dramatically approaching the dimensionless clearance at which the mode switch occurs. This reflects on the work rate, which decreases sharply as it approaches the mode switch. Moreover, the reduction of the RMS impact force contributes to a reduction in the normal work rate.

Figure 4.60 shows the normal work rate at pair B. Work rate is created through the sliding of the tube along the plane containing pair B. This is shown in Figure 4.55, in which the tube displacement in the plane of pair B is presented. Friction resists tube motion in the

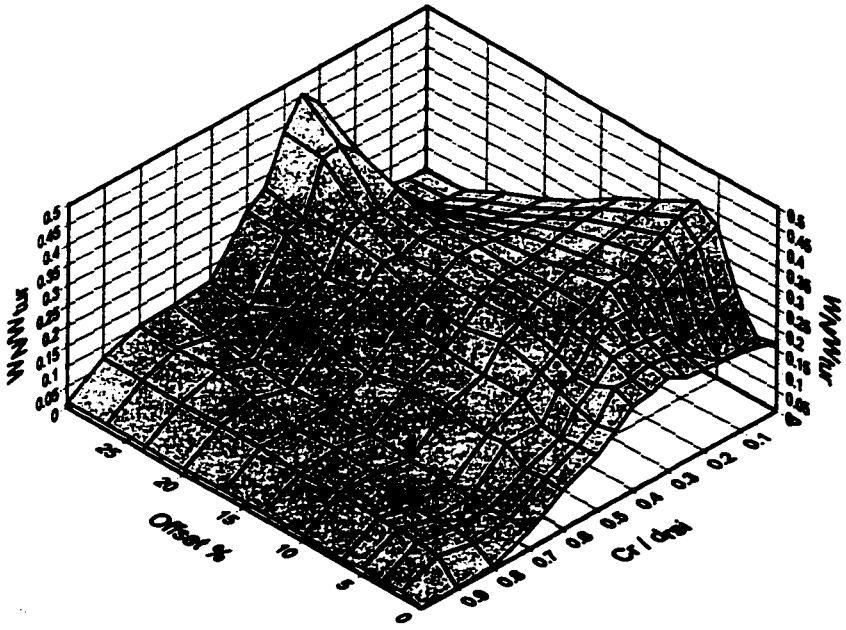

Figure 4.60 Effect of support offset on the normal work rate (pair B)

plane containing pair B. Pair A will create a nodal point at its location as long as the clearance is small. As discussed previously, introducing the offset reduces the physical restraint of the flat bar belonging to pair A to the sliding motion along the flat bars of pair B. This results in an increase in the normal work rate produced at pair B. This behaviour continues to an offset value of 6.67%, after which the normal work rate decreases. In addition, in offsets greater than 20%, the work rate peak is at a dimensionless clearance of approximately 0.35.

4. 8 SUMMARY

In this chapter, numerous simulations have been conducted to understand the tube dynamic behaviour in the presence of gaps at the supports. A cantilever tube supported by a lattice-bar support was considered in this study. The tube was subjected to random distributed forces resembling the turbulence excitation. The tube/support interaction parameters, including contact ratio, RMS impact force, and normal work rate, were calculated for various flow velocities and clearance values. These predicted tube response and tube/support interaction parameters were effectively presented using a set of dimensionless parameters. Utilizing these dimensionless parameters permitted the collapse of the results from various flow velocities over a single curve. Moreover, the proposed set of dimensionless parameters was efficient in collapsing results obtained from tubes with different geometrical and material properties. In addition, a successful application of the dimensionless parameters was also obtained in the case of the multispan tube.

The square-flat-bar (SFB) support and rhomboid-flat-bar (RFB) support were utilized

to study the effect of the support arrangement on the tube dynamics. The comparison demonstrated that the RFB support has a better performance than the SFB support.

The effect of flow orientation was investigated through several simulations utilizing the same tube model. The simulations have shown that the SFB and RFB are two special cases of flow orientation. They also represent an upper and a lower bound for the performance of the lattice-bar support.

Finally, the effect of the support offset on the tube dynamics was presented. Offset has a great impact on the normal work rate. Higher work rates were obtained as a result of introducing offset to the support.

CHAPTER 5

SEGMENT CONTACT MODEL

5. 1 INTRODUCTION

In chapter three, a simple contact model was presented where, the contact between the tube and the support is assumed to occur over a point. Therefore, the principle contact node is the only node that has to be monitored. In other words, the support is assumed to be a knife-edge type of support. However, in reality the support has a finite width which may not be simulated using the current model. Because the current model permits the tube to overlap with the support along the support width, segmental contact may occur.

In this chapter, an enhanced tube-support interaction model is presented. The model considers point-contact and segment contact configurations.

5.2 GENERAL POINT CONTACT MODEL

In this section, a generalized point contact model is developed. This model recognizes the contact of the support edge with any point along the tube. This situation is shown in Figure 5.1 and characterized by an overlap between any of the neighbouring contact nodes and the support plate. Referring to Figure 5.1, A and E represent the current location of the principal contact node (PCN) and the neighbouring contact node (NCN) respectively. Similar to the single contact model, two sets of unit vectors are defined. The tube's axial unit vector is calculated according to the current configuration, such that:

$$\hat{u}_{ta} = \left[\frac{r_x^E - r_x^A}{\Delta r}\right]\cdot\hat{e}_x + \left[\frac{r_y^E - r_y^A}{\Delta r}\right]\cdot\hat{e}_y + \left[\frac{r_z^E - r_z^A}{\Delta r}\right]\cdot\hat{e}_z \tag{5.1}$$

where

$$\Delta r = \left[\left(r_x^E - r_x^A\right)^2 + \left(r_y^E - r_y^A\right)^2 + \left(r_z^E - r_z^A\right)^2\right]^{\frac{1}{2}} \tag{5.2}$$

r_x, r_y, and r_z are position components with respect to the global coordinate system. Superscripts A and E refer to the current location of the PCN and NCN respectively. The tube's tangential and normal unit vectors are shown in Figure 5.2 and are obtained by:

$$\begin{aligned}\hat{u}_{tt} &= \hat{u}_{ta} \times \hat{u}_{smn} \\ \hat{u}_{tn} &= \hat{u}_{tt} \times \hat{u}_{ta}\end{aligned} \tag{5.3}$$

Vectors pointing to the original positions of PCN and NCN are designated as $\bar{A}_o$ and $\bar{E}_o$ respectively. At any instant of time (t), the current position of the PNC and NCN are given by:

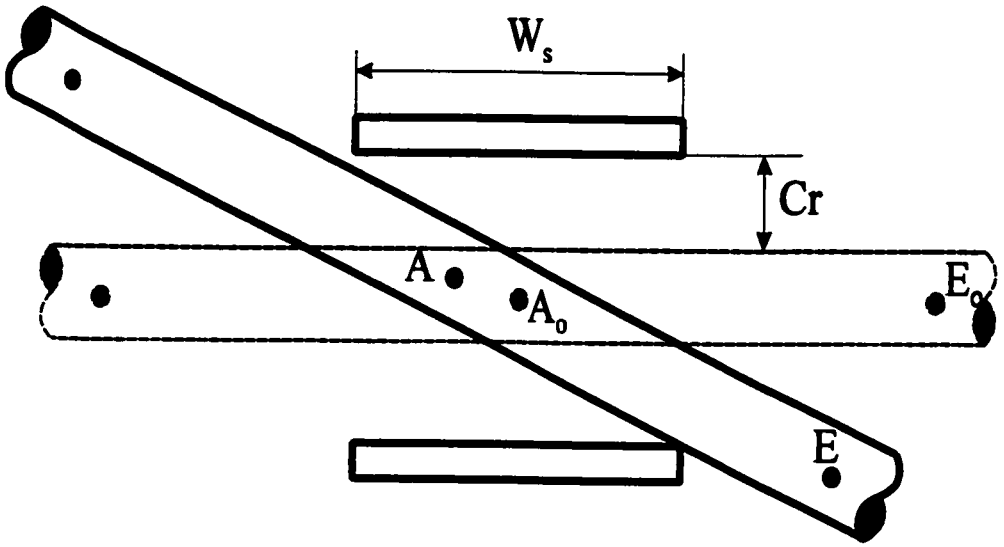

Figure 5.1 Contact node set: Principal Contact Node (A) and Neighbouring Contact Nodes (E)

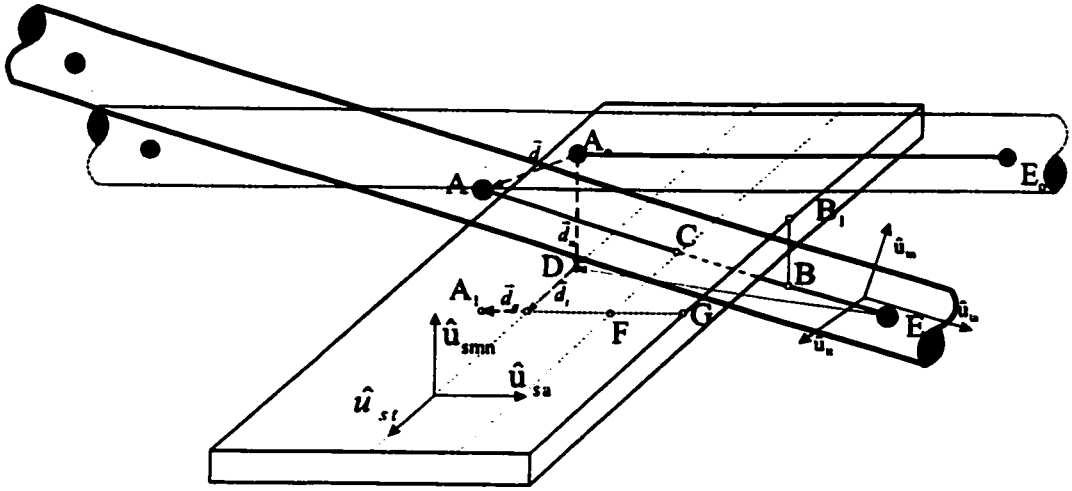

Figure 5.2 Tube-support overlap at a position between the PCN and the NCN

$$\begin{aligned} \vec{A}_t &= \vec{A}_o + \vec{d}_t^{\,A} \\ \vec{E}_t &= \vec{E}_o + \vec{d}_t^{\,E} \end{aligned} \tag{5.4}$$

where $\vec{d}_t^{\,A}$ and $\vec{d}_t^{\,E}$ are the displacement vectors of the PCN and NCN respectively. Both of these displacements have components in the directions of the support unit vectors. These components are axial (d_a), normal (d_n), and tangential (d_t), and can be obtained by the dot-products of the displacement vector ($\vec{d}_t$) and the support unit vectors as follows:

$$\begin{aligned} d_a &= \vec{d}_t \cdot \hat{u}_{sa} \\ d_n &= \vec{d}_t \cdot \hat{u}_{sn} \\ d_t &= \vec{d}_t \cdot \hat{u}_{st} \end{aligned} \tag{5.5}$$

Referring to Figure 5.2, $\vec{D}$ and $\vec{A}_1$ are vectors pointing at the normal projections of points A and A_o, respectively, at the support surface.

$$\begin{aligned} \vec{D} &= \vec{A}_o - \left(\frac{d_{tube}}{2} + Cr \right) \hat{u}_{smn} \\ \vec{A} &= \vec{D} + \left(\vec{d}_t^{\,A} \cdot \hat{u}_{sa} \right) \hat{u}_{sa} + \left(\vec{d}_t^{\,A} \cdot \hat{u}_s \right) \hat{u}_{st} \end{aligned} \tag{5.6}$$

where d_{tube} is the tube's outer diameter. Taking this further, G is the intersection point between the support edge and a vector starting at point A_1, and extending in the direction of the unit vector $\hat{u}_{sa}$.

$$\vec{G} = \vec{A}_1 + \left(\frac{W_s}{2} - d_a \right) \hat{u}_{sa} \tag{5.7}$$

Now, for inter-nodal point contact to occur, three conditions have to be fulfilled:

(1) There must be no overlap between the principal contact node (PCN) and the

support, that is:

$$\vec{d}_t^{\,A} \cdot \hat{u}_{smn} < Cr \tag{5.8}$$

(2) The normal component of the neighbouring contact node (NCN) has to be negative, that is:

$$\vec{d}_t^{\,E} \cdot \hat{u}_{smn} + Cr < 0 \tag{5.9}$$

(3) The point of intersection between the tube's outer surface (C) and the support surface must be located within the support width. This condition is fulfilled by the following inequality:

$$|A_1F| > |A_1G| \tag{5.10}$$

where

$$\begin{aligned} A_1F &= \overline{A}\overline{C} \cdot \hat{u}_{sa} \\ |A_1G| &= \left| \frac{W_s}{2} \cdot \hat{u}_{sa} + \vec{d}_t^{\,A} \cdot \hat{u}_{sa} \right| \end{aligned} \tag{5.11}$$

The point of intersection of the tube and the support (point *B*) can be obtained from the following:

$$\frac{AB}{AC} = \frac{AB \cdot \hat{u}_{sa}}{AE \cdot \hat{u}_{sa}} \tag{5.12}$$

The displacement at point *B* is obtained by using the beam interpolation functions that relate the displacement at any point along the beam element to the nodal displacements. Hence the normal displacement at point *B* is given by:

$$d_n^B(\eta) = \phi_1(\eta)\, d_n^A + \phi_2(\eta)\, \theta_t^A + \phi_3(\eta)\, d_n^E + \phi_4(\eta)\, \theta_t^E \tag{5.13}$$

where d_n^B is the displacement of point B and $\eta = AB/L_e$ is the dimensionless distance of point B from node A. The maximum penetration distance (δ_B) is defined by the distance between point B and the support plane.

$$\delta_B = d_n^B - Cr \tag{5.14}$$

The impact force can be calculated by:

$$\begin{aligned} \bar{F}_{imp} &= \bar{F}_{spr} + \bar{F}_{dmp} \\ \bar{F}_{spr} &= \left(K_{spr}\, \delta_B\right) \cdot \hat{u}_{smn} \\ \bar{F}_{dmp} &= -sign(\dot{\delta}_B)\left(1.5a \left|F_{spr}\dot{\delta}_B\right|\right) \cdot \hat{u}_{smn} \end{aligned} \tag{5.15}$$

The impact force can be decomposed into components in the normal and axial tube local directions:

$$\begin{aligned} F_{in} &= \bar{F}_{imp} \cdot \hat{u}_{tn} \\ F_{ia} &= \bar{F}_{imp} \cdot \hat{u}_{ta} \end{aligned} \tag{5.16}$$

The frictional force acts in the plane containing the tube tangential and the axial unit vectors. In order to calculate the frictional force, it is necessary to calculate the tube tangential velocity in the friction plane. The resultant tangential velocity, $\bar{V}_{rt}^B$, in the friction plane is calculated by the vectorial sum of the tube velocity components in the direction of $\hat{u}_{ta}$ and $\hat{u}_{tt}$. It must be noted that the velocity of point B has to be obtained by interpolating the

velocity with respect to the nodal velocities. Frictional force and moment vectors can be calculated by Equations (3.25 and 3.26). Resultant frictional forces and moments are then translated to the tube local coordinates as follows:

$$\begin{aligned} F_{fa} &= \bar{F}_f \cdot \hat{u}_{ta} \\ F_{ft} &= \bar{F}_f \cdot \hat{u}_{tt} \\ M_{fa} &= \bar{M}_f \cdot \hat{u}_{ta} \\ M_{ft} &= \bar{M}_f \cdot \hat{u}_{tt} \end{aligned} \tag{5.17}$$

Now the total contact forces and moments in the local tube directions are:

$$\begin{aligned} F_{ca} &= F_{ia} + F_{fa} \\ F_{cn} &= F_{in} \\ F_{ct} &= F_{ft} \\ M_{ca} &= M_{fa} \\ M_{cn} &= 0 \\ M_{ct} &= M_{ft} \end{aligned} \tag{5.18}$$

The above expressions define the components of the contact forces at impact point *B*. However, in the finite element solution to structural vibrations, loads are applied at the nodes. Therefore, the impact and friction forces have to be expressed as concentrated loads and moments applied at the nodes. These nodal forces must be equivalent to these forces, in a virtual work sense. In other words, the work done by the impact forces is equal to the work done by the equivalent concentrated forces on the nodes. The work done by the impact and frictional forces is:

$$W = F_{ca} d_a^B(\zeta) + F_{cn} d_n^B(\zeta) + F_{ct} d_t^B(\zeta) + M_a \theta_a^B(\zeta) + M_n \theta_n^B(\zeta) + M_t \theta_t^B(\zeta) \tag{5.19}$$

The displacement components at any point (at a dimensionless distance $\zeta=x/L_e$) are interpolated as follows:

$$\begin{aligned}
d_a^B &= \psi_1(\zeta)d_a^A + \psi_2(\zeta)d_a^E \\
d_n^B &= \phi_1(\zeta)d_n^A + \phi_2(\zeta)\theta_t^A + \phi_3(\zeta)d_n^E + \phi_4(\zeta)\theta_t^E \\
d_t^B &= \gamma_1(\zeta)d_t^A + \gamma_2(\zeta)\theta_n^A + \gamma_3(\zeta)d_t^E + \gamma_4(\zeta)\theta_n^E \\
\theta_a^B &= \lambda_1(\zeta)\theta_a^A + \lambda_2(\zeta)\theta_a^E \\
\theta_n^B &= \beta_1(\zeta)d_t^A + \beta_2(\zeta)\theta_n^A + \beta_3(\zeta)d_t^E + \beta_4(\zeta)\theta_n^E \\
\theta_t^B &= \sigma_1(\zeta)d_n^A + \sigma_2(\zeta)\theta_t^A + \sigma_3(\zeta)d_n^E + \sigma_4(\zeta)\theta_t^E
\end{aligned} \tag{5.20}$$

Substituting in Equation (5.19)

$$\begin{aligned}
W = {} & d_a^A\left(F_{ca}\psi_1(\zeta)\right) + d_n^A\left(F_{cn}\phi_1(\zeta) + M_{ct}\sigma_1(\zeta)\right) + d_t^A\left(F_{ct}\gamma_1(\zeta)\right) + \\
& \theta_a^A\left(M_{ca}\lambda_1(\zeta)\right) + \theta_n^A\left(F_{ct}\gamma_2(\xi)\right) + \theta_t^A\left(F_{cn}\phi_2(\xi) + M_{ct}\sigma_2(\zeta)\right) + \\
& d_a^E\left(F_{ca}\psi_2(\zeta)\right) + d_n^E\left(F_{cn}\phi_3(\zeta) + M_{ct}\sigma_3(\zeta)\right) + d_t^E\left(F_{ct}\gamma_3(\zeta)\right) + \\
& \theta_a^E\left(M_{ca}\lambda_2(\zeta)\right) + \theta_n^E\left(F_{ct}\gamma_4(\xi)\right) + \theta_t^E\left(F_{cn}\phi_4(\xi) + M_{ca}\sigma_4(\zeta)\right) \\
= {} & \{u\}\{P\}
\end{aligned} \tag{5.21}$$

Hence, the consistent load vector equivalent to the impact and frictional forces is expressed by:

$$\{P\} = \begin{Bmatrix} F_{ca}\psi_1(\zeta) \\ F_{cn}\phi_1(\zeta) + M_{ct}\sigma_1(\zeta) \\ F_{ct}\gamma_1(\zeta) \\ M_{ca}\lambda_1(\zeta) \\ F_{ct}\gamma_2(\xi) \\ F_{cn}\phi_2(\xi) + M_{ct}\sigma_2(\zeta) \\ F_{ca}\psi_2(\zeta) \\ F_{cn}\phi_3(\zeta) + M_{ct}\sigma_3(\zeta) \\ F_{ct}\gamma_3(\zeta) \\ M_{ca}\lambda_2(\zeta) \\ F_{ct}\gamma_4(\xi) \\ F_{cn}\phi_4(\xi) + M_{ca}\sigma_4(\zeta) \end{Bmatrix} \tag{5.22}$$

Now the global components of the load vector at nodes A and E are obtained by multiplying each force component with its respective unit vector.

5. 3 SEGMENT CONTACT

Segment contact occurs when the displacements of the PCN and/or an NCN exceed the support gap. Either of the aforementioned conditions will lead to a segment contact. Each of these conditions is discussed further, as follows:

Case 1: Displacements of the PCN and an NCN exceed the support gap

This condition is expressed mathematically as follows:

$$\begin{aligned} \bar{d}^{A} \cdot \bar{u}_{smn} &> Cr \\ \bar{d}^{E} \cdot \bar{u}_{smn} &> Cr \end{aligned} \tag{5.23}$$

Case 2: Displacement of the PCN exceeds the support gap

This condition is expressed mathematically as follows:

$$\begin{aligned} \vec{d}^{A} \cdot \vec{u}_{smn} &> Cr \\ \vec{d}^{E} \cdot \vec{u}_{smn} &< Cr \end{aligned} \tag{5.23}$$

In both cases, the dimensionless overlap segment must be calculated The dimensionless overlap segment is defined as the ratio of the contact segment length to the element length:

$$\eta = \frac{A_1 B_3}{A_1 E_3} \tag{5.24}$$

where A_1E_3 and A_1B_3 are projections of the element length, and the contact segment on the support's axial unit vector respectively (Figure 5.3 and Figure 5.4).

Contact forces can be calculated by considering a distributed stiffness along the contact segment as shown in Figure 5.5. The strain energy of the distributed stiffness is given by:

$$U_k = \int_0^b \left(\frac{1}{2} K_g \left(d_n(x) - Cr \right)^2 \right) dx \tag{5.25}$$

where K_g is the gap stiffness per unit length which is assumed to be constant and distributed over the overlap segment (b). The displacement $d_n(x)$ is interpolated using Equation (5.20). Hence Equation(5.25) becomes:

$$U_k = \frac{K_g L_e}{2} \int_0^{\eta} \left(d_n(\zeta) - Cr \right)^2 d\zeta \tag{5.26}$$

Carrying out the integration of Equation (5.26) results in:

$$U_s = \frac{K_g L_e}{2} \begin{pmatrix} \left(d_n^A\right)^2 H_1 + L d_n^A \theta_t^A H_2 + d_n^A d_n^E H_3 + L d_n^A \theta_t^E H_4 + d_n^A Cr H_5 + \\ L^2 \left(\theta_t^A\right)^2 H_6 + L \theta_t^A d_n^E H_7 + L^2 \theta_t^A \theta_t^E H_8 + L \theta_t^A Cr H_9 + \\ \left(d_n^E\right)^2 H_{10} + L d_n^E \theta_t^E H_{11} + d_n^E Cr H_{12} + L^2 \left(\theta_t^E\right)^2 H_{13} + \\ L \theta_t^E Cr H_{14} + (Cr)^2 H_{15} \end{pmatrix} \tag{5.27}$$

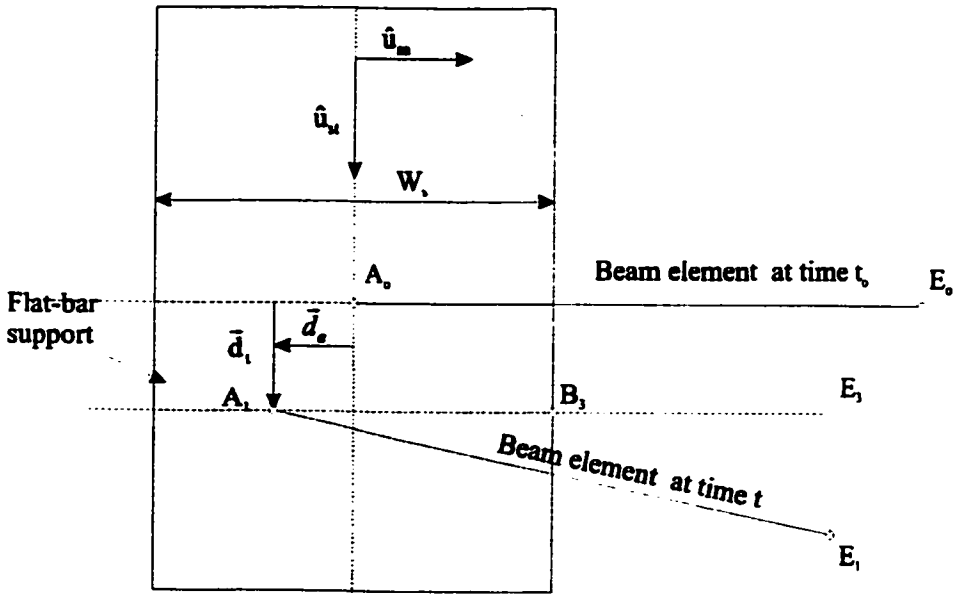

Figure 5.3 Determination of the overlap segment for case 1

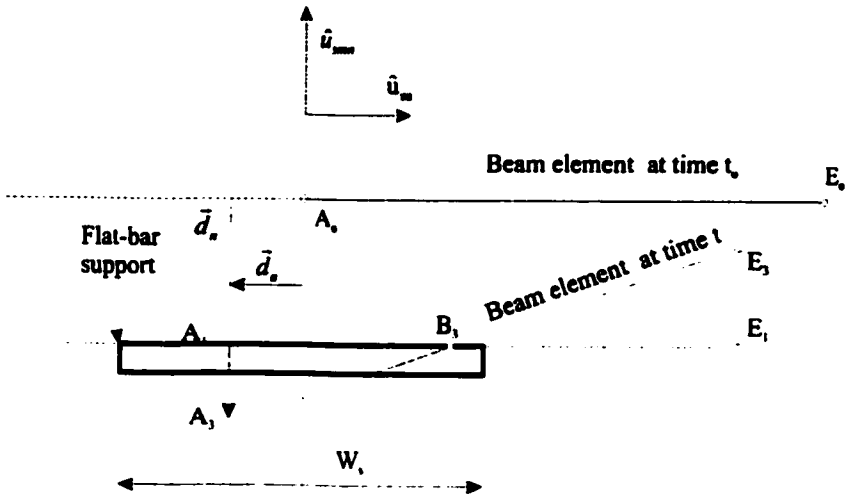

Figure 5.4 Determination of the overlap segment for case 2

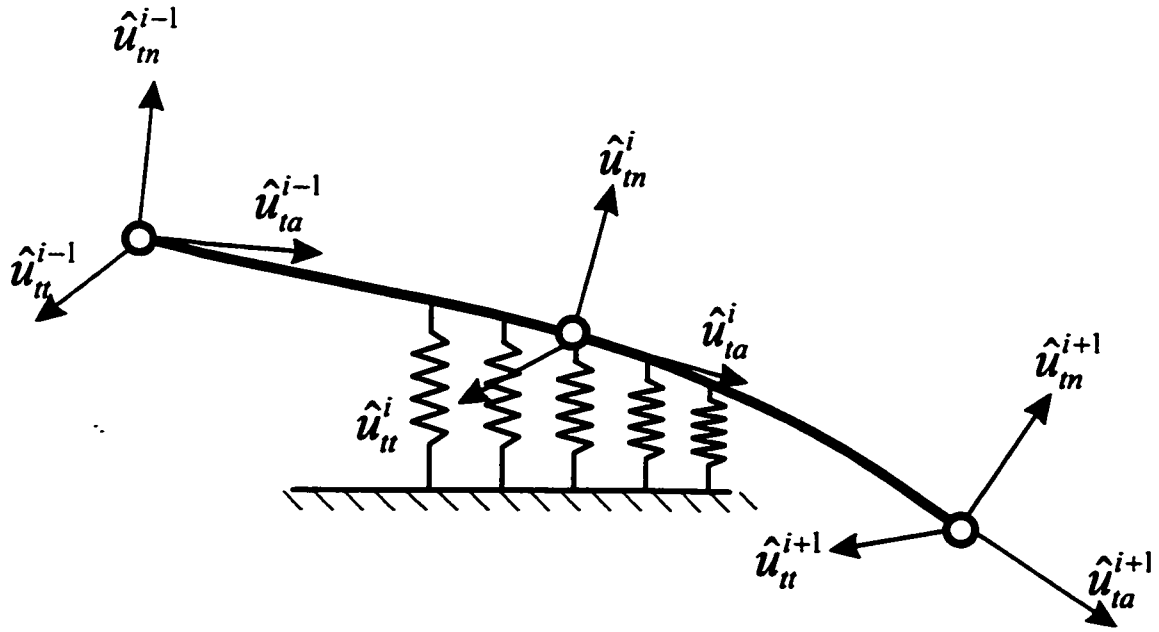

Figure 5.5 The segment contact model

$$U_s = \frac{K_g L_e}{2}\begin{pmatrix} (d_n^A)^2 H_1 + L d_n^A \theta_t^A H_2 + d_n^A d_n^E H_3 + L d_n^A \theta_t^E H_4 + d_n^A Cr H_5 + \\ L^2(\theta_t^A)^2 H_6 + L\theta_t^A d_n^E H_7 + L^2 \theta_t^A \theta_t^E H_8 + L\theta_t^A Cr H_9 + \\ (d_n^E)^2 H_{10} + L d_n^E \theta_t^E H_{11} + d_n^E Cr H_{12} + L^2(\theta_t^E)^2 H_{13} + \\ L\theta_t^E Cr H_{14} + (Cr)^2 H_{15} \end{pmatrix} \tag{5.27}$$

where H_1 to H_{15} are polynomials of the dimensionless contact segment (η):

$$\begin{aligned}
H_1 &= \frac{4}{7}\eta^7 - 2\eta^6 + \frac{9}{5}\eta^5 + \eta^4 - 2\eta^3 + \eta & H_2 &= \frac{4}{7}\eta^7 - \frac{7}{3}\eta^6 + \frac{16}{5}\eta^5 - \eta^4 - \frac{4}{3}\eta^3 + \eta^2 \\
H_3 &= -\frac{8}{7}\eta^7 + 4\eta^6 - \frac{18}{5}\eta^5 - \eta^4 + 2\eta^3 & H_4 &= \frac{4}{7}\eta^7 - \frac{5}{3}\eta^6 + \frac{6}{5}\eta^5 + \frac{1}{2}\eta^4 - \frac{2}{3}\eta^3 \\
H_5 &= -\eta^4 + 2\eta^3 - 2\eta & H_6 &= \frac{1}{7}\eta^7 - \frac{2}{3}\eta^6 + \frac{6}{5}\eta^5 - \eta^4 + \frac{1}{3}\eta^3 \\
H_7 &= -\frac{4}{7}\eta^7 + \frac{7}{3}\eta^6 - \frac{16}{5}\eta^5 + \frac{3}{2}\eta^4 & H_8 &= \frac{2}{7}\eta^7 - \eta^6 + \frac{6}{5}\eta^5 - \eta^4 \\
H_9 &= -\frac{1}{2}\eta^4 + \frac{4}{3}\eta^3 - \eta^2 & H_{10} &= \frac{4}{7}\eta^7 - 2\eta^6 + \frac{9}{5}\eta^5 \\
H_{11} &= -\frac{4}{7}\eta^7 - \frac{5}{3}\eta^6 - \frac{6}{5}\eta^5 & H_{12} &= \eta^4 - 2\eta^3 \\
H_{13} &= \frac{1}{7}\eta^7 - \frac{1}{3}\eta^6 + \frac{1}{5}\eta^5 & H_{14} &= -\frac{1}{2}\eta^4 + \frac{2}{3}\eta^6 \\
H_{15} &= \eta
\end{aligned} \tag{5.28}$$

Now the nodal forces can be obtained by differentiating the strain energy expression with respect to the nodal degrees of freedom:

$$\begin{aligned}
\frac{\partial U_s}{\partial d_n^A} &= \frac{K_g L_e}{2}\left[2d_n^A H_1 + L_e \theta_t^A H_2 + d_n^E H_3 + L_e \theta_t^E H_4 + Cr H_5\right] \\
\frac{\partial U_s}{\partial \theta_n^A} &= \frac{K_g L_e}{2}\left[L_e d_n^A H_2 + 2L_e^2 \theta_t^A H_6 + L_e d_n^E H_7 + L_e^2 \theta_t^E H_8 + L_e Cr H_9\right] \\
\frac{\partial U_s}{\partial d_n^E} &= \frac{K_g L_e}{2}\left[d_n^A H_3 + L_e \theta_t^A H_7 + 2d_n^E H_{10} + L_e \theta_t^E H_{11} + Cr H_{12}\right] \\
\frac{\partial U_s}{\partial \theta_n^E} &= \frac{K_g L_e}{2}\left[L_e d_n^A H_4 + L_e^2 \theta_t^A H_8 + L_e d_n^E H_{11} + L_e^2 \theta_t^E H_{13} + L_e Cr H_{14}\right]
\end{aligned} \tag{5.29}$$

Rearranging Equation (5.29) in the matrix form:

$$[P]_{spr} = \begin{Bmatrix} F_n^A \\ M_t^A \\ F_n^E \\ M_t^E \end{Bmatrix} = \frac{K_g L_e}{2} \begin{bmatrix} 2H_1 & L_e H_2 & H_3 & L_e H_4 & H_5 \\ L_e H_2 & 2L_e^2 H_6 & L_e H_7 & L_e^2 H_8 & LH_9 \\ H_3 & L_e H_7 & 2H_{10} & L_e H_{11} & H_{12} \\ L_e H_4 & L_e^2 H_8 & L_e H_{11} & 2L_e^2 H_{13} & LH_{14} \end{bmatrix} \begin{Bmatrix} d_n^A \\ \theta_t^A \\ d_n^E \\ \theta_t^E \\ Cr \end{Bmatrix} \tag{5.30}$$

The total spring force is obtained by integrating the contact pressure along the contact segment.

$$F_{spr} = L_e K_g \int_0^{\eta} \left(d_n(\zeta) - Cr \right) d\zeta \tag{5.31}$$

By carrying out the above integration and rearranging the resultant expression:

$$F_{spr} = K_g L_e \begin{Bmatrix} d_n^A & L_e \theta_t^A & d_n^E & L_e \theta_t^E & Cr \end{Bmatrix} \begin{Bmatrix} H_1 \\ H_2 \\ H_3 \\ H_4 \\ H_5 \end{Bmatrix} \tag{5.32}$$

where

$$\begin{aligned} H_1 &= \frac{1}{2}\eta^4 - \eta^3 + \eta \quad H_2 = \frac{1}{4}\eta^4 - \frac{2}{3}\eta^3 + \frac{1}{2}\eta \\ H_3 &= -\frac{1}{2}\eta^4 + \eta^3 \quad H_4 = \frac{1}{4}\eta^4 - \frac{1}{3}\eta^3 \\ H_5 &= -\eta \end{aligned} \tag{5.33}$$

The damping force due to the impact can be calculated using Equation(3.10) which can use the average velocity along the segment contact. Now, the consistent load vector due to the damping force is calculated by considering that the damping force to be equally distributed along the contact segment. The resulting pressure due to the impact damping force is

represented by:

$$p_{dmp} = \frac{F_{dmp}}{b} \tag{5.34}$$

where b is the contact segment length. Now considering the work rate due to these forces:

$$W_{dmp} = L_e \int_0^{\eta} p(\zeta)\left(d_n(\zeta) - Cr\right)d\zeta \tag{5.35}$$

By carrying out the integration, Equation (3.35) becomes:

$$W_{dmp} = p_{dmp} L\left\{d_n^A \quad \theta_t^A \quad d_n^E \quad \theta_t^E \quad Cr\right\}\begin{Bmatrix} H_1 \\ LH_2 \\ H_3 \\ LH_4 \\ H_5 \end{Bmatrix} = \left\{d_n\right\}\{P\} \tag{5.36}$$

The consistent load vector due to the support damping forces is therefore:

$$[P]_{dmp} = p_{dmp} L\left\{H_1 \quad LH_2 \quad H_3 \quad LH_4\right\}^T \tag{5.37}$$

Now the consistent load vector due to impact forces is expressed as:

$$[P]_{imp} = [P]_{spr} + [P]_{dmp} \tag{5.38}$$

The consistent load vector representing the friction force due to the relative motion between the tube and its support is obtained by considering the dissipated energy. The work done by the friction forces in the axial direction is expressed as:

$$W_{fa} = R_a K_g L_e \int_0^{\eta} \left(d_n(\zeta) - Cr\right) d_a(\zeta) d\zeta \tag{5.39}$$

where R_a is a proportionality factor which depends on the friction coefficient and the sliding velocity, therefore:

$$\begin{aligned} R_a &= -\frac{\mu_s V_r}{V_o}\left(\hat{u}_{tr} \cdot \hat{u}_{ta}\right) && \text{if } V_r < V_o \\ &= -\mu_d\left(\hat{u}_{tr} \cdot \hat{u}_{ta}\right) && \text{if } V_r \geq V_o \end{aligned} \tag{5.40}$$

By carrying out the integration of Equation (5.39) and rearranging the resultant equation in matrix form:

$$\begin{aligned} W_{fa} &= R_a K_g L_e \left\{d_a^A \quad d_a^E\right\} \begin{bmatrix} H_{11} & H_{12} & H_{13} & H_{14} & H_{15} \\ H_{21} & H_{22} & H_{23} & H_{24} & H_{25} \end{bmatrix} \begin{Bmatrix} d_n^A \\ L_e\theta_t^A \\ d_n^E \\ L_e\theta_t^E \\ Cr \end{Bmatrix} \\ &= \left\{d_a\right\}\left\{P_{fa}\right\} \end{aligned} \tag{5.41}$$

Hence the consistent the load vector due to the axial component of the friction forces is:

$$\left\{P_{fa}\right\} = R_a K_g L \begin{bmatrix} H_{11} & H_{12} & H_{13} & H_{14} & H_{15} \\ H_{21} & H_{22} & H_{23} & H_{24} & H_{25} \end{bmatrix} \begin{Bmatrix} d_n^A \\ L_e\theta_t^A \\ d_n^E \\ L_e\theta_t^E \\ Cr \end{Bmatrix} \tag{5.42}$$

where

$$H_{11} = -\frac{2}{5}\eta^5 = \frac{5}{4}\eta^4 - \eta^3 - \frac{1}{2}\eta^2 + \eta \quad H_{12} = -\frac{1}{5}\eta^5 + \frac{3}{4}\eta^4 - \eta^3 + \frac{1}{2}\eta^2$$
$$H_{13} = \frac{2}{5}\eta^5 - \frac{5}{4}\eta^4 + \eta^3 \qquad H_{14} = -\frac{1}{5}\eta^5 + \frac{1}{2}\eta^4 - \frac{1}{3}\eta^3$$
$$H_{15} = \frac{1}{2}\eta^2 - \eta \qquad H_{21} = \frac{2}{5}\eta^5 - \frac{3}{4}\eta^4 + \frac{1}{2}\eta^2 \qquad (5.43)$$
$$H_{22} = \frac{1}{5}\eta^5 - \frac{1}{2}\eta^4 - \frac{1}{3}\eta^3 \qquad H_{23} = -\frac{2}{5}\eta^5 - \frac{3}{4}\eta^4$$
$$H_{24} = \frac{1}{5}\eta^5 - \frac{1}{4}\eta^4 \qquad H_{25} = -\frac{1}{5}\eta^2$$

Similarly, the work expression for the tangential friction force is given by the following integral:

$$W_{ft} = R_t K_g L_e \int_0^{\eta} \left(d_n(\zeta) - Cr\right) d_t(\zeta) d\zeta \qquad (5.44)$$

where R_t is a proportionality factor which depends on the friction coefficient and the sliding velocity.

$$\begin{aligned} R_t &= -\frac{\mu_s V_r}{V_o}\left(\hat{u}_{tr} \cdot \hat{u}_{tt}\right) && \text{if } V_r < V_o \\ &= -\mu_d\left(\hat{u}_{tr} \cdot \hat{u}_{tt}\right) && \text{if } V_r \geq V_o \end{aligned} \qquad (5.45)$$

The integration of Equation (5.44) is carried out and the resultant expression is rearranged in matrix form as follows:

$$W_{ft} = -R_t K_g L_e \left\{ d_t^A \quad \theta_n^A \quad d_t^E \quad \theta_n^E \right\} \begin{bmatrix} H_{11} & H_{12} & H_{13} & H_{14} & H_{15} \\ H_{21} & H_{22} & H_{23} & H_{24} & H_{25} \\ H_{31} & H_{32} & H_{33} & H_{34} & H_{35} \\ H_{41} & H_{42} & H_{43} & H_{44} & H_{45} \end{bmatrix} \begin{Bmatrix} d_n^A \\ L_e\theta_t^A \\ d_n^E \\ L_e\theta_t^E \\ Cr \end{Bmatrix} \qquad (5.46)$$

$$= \left\{d_t\right\}\left\{P_{ft}\right\}$$

Hence the consistent load vector due to the axial component of the friction forces is:

$$\left\{P_{fi}\right\} = R_t K_g L_e \begin{bmatrix} H_{11} & H_{12} & H_{13} & H_{14} & H_{15} \\ H_{21} & H_{22} & H_{23} & H_{24} & H_{25} \\ H_{31} & H_{32} & H_{33} & H_{34} & H_{35} \\ H_{41} & H_{42} & H_{43} & H_{44} & H_{45} \end{bmatrix} \begin{Bmatrix} d_n^A \\ L_e\theta_t^A \\ d_n^E \\ L_e\theta_t^E \\ Cr \end{Bmatrix} \tag{5.47}$$

where

$$H_{11} = \frac{4}{7}\eta^7 - 2\eta^6 + \frac{9}{5}\eta^5 + \eta^4 - 2\eta^3 + \eta \qquad H_{12} = -\frac{4}{7}\eta^7 - 2\eta^6 + \frac{9}{5}\eta^5 - \frac{1}{2}\eta^4 - \eta^3$$

$$H_{13} = \frac{2}{7}\eta^7 - \frac{7}{6}\eta^6 + \frac{8}{5}\eta^5 - \frac{1}{2}\eta^4 - \frac{2}{3}\eta^3 + \frac{1}{2}\eta^2 \qquad H_{14} = \frac{2}{7}\eta^7 - \frac{5}{6}\eta^6 + \frac{3}{5}\eta^5 + \frac{1}{4}\eta^4 - \frac{1}{3}\eta^3$$

$$H_{15} = -\frac{1}{2}\eta^4 + \eta^3 - \eta \qquad H_{21} = -\frac{2}{7}\eta^7 + \frac{7}{6}\eta^6 - \frac{8}{5}\eta^5 + \frac{1}{2}\eta^4 + \frac{2}{3}\eta^3 - \frac{1}{2}\eta^2$$

$$H_{22} = -\frac{1}{7}\eta^7 + \frac{2}{3}\eta^6 - \frac{6}{5}\eta^5 + \eta^4 - \frac{1}{2}\eta^3 \qquad H_{23} = \frac{2}{7}\eta^7 - \frac{7}{6}\eta^6 + \frac{8}{5}\eta^5 - \frac{3}{4}\eta^4$$

$$H_{24} = -\frac{1}{7}\eta^7 + \frac{1}{2}\eta^6 - \frac{3}{5}\eta^5 + \frac{1}{4}\eta^4 \qquad H_{25} = \frac{1}{4}\eta^4 - \frac{2}{3}\eta^3 + \frac{1}{2}\eta^2$$

$$H_{31} = -\frac{4}{7}\eta^7 - 2\eta^6 - \frac{9}{5}\eta^5 - \frac{1}{2}\eta^4 + \eta \qquad H_{32} = -\frac{2}{7}\eta^7 + \frac{7}{6}\eta^6 - \frac{8}{5}\eta^5 + \frac{3}{4}\eta^4 \tag{5.48}$$

$$H_{33} = \frac{4}{7}\eta^7 - 2\eta^6 + \frac{9}{5}\eta^5 \qquad H_{34} = -\frac{2}{7}\eta^7 + \frac{5}{6}\eta^6 - \frac{3}{5}\eta^5$$

$$H_{35} = \frac{1}{2}\eta^4 - \eta^3 \qquad H_{41} = -\frac{2}{7}\eta^7 + \frac{5}{6}\eta^6 - \frac{3}{5}\eta^5 - \frac{1}{4}\eta^4 - \frac{1}{3}\eta^3$$

$$H_{42} = -\frac{1}{7}\eta^7 + \frac{1}{2}\eta^6 - \frac{3}{5}\eta^5 + \frac{1}{4}\eta^4 \qquad H_{43} = -\frac{2}{7}\eta^7 - \frac{5}{6}\eta^6 + \frac{3}{5}\eta^5$$

$$H_{44} = -\frac{1}{7}\eta^7 + \frac{1}{3}\eta^6 - \frac{1}{5}\eta^5 \qquad H_{45} = \frac{1}{4}\eta^4 - \frac{1}{3}\eta^6$$

The normal work rate defined by Equation (4.2) can be rewritten in terms of its tangential and axial components as:

$$\dot{W}_t = L_e K_g \int_0^{\eta} \left(d_n(\zeta) - Cr\right)\dot{d}_t(\zeta)\,d\zeta \tag{5.49}$$

$$\dot{W}_a = L_e K_g \int_0^{\eta} \left(d_n(\zeta) - Cr\right)\dot{d}_a(\zeta)\,d\zeta \tag{5.50}$$

By carrying out the integration and rearranging the terms, the work rate expression yields the following equation:

$$\dot{W}_t = K_g L_e \left\{\dot{d}_t^A \quad \dot{\theta}_n^A \quad \dot{d}_t^E \quad \dot{\theta}_n^E\right\} \begin{bmatrix} H_{11} & H_{12} & H_{13} & H_{14} & H_{15} \\ H_{21} & H_{22} & H_{23} & H_{24} & H_{25} \\ H_{31} & H_{32} & H_{33} & H_{34} & H_{35} \\ H_{41} & H_{42} & H_{43} & H_{44} & H_{45} \end{bmatrix} \begin{Bmatrix} d_n^A \\ L_e\theta_t^A \\ d_n^E \\ L_e\theta_t^E \\ Cr \end{Bmatrix} \tag{5.51}$$

$$\dot{W}_a = K_g L_e \left\{\dot{d}_a^A \quad \dot{d}_a^E\right\} \begin{bmatrix} H_{11} & H_{12} & H_{13} & H_{14} & H_{15} \\ H_{21} & H_{22} & H_{23} & H_{24} & H_{25} \end{bmatrix} \begin{Bmatrix} d_n^A \\ L_e\theta_t^A \\ d_n^E \\ L_e\theta_t^E \\ Cr \end{Bmatrix} \tag{5.52}$$

Now, the equivalent work rate is obtained by:

$$\dot{W} = \left(\dot{W}_a^2 + \dot{W}_t^2\right)^{\frac{1}{2}} \tag{5.53}$$

5. 4 NUMERICAL SIMULATIONS

5. 4. 1 CANTILEVER TUBE

The enhanced tube/support interaction model is used to investigate the effect of the support width on the tube dynamics. In this analysis, the tube model used in Section 4.3 (configuration # 3) is utilized. The support is placed at the 30th node (at 0.021 m from the tip of the tube). Four support width values are used:10, 15, 20, and 25 mm. The tube is subjected to a flow of air at density of 1.18 kg/m^3 at a velocity of 8 m/s. The fluid forces due to turbulence are distributed over the entire tube length. Using the enhanced tube/support model, both segment and point contact are identified. The tube support interaction parameters, including the RMS impact forces, the contact ratio and the normal work rate, are calculated for both the segment and the point contact situations.

5. 4. 1. 1 DETERMINATION OF THE CONTACT STIFFNESS

In the case of point contact, the value of the equivalent point contact stiffness, as indicated in the literature (Axisa *et al.*, 1988), is in the range of 10^6 to 10^7 N/m. The value of the distributed contact stiffness is needed for the model developed here. Therefore, a detailed finite element modelling of the tube-support contact was conducted. Figure 5.6a shows a tube/flat bar assembly in which the flat bar is supporting many tubes on either side. To analyse the tube/support stiffness, the tube support assembly is reduced to a single tube contacting the flat bar. In addition, only a small portion of the flat bar is considered. The length of this portion corresponds to the tube array pitch (The distance between two successive tubes). The tube support model is shown in Figure 5.6b A tube of a 15.88 mm

outer diameter is considered and is discretized by means of 3-D solid tetrahedron elements. The support is assumed to be 25 mm wide, 40 mm long, and 5 mm thick. A distributed load of 1 N/mm is applied at the top of the tube. Two simulations considering two flat support boundary conditions; simply supported and clamped at either side, were carried out. For both boundary conditions cases, the tube deformation was restrained against lateral motion.

Figure 5.7 shows the deformation distribution of the tube/support assembly for the case of the simply supported flat bar. The tube deformation and the corresponding equivalent contact stiffness per unit support length for the two flat bar end conditions are shown in Table 5.1. The tube deformation is calculated at the plane passing the centre of the tube and parallel to the support surface. The distributed contact stiffness can be inferred by dividing the applied distributed load by the average tube deformation.

Table 5.1 Tube/support contact stiffness for two flat bar boundary conditions

Flat-bar end conditions	Average tube deformation [m]	Stiffness per unit support width [(N/m)/m]
Simply supported	2.036×10^{-6}	2.036×10^{8}
Clamped	2.155×10^{-6}	2.155×10^{8}

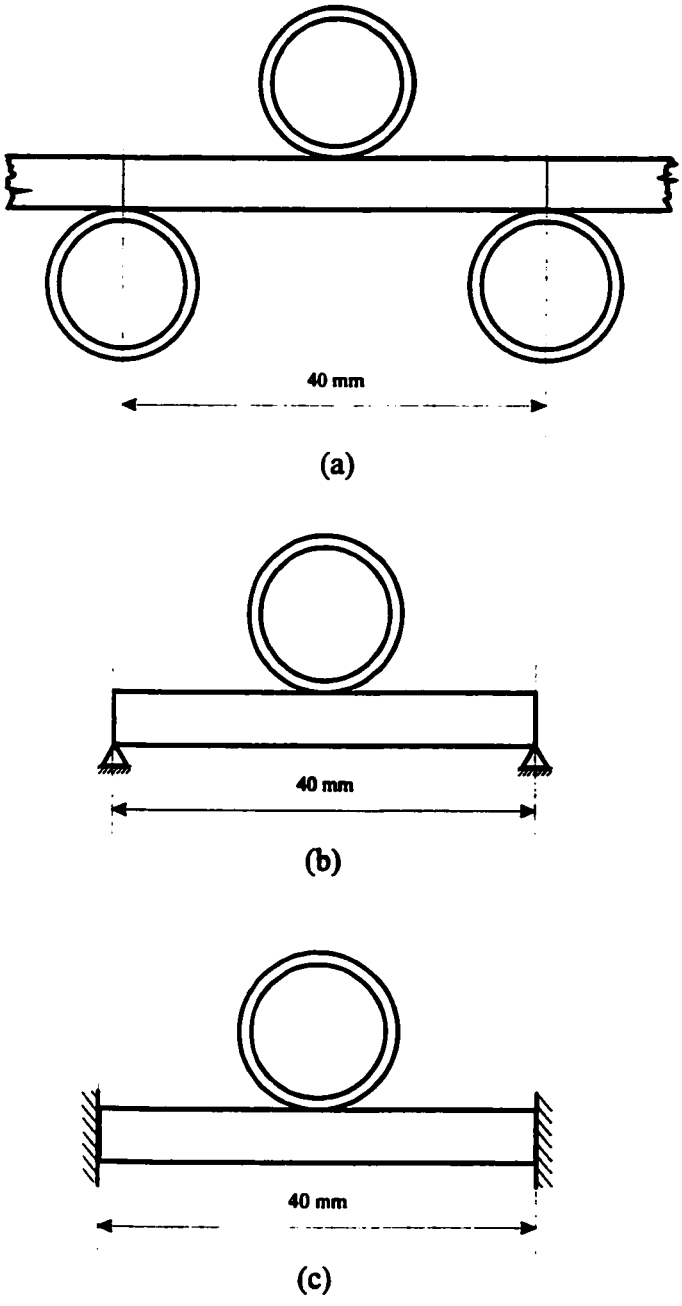

Figure 5.6 Tube/support modelling. a) heat exchanger tube/support assembly. b) a tube/support model including a simply-supported flat bar. c) a tube/support model including a fixed-end flat bar.

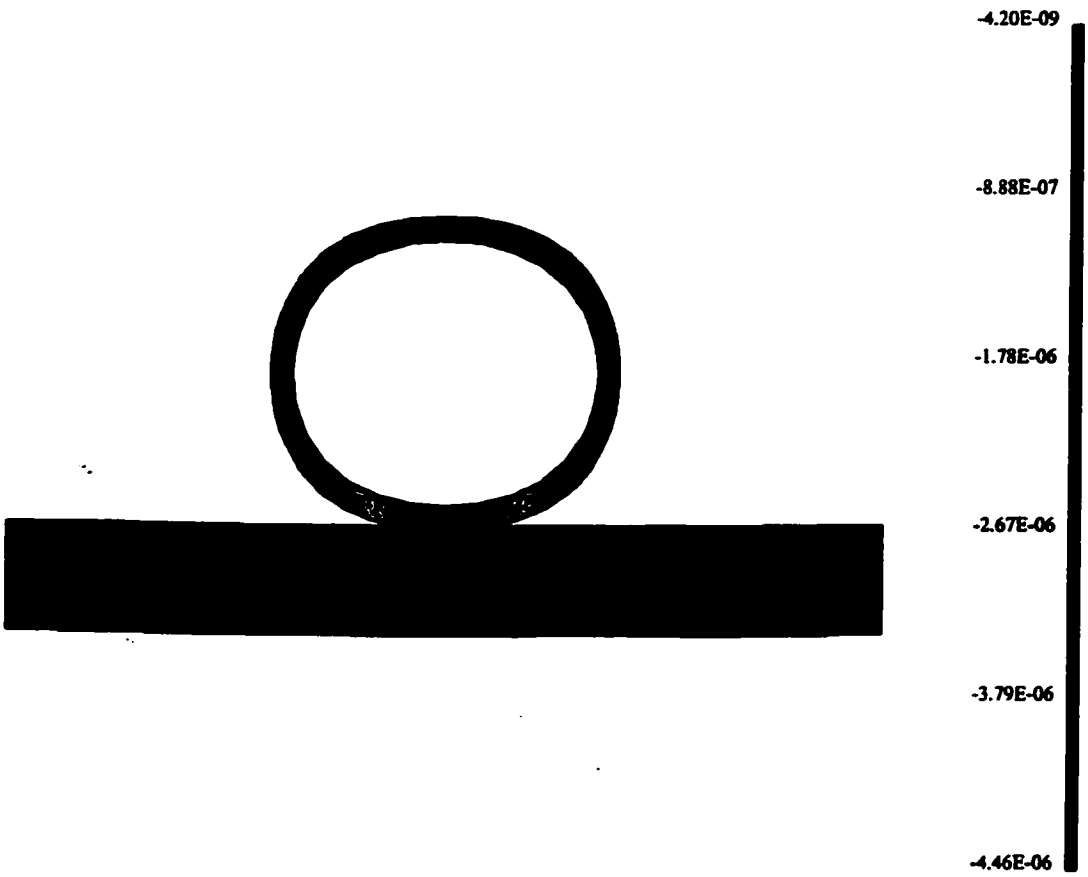

Figure 5.7 The deformation distribution of the tube/support assembly

5. 4. 1. 2 EFFECT OF THE CONTACT STIFFNESS

In order to investigate the sensitivity of the tube/support interaction parameters to the value of the segmental contact stiffness, a support width of 25 mm is considered. The segmental stiffness values vary within a range of $1x10^8$ to $5x10^8$ N/m^2. Figures 5.8 to 5.10 show the effect of the segmental stiffness on the RMS impact force, the contact ratio, and the normal work rate, respectively. Increasing the segmental stiffness does not have a significant effect on either RMS impact force or the contact ratio. If the segmental stiffness is increased by 500%, the RMS impact force increases by a mere 3.7%, while the contact ratio decreases by 2%. On the other hand, the normal work rate decreases as the segmental stiffness increases (Figure 5.10). When the segmental stiffness is increased beyond $3x10^8$ N/m^2, the work rate levels off. This is attributed to the fact that as the contact stiffness increases the normal contact force becomes larger and in turn, the friction capacity increases. Therefore, a higher resistance to the tube sliding motion develops. Using the estimated support stiffness from Section (5.4.1.1) will therefore give a reasonable estimate of both the RMS impact force and the contact ratio, while providing a conservative estimate of the normal work rate.

5. 4. 1. 3 EFFECT OF THE SUPPORT WIDTH

The RMS impact force of the segment contact for various support width values is shown in Figure 5.11. An similar behaviour can be observed for all support width values. The RMS impact force decreases approximately linearly as the dimensionless clearance increases. This is followed by a sharper decrease in the RMS impact force. For a small range of dimensionless clearances (0 to approximately 0.16), a higher RMS impact force

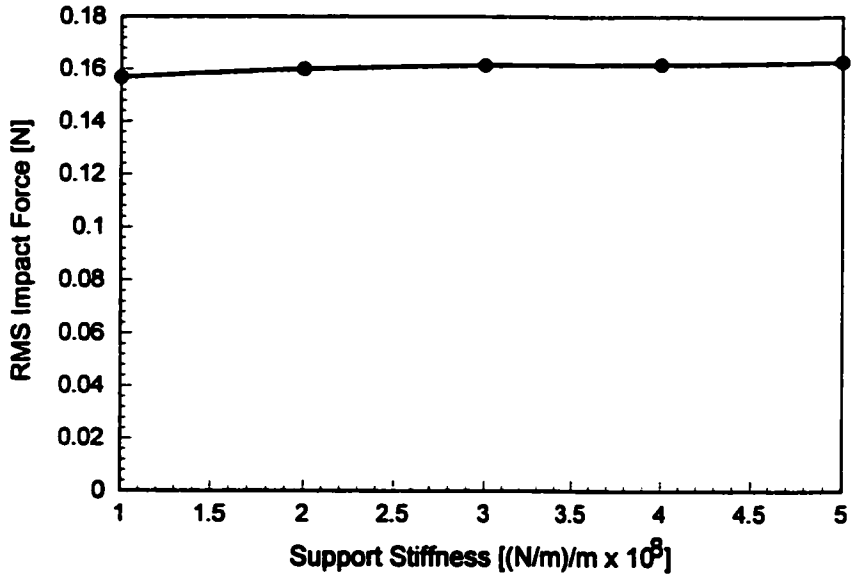

Figure 5.8 Effect of the segmental stiffness on the RMS impact force

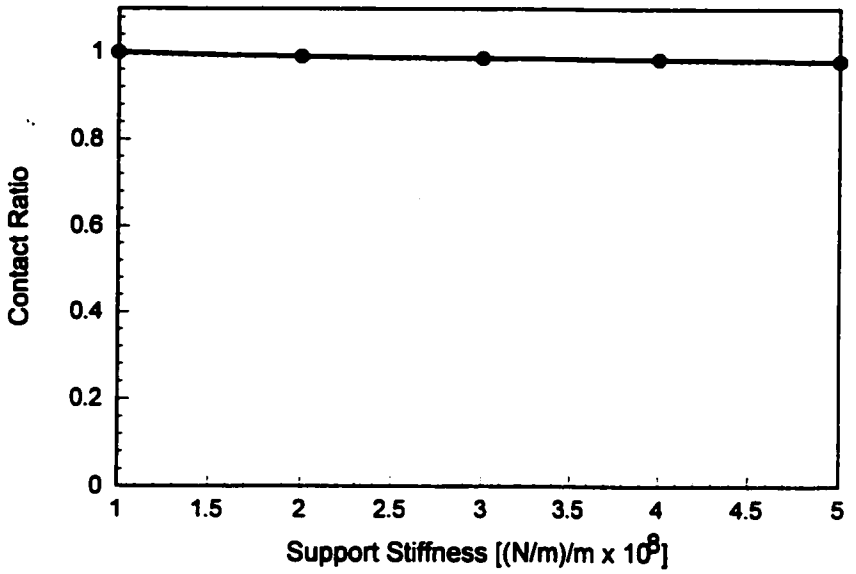

Figure 5.9 Effect of the segmental stiffness on the contact ratio

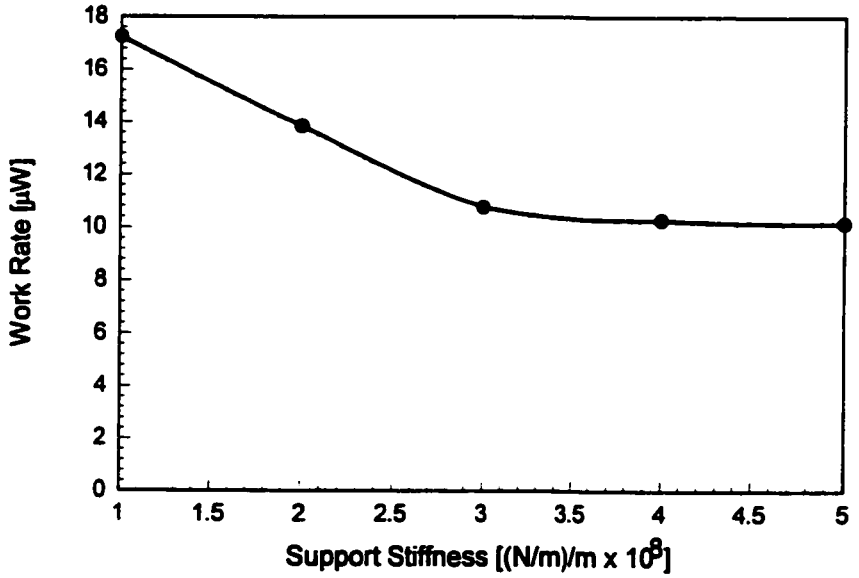

Figure 5.10 Effect of the segmental stiffness on the normal work rate

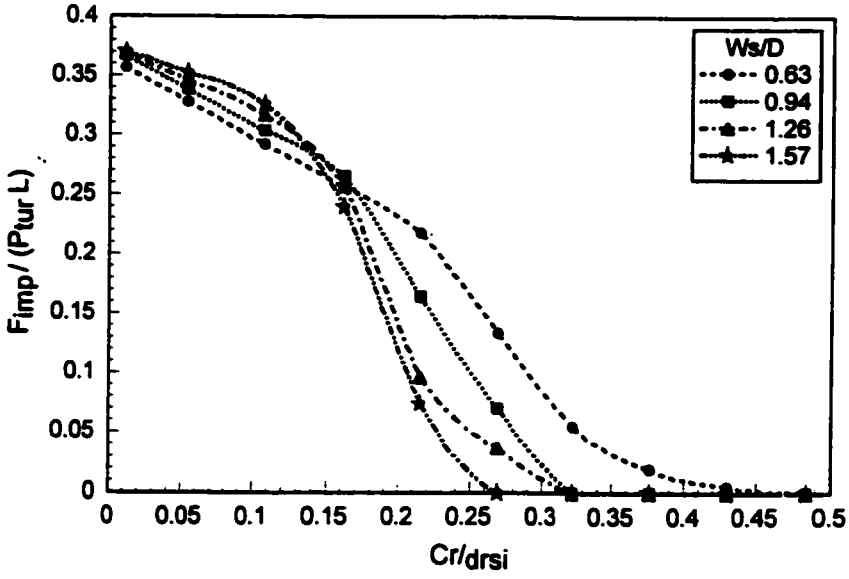

Figure 5.11 Dimensionless RMS impact force (segment contact)

results when the support width is increased. As the support width decreases and the dimensionless clearance increases beyond about 0.16, the segment contact force decreases to zero since the contact tends to be a point-like contact.

Figure 5.12 depicts the dimensionless RMS impact force resulting from the tube/support point (edge) contact for various support width values. For a given support width, the dimensionless impact force is zero when the dimensionless clearance is zero. Increasing the dimensionless clearance gradually increases the point impact force. This behaviour is maintained up to a certain dimensionless clearance at which the impact force starts to decrease linearly. At this point the solution is similar to the situation of a zero-width support (using the conventional tube/support model) in which only point contact exists. This is true since enlarging the dimensionless clearance permits the tube to impact with the support at the support edge. This results in essentially a point contact situation. On the other hand, at a small clearance the contact configuration is mainly of the segmental type. This is because the tube deformation profile in the neighbourhood of the support is more uniform when the support clearance is small. This leads to a better alignment of the tube with the support and hence a segmental contact is promoted. As the width increases, the resulting impact force due to the point contact becomes larger. Moreover, the value of the dimensionless clearance, at which the solution is similar to the case of a zero-width support, is larger for smaller support width values.

The equivalent dimensionless impact force (EDIF) which is the sum of the point and segment contact forces of one of the support pairs is shown in Figure 5.13. In general, a higher support width yields a slightly higher EDIF for the dimensionless clearances ranging

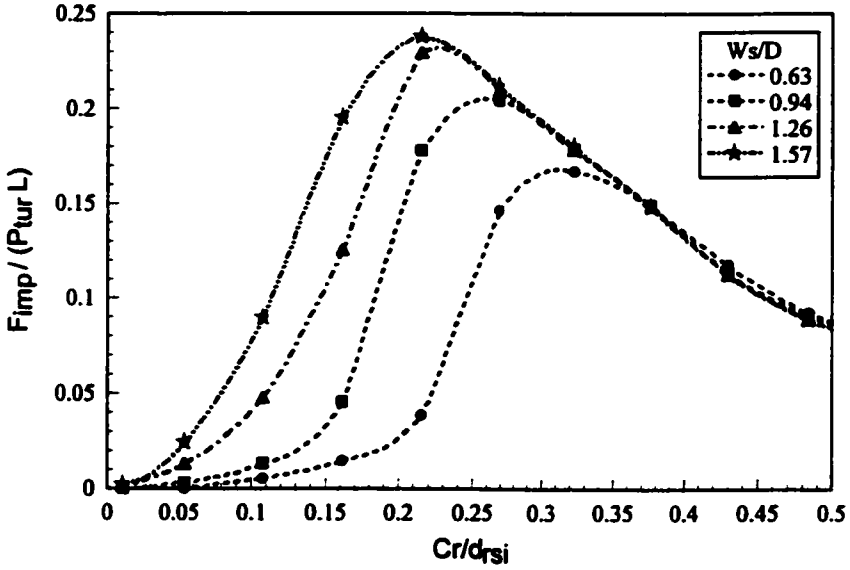

Figure 5.12 Dimensionless RMS impact force (point contact)

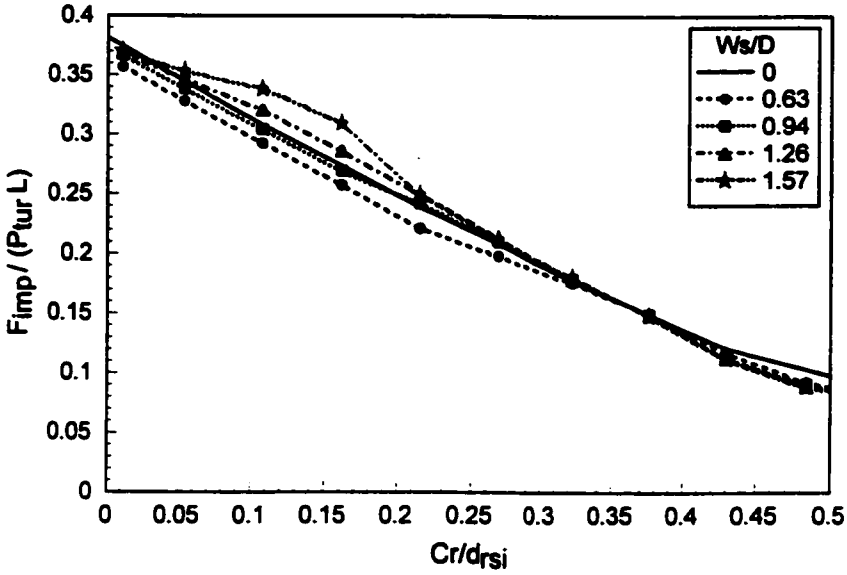

Figure 5.13 Dimensionless RMS impact force (equivalent contact)

from 0 to approximately 0.3. As the dimensionless clearance increases further, solutions for all support width values converge to the solution of the zero-width support. This is attributed to the nature of the tube support contact where at larger clearances, the tube contacts the support through a point rather than a segment.

Figure 5.14 shows the contact ratio due to segment contact as a function of the dimensionless clearance. As expected, for all support width values, the tube has 100% segment contact with the support at very small clearances. For a small support width, the tube continues to maintain a high segment-type of contact with the support for a range of dimensionless clearances. The range of dimensionless clearances permitting continuous segment contact decreases as the support width increases. Similar to the single-point contact model results, a sharp decrease in the contact ratio is observed when the clearance increases beyond a certain value. It then levels off asymptotically to zero as point contact is established. For a given dimensionless clearance, the segment contact ratio increases as the support width decreases, the higher the support width, the lower the dimensionless clearance at which the tube does not maintain a segment contact with the support.

The contact ratio of the tube with the support through the point-type contact is depicted in Figure 5.15 for various support width values. As mentioned earlier, in this model point contact is only possible between the tube and the edge of the support. Since the smaller clearance promotes a segment type of contact, the point contact ratio is initially very low. For a very small range of low dimensionless clearances (depending on the support width), the point contact ratio increases gradually. Then, it increases sharply up to a certain dimensionless clearance. A further increase in the support clearance results in a decrease in

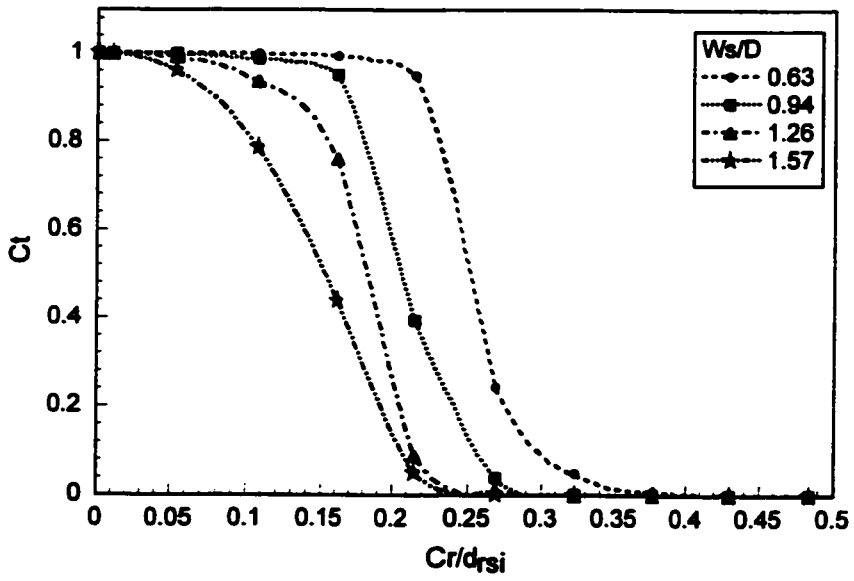

Figure 5.14 Contact ratio (segment contact)

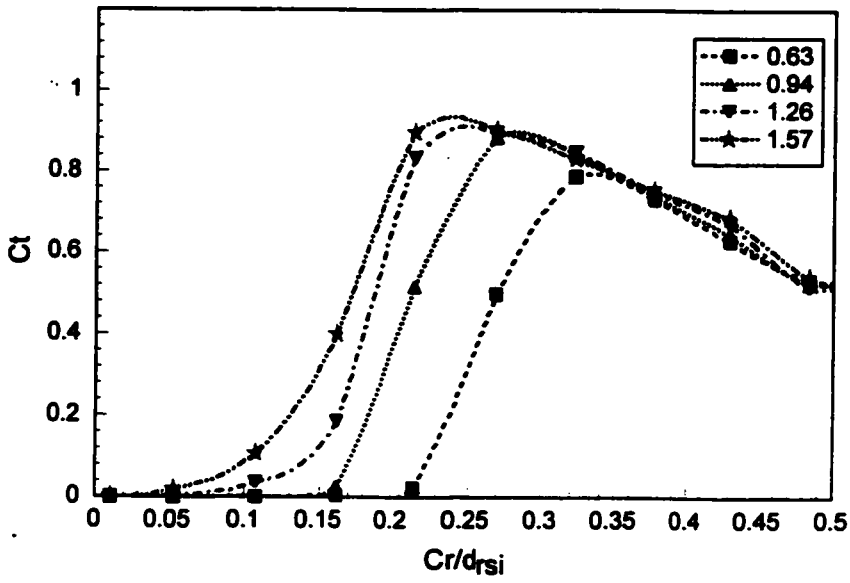

Figure 5.15 Contact ratio (point contact)

the contact ratio. It is interesting to note in Figure 5.15 that the point contact ratio solution does not converge to the solution of the single-point algorithm. This is attributed to the fact that the tube can be in a point-type of contact with either side of the support width.

The dimensionless work rate for the segment contact forces is shown in Figure 5.16. In the case of a tube with a dimensionless support width of 0.63, the work rate decreases linearly up to a dimensionless clearance of approximately 0.2. Then it decreases asymptotically to zero. For a higher support width, the work rate increases gradually to a certain dimensionless clearance, then decreases, the larger the support width, the higher the peak of the work rate. The normal work rate resulting from point contact sliding is shown in Figure 5.17. Similar to the normal work rate due to segment contact, the point contact work rate increases up to a certain dimensionless clearance, then decreases gradually. The maximum work rate is higher for a larger support width. Moreover, the smaller the support width, the higher the dimensionless clearance at which the work rate peak occurs. In addition, the normal work rate curves, due the point contact for all support width values, are similar to the results obtained by the conventional tube-support model.

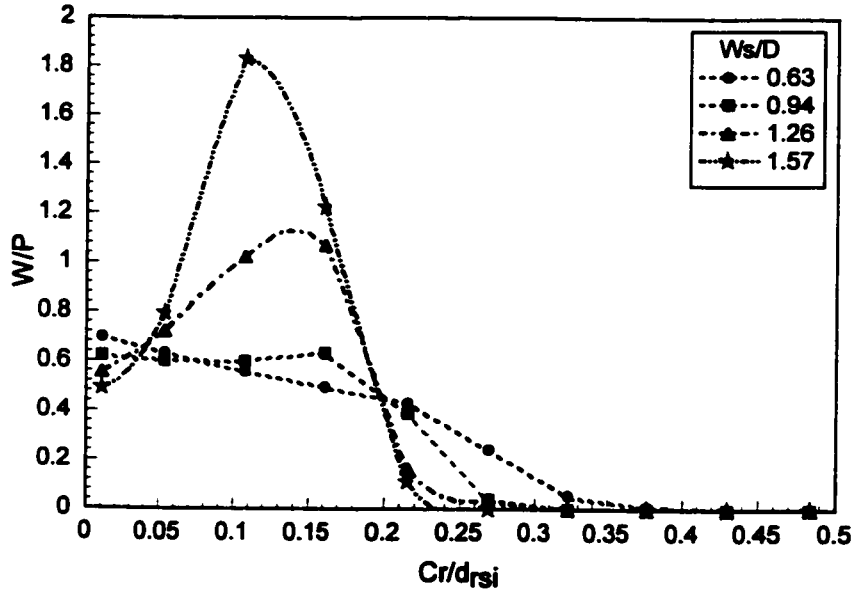

Figure 5.16 Dimensionless normal work rate (segment contact)

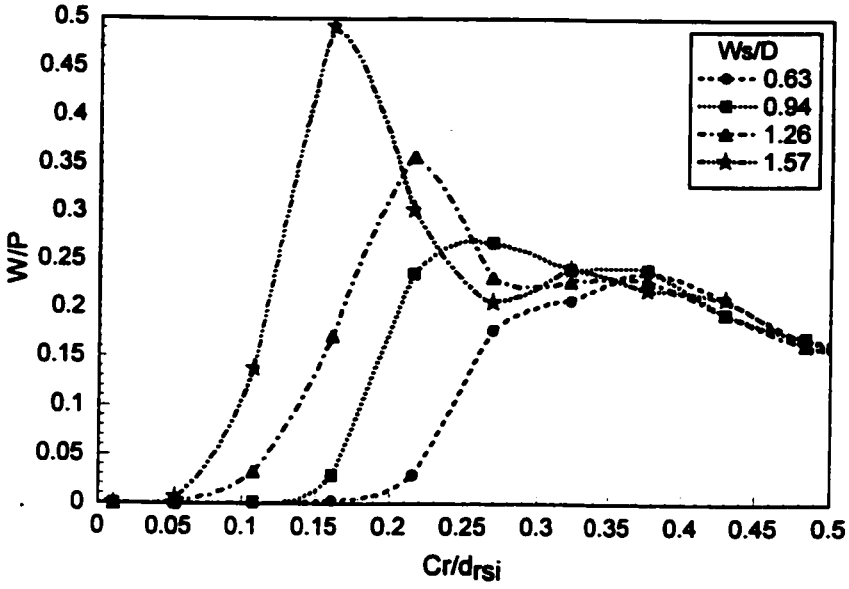

Figure 5.17 Dimensionless normal work rate (point contact)

5. 4. 2 TWO-SPAN TUBE

A two-span tube configuration was utilized in this section. This configuration consists of 1.19 m long tube fixed at both ends and loosely supported at the middle (Figure 5.18). The tube's material and cross section properties are identical to those of the cantilever tube model used in Section 5.4.1. The tube was excited by turbulence forces which are distributed along the entire length of the tube. The first unconstrained mode has an anti-node with a zero-slope at the support location as shown in Figure 5.18b This profile of the unconstrained mode provides a favourable condition for segmental contact rather than a point contact. Figure 5.19 depicts the effect of the dimensionless clearance on the dimensionless RMS impact force. It was found that the tube/support contact was only due to the segmental contact and no point contact was observed. Similar to the characteristic behaviour of the RMS impact forces described in Section 5.4.1, the RMS impact force decreases linearly as the dimensionless clearance increases up to a certain dimensionless clearance after which it decreases asymptotically to zero. This behaviour is observed for all support width values. It is evident that the RMS impact force increases when increasing the support width.

The dimensionless work rate for the segment contact forces is shown in Figure 5.20. For small dimensionless clearances (< 0.1), the dimensionless work rate decreases as the support width increases. For dimensionless width values of 0.63 and 0.94, the dimensionless work rate gradually deceases up to a dimensionless clearance of 0.4, then decreases more rapidly for a small range of dimensionless clearance values (0.4 to 0.6). Finally, the dimensionless normal work rate decreases asymptotically to zero. For dimensionless width values of 1.26 and 1.57, the work rate increases gradually up to a certain dimensionless

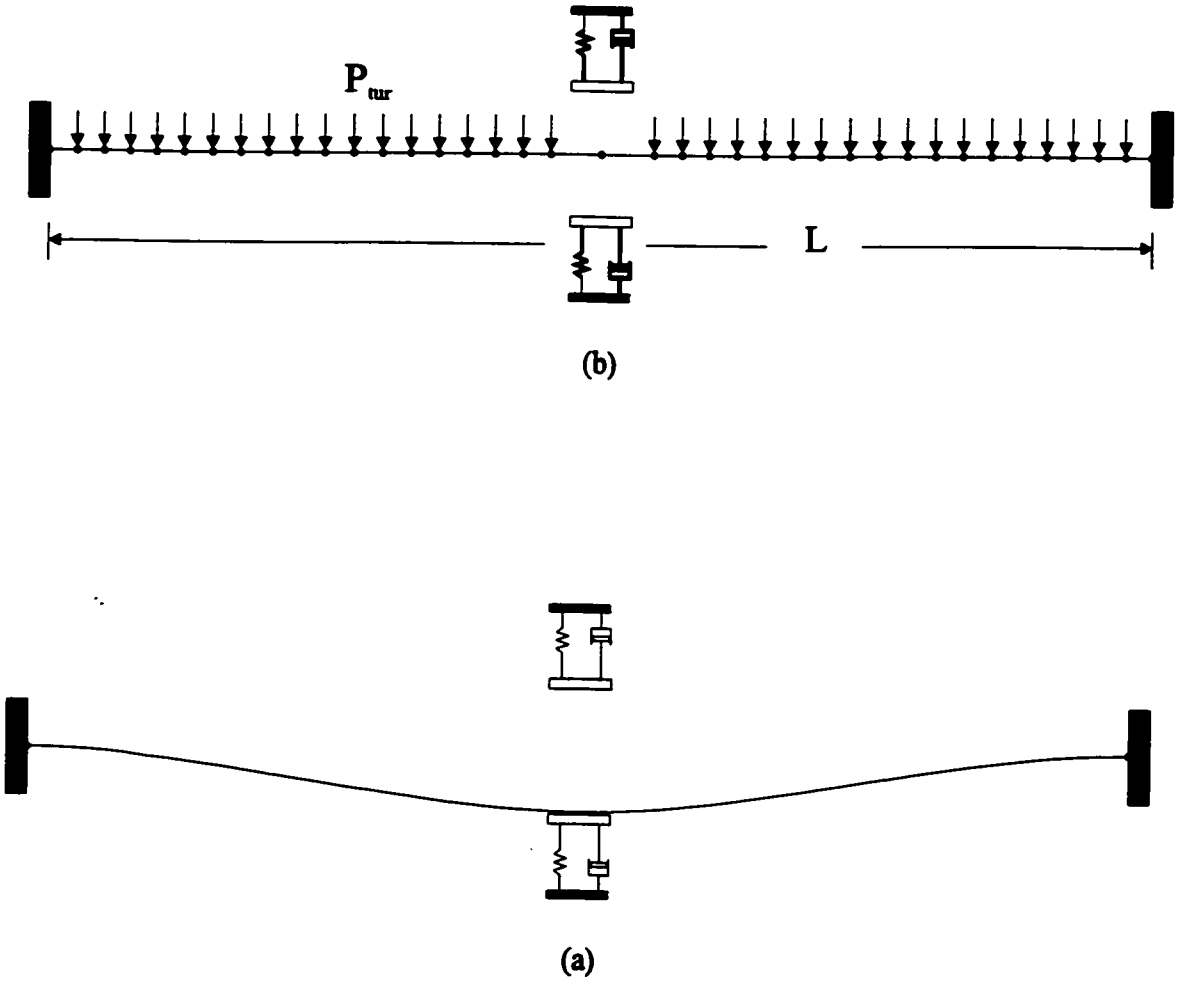

Figure 5.18 Two-span tube model with a loose support. a) tube/support finite element model. b) the first unconstrained mode shape.

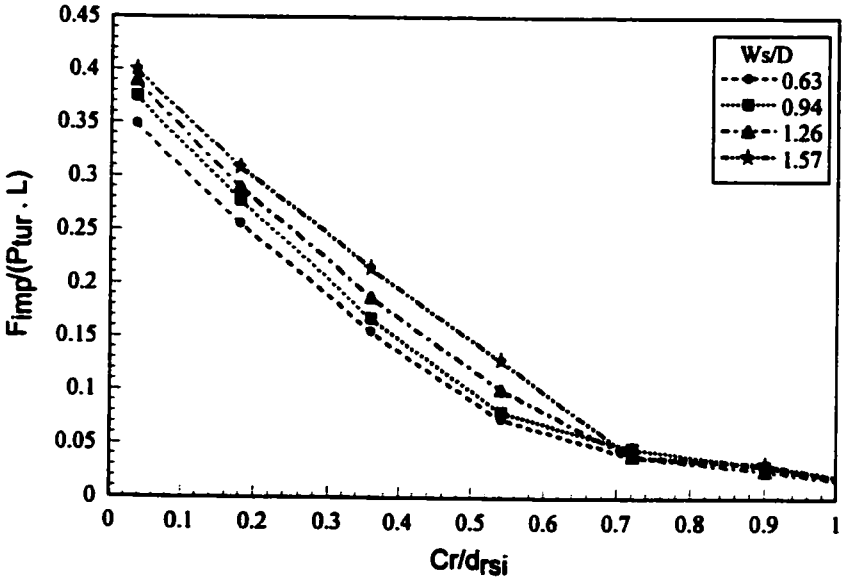

Figure 5.19 RMS impact force due to segmental contact

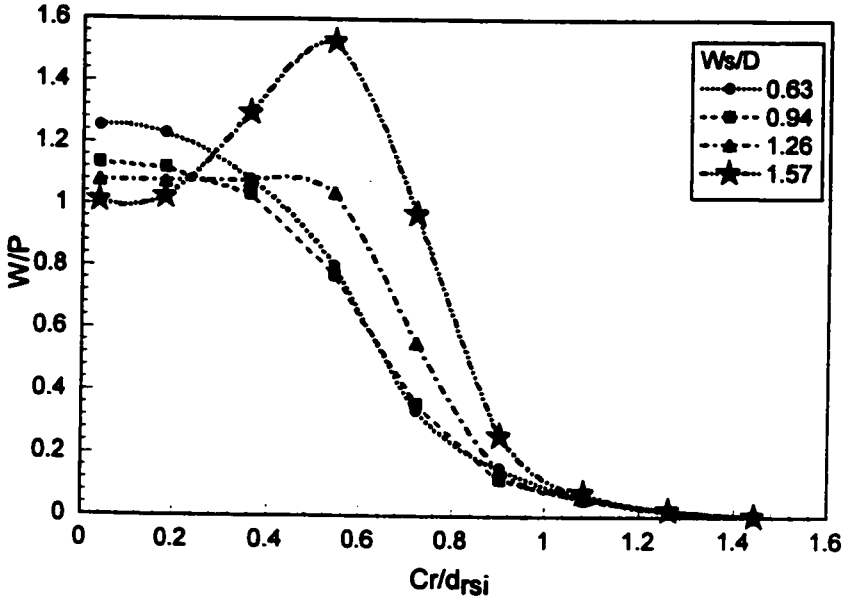

Figure 5.20 Dimensionless normal work rate due to segmental contact

clearance (0.6), then decreases sharply as the dimensionless clearance is further increased. The higher the support width, the higher the peak of the dimensionless work rate. In addition, the normal work rate curves, which are due to the segment contact for all support width values, converges to that of the zero-support width case for dimensionless clearance values larger than 0.7. This is attributed to the fact that by increasing the dimensionless clearance, the area of contact is reduced since less tube-support overlap is maintained. Finally, the overlap segment is reduced to a very small value, which makes all the work rate curves associated to the work rate converge to that of the zero-width type of contact.

5. 4. 3 COMMENTS ON THE WORK RATE RESULTS

Tube wear rate is affected by several factors including tube and support material combination, environmental conditions (temperature and water chemistry), tube to support relative motion and the support configuration (Fisher *et al.* 1995). The effect of the first and second factors are discussed in detail by Guérout and Fisher (1999). Tube-to-support relative motion is a major parameter affecting fretting wear rates. A tube within a heat exchanger may experience many different tube motions. Motion type may be classified as impact, sliding, and combined impact and sliding (Ko, 1997; Pettigrew *et al.* 1986). The existence of any of these motion types depends on the support geometry, the excitation level and the tube-to-support clearance. For example, when the preload is large enough to prevent tube support separation, tube motion is basically of the classical sliding type. On the other hand, when the clearance is large with a small preload, intermittent contact occurs. The tube/support contact configuration may change with the steam generator operating

conditions. Other classification categorizes the tube motion at the support location into two main types: rocking motion, and tube vibration with anti-nodes at the supports (Goyder 1982). Support configuration (geometry, clearance, width etc.) affects tube wear in two ways. Firstly, tube-to-support clearance combined with the level of support preload determines the type of tube/support relative motion as discussed earlier. Secondly, the wear rate is dependent on the contact configuration. As introduced in this chapter, tube/support contact is classified into two types: point contact and segment contact. The domination of any of these tube/support contact configuration is dictated by the tube motion and the support width. Tube/support contact may be a combination of both of these types. For example, the cantilever tube presented in Section 5.4.1.3 contacts the support over a segment for only a small range of clearances. As the clearance increases, the tube/support contact is a combination of segmental and point contact. On the other hand, tube/support interaction may occur through a segmental type of contact only. This was observed in the two-span tube example discussed in Section 5.4.2. In both of these examples, it was also shown that increasing the support width increases the segmental RMS impact force and the work rate. This segmental contact force is distributed over a larger area when the support width is increased. Therefore, their effect may be less damaging than the wear produced due to point contact. The contact pressure (impact force per unit support width) for various support width values is illustrated in Figures 5.21 and 5.22 for the cantilever and two-span tube cases respectively. The effective dimensionless contact pressure is calculated as follows:

$$F = \left(\frac{P_{imp}}{P_{tur}} \right) \tag{5.54}$$

where P_{tur} is the applied turbulence force per unit tube length and P_{imp} is the RMS segmental impact pressure which is calculated by:

$$P_{imp} = \left(\lim_{T \to \infty} \frac{1}{T} \int_0^T \frac{F_{imp}(t)}{b(t)} dt \right)^{\frac{1}{2}} \tag{5.55}$$

where $F_{imp}(t)$ and $b(t)$ are the instantaneous impact force and the segmental contact length respectively. As the support width increases, the impact force is distributed over a larger contact area leading to a smaller contact pressure. It is apparent that the contact pressure decreases as the support width increases. Contact pressure can have a great effect on the work rate. Greater wear rates were observed for smaller areas of contact (Fisher *et al.* 1995). This effect was attributed to the differences in the contact pressure (Lim and Ashby, 1987). Simplifying the tube-support structure to a single point contact seems to be a valid assumption when predicting the total RMS impact force. However, since the details of the tube motion, contact force distribution and the contact type are very important, the problem would be oversimplified when using the single point contact assumption. This is very important when studying the effect of the support geometry on the wear rates which will be discussed in the next section.

5. 4. 4 TUBE WEAR MODEL

The ultimate goal of the fretting wear analysis of heat exchanger tubes is to estimate tube wall thickness loss. This is accomplished by utilizing the normal work rate. The normal work rate, which is defined as the integral of the normal contact force and the sliding

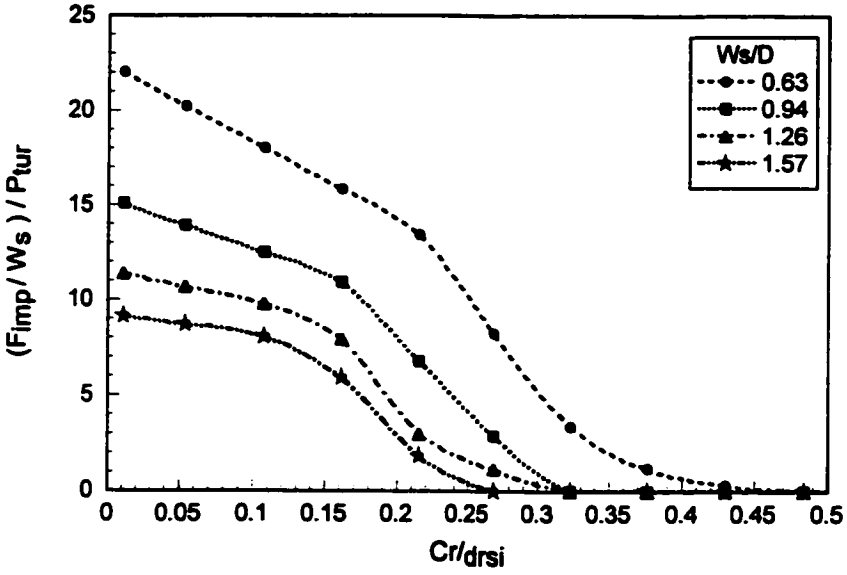

Figure 5.21 The dimension contact pressure for the cantilever tube case

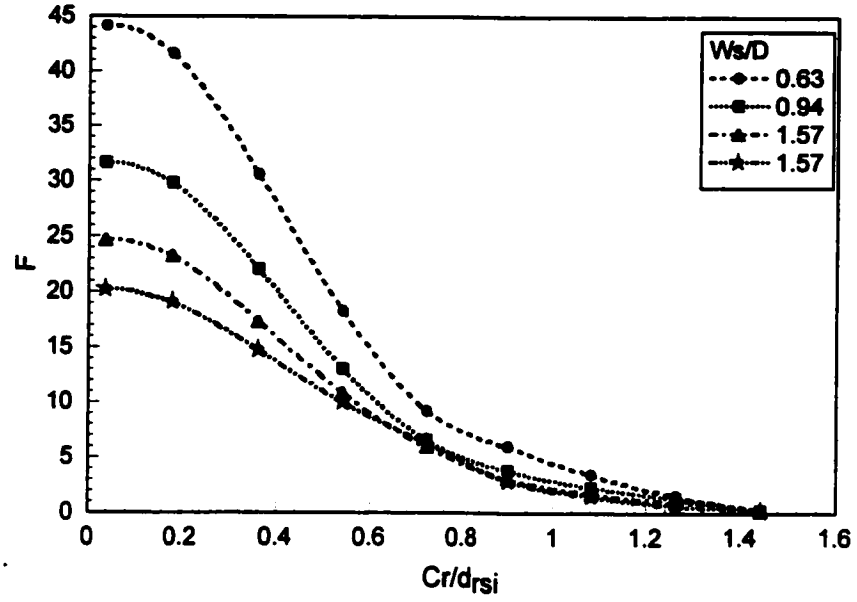

Figure 5.22 The dimensionless contact pressure for the two-span tube case

distance per unit time, is usually used to calculate the fretting wear volume rate $\dot{V}$:

$$\dot{V} = C_w \dot{W} \tag{5.56}$$

where C_w is the wear coefficient obtained experimentally. The literature suggests that the wear coefficient for continuous sliding is larger than the wear coefficient for fretting (Connors, 1981). Using this equation, the volumetric loss can be calculated. The cumulative tube wall loss can be expressed as follows:

$$h(t) = \int_{t_o}^{t} \dot{h}(t)dt \tag{5.57}$$

where $\dot{h}(t)$ is the rate of the wall thickness loss which is a function of the volume wear rate.

The cumulative depth of wear must be calculated incrementally. This is because as the tube thickness decreases due to wear, the tube-to-support clearance increases. This in turn, changes the nonlinear dynamics of the tube. As a result, the normal work rate changes with time as the tube wall wears out. The relationship between the normal work and the support clearance can be obtained using the nonlinear simulation carried out in Section 5.4.2. The incremental procedure starts with considering an initial tube-to-support clearance $Cr(t_o)$ at time t_o. After a time increment of Δt, a volume ΔV is removed from the tube. This volume can be calculated using Equation (5.56). The tube wear depth associated with this wear volume can be determined by defining the geometry of the wear scar. The geometrical relationship between the wear volume and the wear depth of a tube contacting a flat-bar support is shown in Figure 5.23. Assuming that the tube and the flat bar are perfectly aligned, the volume of the removed material, ΔV, is given by:

$$\Delta V = \frac{R^2 W_s}{2}(2\alpha - \sin(2\alpha)) \tag{5.58}$$

where R and α are the tube radius and the contact angle respectively. The contact angle is related to the scar width S by the following relationship:

$$\alpha = \sin^{-1}\left(\frac{S}{2R}\right) \tag{5.59}$$

The wear depth Δh can be obtained as follows:

$$\Delta h = R(1 - \cos\alpha) \tag{5.60}$$

The scar width S is not known and hence Δh is obtained using an iterative procedure using the following equation:

$$\Delta V = \frac{\Delta h W_s}{12\sqrt{2R\Delta h - \Delta h^2}}\left(3\Delta h^3 + 2R\Delta h - \Delta h^2\right) \tag{5.61}$$

The above relations are used to determine the wear depth for the first time increment only since the subsequent tube surface is no longer circular. The subsequent time increments assume flat tube wear area. The new wear volume is shown in Figure 24. The calculation of the updated wear depth is carried out by assuming the cross section of the wear layer is a rectangle of width S. This is a reasonable assumption if the time increment is small enough. Now, the current tube-to-support clearance must be updated to reflect the loss of tube thickness at the support location as follows:

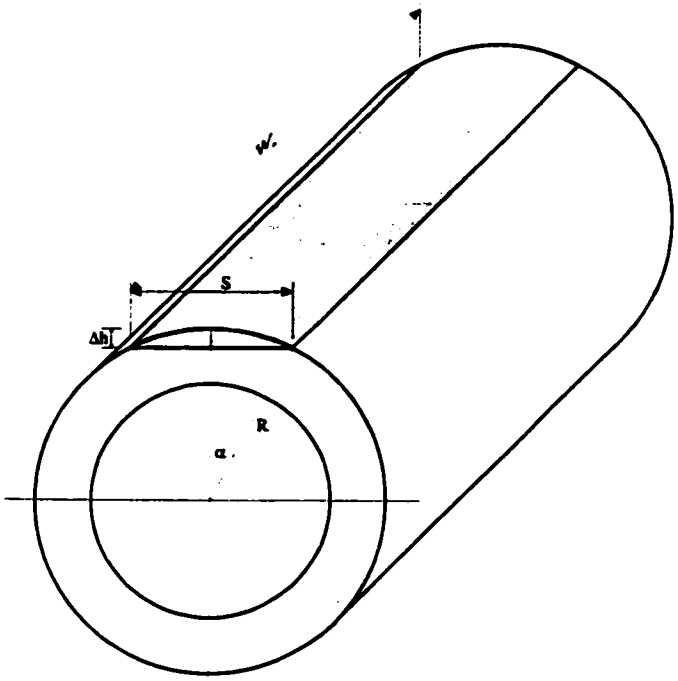

Figure 5.23 Geometry of the initial wear volume of a tube with a flat-bar support

$$Cr(t) = Cr(t_o) + h(t) \tag{5.62}$$

This new value of the support clearance will result in a change in the current normal work rate which can be obtained from Figure 5.20. These calculations continue until the wall thickness reaches a target value. For the calculations presented in this Section, C_w will be assumed equal to 40×10^{-15} Pa^{-1}. The same wear coefficient will be used for continuous sliding and for intermittent impact. The purpose of these calculations is to provide a comparison on the effect of the width on the tube's dynamics rather than an exact estimate of the heat exchanger life. Therefore, the simplified example provided herein represents a portion of the overall evaluation that is required. Figure 5.25 depicts the calculated dimensionless depth of wear ($h(t)/d_{ri}$) for different support width values. These curves were produced for the two-span tube configurations discussed in Section 5.4.2. The initial dimensionless clearance is 0.036 and a time increment of 10^5 seconds was used. The time is incremented until the dimensionless clearance reaches a value of 0.36. Results show that the rate of the tube wear depth decreases with time as wear volume is distributed over a larger area of the tube surface (Guérout and Fisher, 1999). Increasing the support width results in a lower depth of wear. These wear predictions agree with the findings of Langford and Connors (1991).

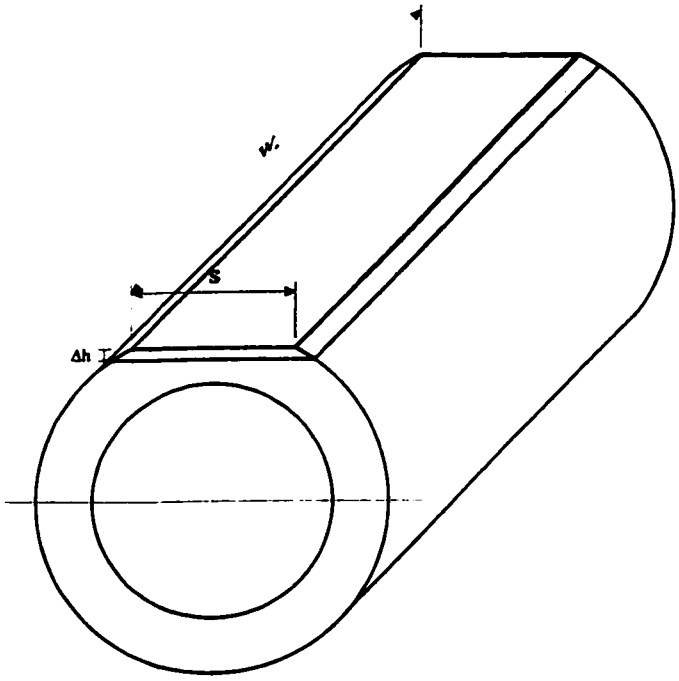

Figure 5.24 Geometry of the wear volume of a tube with a flat-bar support

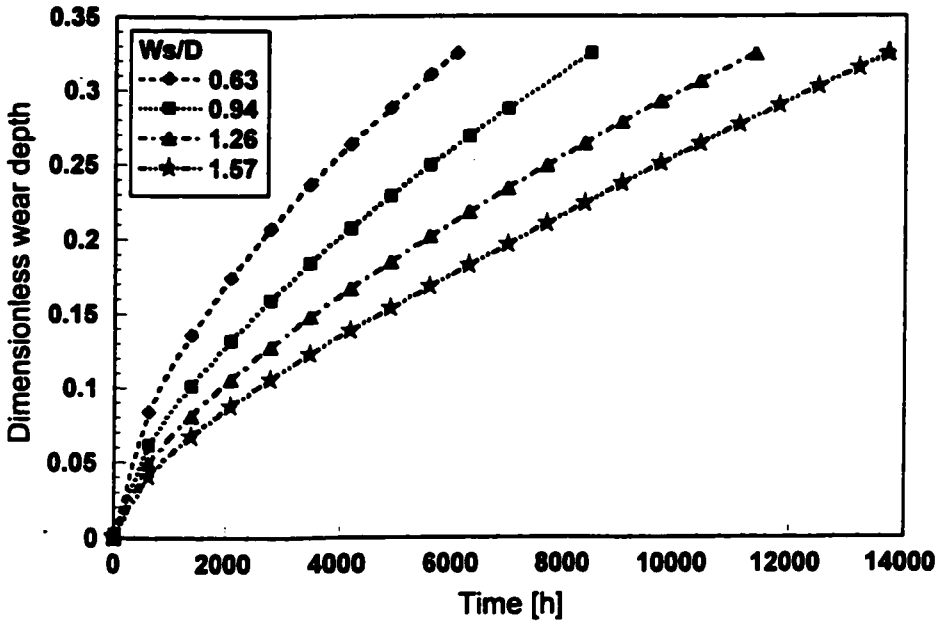

Figure 5.25 The predicted dimensionless wear depth versus time

5.5 SUMMARY

A tube-support interaction model was developed to simulate a more realistic support configuration. In this model, the support width was taken into account when calculating the contact forces and the work rate. The tube/support contact was modelled by a distributed stiffness. The impact forces were distributed along the contact segment using the beam displacement interpolation function. The equivalent nodal force vector was derived in a manner consistent with the finite element formulation. The model was also capable of expressing an inter-nodal point contact which may be encountered.

Numerical simulations were carried out using the new model to examine the effect of the support width on the tube dynamics. Using this model, it was possible to calculate the tube-support interaction parameters resulting from the point or the segment contact. The simulation results showed that increasing the support width yields a relatively higher total segmental contact force and normal work rate. However, since this contact force is distributed over a larger area when using a wider support, the resulting contact pressure is lower. In addition, the wear calculations showed that using wider supports results in a lower penetration rate.

CHAPTER 6

CONCLUSIONS AND RECOMMENDATIONS

6. 1 CONCLUSIONS

Tube failure is a major concern with regards to the operation of heat exchangers in nuclear power and chemical process plants. The need to plug failed tubes results in costly, unplanned shut downs. A major contributor to these failures is tube fretting wear, which is a consequence of excessive flow-induced vibrations. These vibrations result in impact and friction forces at the tube/support interface. Fluidelastic instability and turbulence have been identified as the main cause for these vibrations. The first mechanism usually results in short-term tube failure and must be avoided. Turbulence-induced forces, however, have a persistent effect and thus determine the long-term reliability of heat exchangers.

Tube/support interaction is a complex problem due to the strong nonlinear effects of

contact. The geometry of the support affects the dynamics of the tube due to variations in the contact configurations. Lattice-bar supports have a very complicated contact configuration due to the number of possible tube/support contact points. Understanding the tube dynamics related to this type of support is essential to the development of reliable heat exchangers and is the purpose of the research developed in this thesis.

To address these issues, a finite element tube/support impact model was developed and implemented in the general purpose finite element code INDAP. In this model, the nonlinear contributions of impact and friction are introduced to the system's equations of motion as a pseudo-force vector. The Newmark method was utilized to integrate the equations of motion projected on the modal coordinates. The equilibrium equations were solved iteratively to calculate the contact forces which opposes any overlaps. The model was then verified qualitatively and quantitatively through several examples.

An extensive parametric study was conducted which included simulations of tubes with lattice-bar supports. The model utilized a cantilever tube subjected to crossflow turbulence. The effect of the turbulence excitation including permanent tube/support preload arising from the crossflow drag and the tube-to-support clearances on the tube response were investigated. Tube behavior exhibited two distinct dynamic regimes (support-active and support-inactive modes) depending on the clearance and the excitation level. The results obtained showed that the tube exhibits two different responses in the drag and the lift directions. The lift response of the tube decreases slightly for a range of clearances, then increases, producing a point of minimum response at a certain clearance. This point of minimum response marks the transition in the tube's dynamics from the constrained to the

unconstrained configuration. This transition is also manifested by a change in the drag response. The drag response increases linearly, then levels off approaching the RMS tube response of the unconstrained configuration. The predicted work rate increases as the clearance increases up to a certain clearance value then decreases. Moreover, increasing the support clearance decreases the impact forces and the contact ratio.

Simulations of a multi-span tube indicate that, depending on the clearance, the effectiveness of some of the supports is changed. It was observed that a process of load-carrying redistribution takes place among the supports. Complex response spectra were observed in which multiple mode switches exist as the clearances are increased.

Square-flat-bar (SFB) supports and rhomboid-flat-bar (RFB) supports were utilized to study the effect of the lattice-support type on the tube dynamics. A better performance was demonstrated in terms of the wear work rate by the RFB support.

The effect of offseting the lattice-bar supports was also investigated. The results show that offset affects the tube dynamics substantially. In particular, the sliding contact and impact forces are increased such that the normal work rate is increased. Thus, in spite of increasing the complexity of the tube response through strong nonlinear coupling at the supports, substantial lattice-bar offset may generate increased wear at the supports.

The effect of flow orientation was investigated through several simulations utilizing the same tube model. The simulations have shown that SFB and RFB supports represent two special cases of flow orientation. They also represent an upper and a lower bound for the performance of the lattice-bar support. The study indicates that some flow orientations provide a favourable support geometry for higher normal work rates, and therefore, are more

susceptible to fretting wear damage.

In addition, the model was further modified to account for the effect of the support width. In this model, the contact configuration was generalized such that tube/support segment contact was permitted in addition to a general inter-nodal point contact. The impact problem was solved for the nodal forces that oppose the overlaps and satisfy a friction law. These contact forces were distributed over the contact segment using the shape functions of the displacement field. This treatment is consistent with the finite element method in dealing with the equivalent nodal forces.

The new model was utilized to study the effect of support width on tube fretting wear. Using the new model, it was possible to calculate the tube/support interaction parameters resulting from point or segment contact. It was found that increasing the support width yields a relatively higher total segmental contact force and normal work rate. On the other hand, the contact force is distributed over a larger area when using a wider support, resulting in a lower contact pressure. Wear calculations show that using wider supports results in a lower penetration rate.

For the first time, the tubes' response and the associated tube/support interaction parameters have been presented in dimensionless form. Dimensionless parameters effectively collapse the data obtained for the nonlinear response of loosely-supported heat exchanger tubes subjected to random turbulence excitation. The applicability of the methodology was confirmed by means of numerical simulations of different tube configurations. The introduction of these dimensionless parameters expands the power and the utility of the numerical model to predict a wider range of configurations and flow

conditions. This is significant since the procedure can be applied for design purposes in order to reduce the risk of fretting wear related failure by controlling the most dominant factor, the dimensionless clearance.

These results provide some new insights into, and a better understanding of, the underlying phenomena of nonlinear tube behaviour. There is however, still a great deal of work to be done on this topic.

6. 2 RECOMMENDATIONS FOR FUTURE WORK

Turbulence buffeting causes low amplitude tube motion resulting in long-term fretting wear or fatigue. However, progressive long-term wear and chemical cleaning processes cause enlargement of the support clearances, which in turn alters the support effectiveness. As demonstrated throughout this work, this leads to the evolution of low frequency tube modes. These modes may become unstable at low flow velocities due to fluidelastic coupling forces. The fluidelastic instability response amplitude of the tubes increases steadily until tube/support impact becomes unavoidable. These extremely nonlinear vibratory motions have a high-risk potential, since tube velocities and impact forces can lead to unacceptable rates of fretting wear. Therefore, any proposed research must include developing an accurate, analytical model that accounts for both structural (tube/support interaction) and fluid (motion-dependent fluid forces) nonlinearities.

The recommended research aims at studying the tube vibratory response in the post-stability regime. This includes modelling the fluidelastic forces through effective velocity and effective stiffness coefficient feedback. This enables the tube to gain energy

through the negative damping ratio of the unstable modes. Post stability amplitude evolution can then be predicted. It is also imperative to verify the proposed model with an experimental investigation of U-bend tube and straight tube models subjected to partial admission cross-flow.

In addition, the effect of the superposition of turbulent buffeting and fluidelastic excitation on the response of nuclear plant steam generator tubes would be of great importance. Special attention must be paid to the evolution of dynamic parameters influencing wear and to the changes in the dynamic regimes. Moreover, a study should be conducted to resolve issues related to the effect of the support type. As well, the influence of friction on the vibration and the instability of the tube under these severe conditions should be investigated.

In addition, it is equally important to generalize the results in order to correlate the tube nonlinear-response to the random excitation due to turbulence and fluidelastic instability. This includes the nondimensionalization of the tube response and its corresponding wear rate.

REFERENCES

Antunes, J., Axisa, F., and Vento, M., 1990, "Experiments on Vibro-Impact Dynamics Under Fluidelastic Instability," ASME PVP Conference., Tennessee, USA, 127-138.

Antunes, J., Axisa, F., Beafils, B., and Guilbaud, D., 1988, "Coulomb Friction Model in numerical Simulations of Vibration and Wear Work Rate of Multispan Tube Bundle," International Symposium on Flow Induced Vibrations and Noise, Chicago, pp. 157-176.

Axisa, F., Antunes, J., and Villard, B., 1990, "Random Excitation of Heat Exchanger Tubes by Cross Flows", Journal of Fluid and Structures, Vol. 4, pp. 321-341.

Axisa, F., Antunes, J., and Villard, B., 1988, "Overview of Numerical Methods for Predicting Flow-Induced Vibration," Journal of Pressure Vessel Technology, Vol. 110, pp 6-14.

Axisa, F., Desseaux, A., and Gibert, R., 1984, "Experimental Study of Tube/Support Impact Forces in Multi-Span PWR Steam Generator Tubes," Symposium on Flow-Induced Vibrations, Winter Annual Meeting, New Orleans, Vol.3, pp. 139-148.

Blevins, R., 1993, "Turbulence Induced Vibration," Technology for the 90s, Part III, Ch. 4, ASME, pp. 681-710.

Blevins, R., Gibert, R., and Villard, B., 1981, "Experiment on Vibration of Heat Exchanger Tube Arrays in Cross Flow," Trans. 6th International Conference on Structural Mechanics in Reactor Technology, Paris, Paper b6/9.

Blevins, R., 1975, "Vibration of a Loosely Held Tube," Journal of Engineering for Industry, Vol. 97, pp. 1301-1304.

Bohm, G., and Nahavandi, A., 1972, "Dynamics of Reactor Internal Structures with Impact Between components", Nuclear Science Engineering, Vol. 47, pp. 391-408.

Chen, S., Jendrzjczyk, J., and Wambsganss, M., 1985, "Dynamics of Tubes in Fluid with Tube-Baffle interaction," Journal of Pressure Vessel Technology, Vol. 107, pp 7-17.

Connors, H., and Kramer, F., 1991, "U-bend Shaker Test Investigation of Tube-AVB Wear Potential," Proceedings of the Fifth International Conference on Flow-Induced Vibrations, Brighton, U.K., C416/014, pp. 57-67.

Connors, H., 1981, "Flow-Induced Vibration and Wear of Steam Generator Tubes," Nuclear Technology, Vol. 55, pp. 311-331.

Den Hartog, J., 1931, "Forced Vibrations With Combined Coulomb and Viscus Friction," Transactions of the American Society of Mechanical Engineers, Vol., 53, pp. 107-115.

Dokainish, M., 1988a, "Incremental Nonlinear Dynamic Analysis Program: Theoretical Manual. INDAP Manual," McMaster University, Ontario, Canada.

Dokainish, M., 1988b, "Incremental Nonlinear Dynamic Analysis Program: User's Manual. INDAP Manual," McMaster University, Ontario, Canada.

Dokainish, M., 1988c, "Incremental Nonlinear Dynamic Analysis Program: Verification Manual: INDAP Manual," McMaster University, Ontario, Canada.

Eisinger, F., Rao, M., Steininger, D., and Haslinger, K., 1995, "Numerical Simulation of Cross-Flow-Induced Fluidelastic Vibration of Tube Arrays and Comparison With Experimental Results," Journal of Pressure Vessel Technology, Vol. 111, pp. 378-384.

Elliot, G., 1973, "Dynamic Response of Heat Exchanger Tubes," Master of Engineering Thesis, University of Waterloo, Ontario, Canada.

Fisher, N., Pettigrew, M. and Rogers, R., 1991, "Fretting wear damage prediction in the inlet region of nuclear steam generators," Proceedings of the 5th International Conference on Flow Induced Vibrations, Brighton, U.K. 129-137.

Fisher, N., Olesen, M., Rogers, R., and Ko, P., 1989, "Simulation of Tube-to-Support Dynamic Interaction in Heat exchange Equipment," Journal of Pressure Vessel Technology, Vol. 111, pp 378-384.

Fisher, N. and Ingham, B., 1989, "Measurement of Tube-to-Support Dynamic Forces in Fretting-Wear Rigs," Journal of Pressure Vessel Technology, Vol. 111, pp. 385-393.

Fricker, A., 1992, "Numerical Analysis of the Fluid-Elastic Vibration of a Steam Generator Tube with Loose Support," Journal of Fluids and Structures, Vol. 6, pp. 85-107.

Fricker, A., 1991, "Vibro-impacting Behaviour of Fluid-elastically unstable Heat Exchanger Tubes with support clearances," Proceedings of the Fifth International Conference on Flow-Induced Vibrations, Brighton, U.K., C416/021.

Guérout F., and Fisher, N., 1999, "Steam generator fretting-wear damage: a summary of recent findings," Journal of Pressure Vessel Technology, Vol. 121, pp. 304-210.

Goyder, H.,1982, "Measurements of the natural Frequencies and Damping of Loosely Supported Tubes in Heat Exchangers," Vibration in Nuclear Plants, 3rd Keswick Conference, England.

Hundal, M., 1979, "Response of a Base Excited System With Coulomb and Viscous Friction," Journal of Sound and Vibration, Vol. 64(3), pp. 371-378.

Haslinger, K. and Steininger, D., 1995, "Experimental Characterization of Sliding and Impact Friction Coefficients Between Steam Generator Tubes and AVB Supports," Journal of Sound and Vibration, Vol. 181(5), pp. 851-871.

Haslinger, K., Martin, M., and Steininger, D., 1987, "Pressurized Water Reactor Steam Generator Tube Wear Prediction Utilizing Experimental Techniques," International. Conference on Flow-Induced Vibrations, England. K2:437-448.

Haslinger, K. and Steininger, D., 1984, "Steam Generator Tube/Tube Support Plate Interaction Characteristics", Symposium on Flow-Induced Vibrations, Winter Annual Meeting, New Orleans, Vol.3, pp. 9-14.

Hunt, K., and Crossley, F., 1975, "Coefficient of Restitution Interpreted as Damping in Vibroimpact," Journal of Applied Mechanics, June, pp. 440-445.

Iwase, T., Sunami, T., Matsutani, K., Nakamura, T., Mureithi, N., Tsuge, A., Watanabe, Y., Tomomatsu, K., and Takaba, O., 1997, "Flow-induced Vibration of a Tube Array in the Inlet Region of a High Performance Steam Generator (Part 1 : Turbulence Induced Vibration," ASME Winter Annual Meeting, Dallas, Texas, Vol. 1, pp. 265-272.

Johansson, L., 1997, " Beam Motion With Unilateral Contact Constraints and Wear Contact Sites," Journal of Pressure Vessel Technology, Vol. 119., pp. 105-110.

Langford, P. and Connors, H., 1991, "Calculation of tube-AVB wear from U-bend Shaker test Data," Proceedings of the 5th International Conference on Flow Induced Vibrations, Brighton, U.K., pp. 45-55.

Levitan, E., 1960, "Forced Oscillation of a Spring-Mass System having Combined Coulomb and Viscus Friction," Journal of Acoustical Society of America, Vol. 32, pp. 1265-1269.

Molnar, A., Vashi, K., and Gay, C., 1976, "Application of Normal Mode Theory and Pseuoforce Method to solve Problems with Nonlinearities," Journal of Pressure Vessel Technology, May, pp. 151-156.

Nakamura, T. and Fujita, K., 1987, "A Study on Impact Vibration of Loosely Held Tube by Cross flow," International Conference on Flow-Induced Vibrations, England. K1:427-426.

Oengören A., and Ziada, S., 1995, "Vortex Shedding, Acoustic Resonance and Turbulent Buffeting in Normal Triangle Tube Arrays," Flow Induced Vibrations, Bearman (ed.), Balkema, Rotterdam.

Pettigrew, M., Carlucci, L., Taylor, C., and Fisher, N., 1991, "Flow-Induced Vibration and Related Technologies in Nuclear Components," Nuclear Engineering and Design, Vol. 131, pp. 81-100.

Pettigrew, M., and Gorman, D., 1978, "Vibration of Heat Exchanger Components in Liquid and Two-Phase Cross-Flow," Proceedings BNES International Conference on Vibration in Nuclear Plant, Keswick, UK, Paper 2.3.

Phillips, M. and Taylor, P., 1973, "Theory and Applications of Numerical Analysis," Academic Press, London.

Rogers, R., and Pick, R., 1977, "Factors Associated with Support Plate Forces due to Heat Exchanger Tube Vibratory Contact," Nuclear Engineering and Design, Vol. 44, No. 2, pp 247-253.

Rogers, R. and Pick, R., 1976, "On the Dynamic Spatial Response of a Heat Exchanger Tube with Intermittent Baffle Contacts," Nuclear Engineering and Design, Vol. 36, pp. 81-90.

Shah, V., Bohm, G., and Nahavandi, A., 1979, "Modal Superposition Method for Computationally Economical Nonlinear Structural Analysis," Journal of Pressure Vessel Technology, Vol. 101, pp. 134-141.

Sauvé, R., 1996, "A Computational Time Domain Approach to Fluidelastic Instability for Nonlinear Tube Dynamics," Symposium on Flow Induced Vibrations, ASME PVP/ICPVT-8 Conference, Montreal, Canada, Vol. 328, pp. 111-121.

Sauvé, R., 1994, "Turbulent Forcing Function Models for Process Equipment Tube Vibration," Ontario Hydro Technologies, Report No. A-NSG-94-125-P.

Sauvé, R. , and Teper, W., 1987, "Impact Simulation of Process Equipment Tubes and Support Plates-A Numerical Algorithm," Journal of Pressure Vessel Technology, Vol. 109,

pp 70-79.

Shinozuka, M., 1974, "Digital Simulation of Random Process in Engineering Mechanics with the Aid of FFT Technique," Stochastic Problems in Mechanics, University of Waterloo Press, pp. 277-286.

Salmon, M., Verma, V., and Youtsos, T., 1985, "Elastic Analysis of Beam-Support Impact," Journal of Pressure Vessel Technology, Vol. 107, pp. 64-67.

Tan, X. and Rogers, R., 1996, "Dynamic Friction modelling in Heat exchanger tube Simulations", ASME PVP/ICPVT-8 Conference, Montreal, Canada, Vol. 328, pp. 347-358.

Taylor, C., Boucher, K., and Yetisir, M., 1995, "Vibration and Impact Forces Due to Two-Phase Cross-Flow in U-bend Region of Nuclear Steam Generators," Flow Induced Vibrations, Bearman, P. (ed), Balkema, A., Rotterdam, pp. 401-412.

Taylor C., Pettigrew, M., Axisa, F., and Villard, B., 1988, "Experimental Determination of Single and Two-Phase Cross Flow-Induced Forces on Tube Rows," Journal of Pressure Vessel Technology, Vol. 110, pp. 22-28.

Ting, E., Chen, S., and Wambsganss, M.,1979, "Dynamics of Component-Support Impact: An Elastic Analysis," Nuclear Engineering and Design, Vol. 52, pp. 235-244.

Thomson, W. and Dahleh, M., 1998, "Theory of Vibration with applications," 5th edition, Printice-Hall Inc.

Watanabe, T., 1981, "Steady Impact Vibration of Continuous Elements," Bulletin of the JSME, Vol. 24, pp. 222-228.

Weaver, D. and Fitzpatrick, J., 1988, "A review of cross-flow induced vibrations in heat exchanger tube arrays," Journal of Fluids and structures, Vol. 2, pp. 73-93.

Weaver, D., and Schneider, W., 1983, "The effect of flat bar supports on the crossflow induced response of heat exchanger U-tubes," Journal of Pressure Vessel Technology, Vol.105, pp.775-781.

Yetisir, M., McKerrow, E., and Pettigrew, M., 1997, "Fretting wear damage of heat exchanger tubes: a proposed damage criterion based on tube vibration response," ASME Winter Annual Meeting, Flow Induced Vibrations and Noise, Dallas, Vol. 2, pp. 291-299.

Yetisir, M., and Fisher, N., 1996, "Fretting Wear Prediction in Heat Exchanger Tubes: Effect of Chemical Cleaning" Symposium on Flow Induced Vibrations, ASME PVP/ICPVT-8

Conference, Montreal, Canada, Vol. 328, pp. 285-296.

Yetisir, M., 1987, "The Vibro-Impact of Heat Exchanger U-Bend Tubes With Flat Bar Supports," Master Thesis, McMaster University, Ontario, Canada.

Yetisir, M., and Weaver, D., 1986, "The Dynamics of Heat Exchanger U-bend Tubes With Flat-Bar Supports," Journal of Pressure Vessel Technology, Vol. 108, pp. 406-412.